Particle Image Velocimetry and Analysis Methods using Cleanly Seeded Particles in Supersonic Flow

THESIS

Paul A. Gulotta, Second Lieutenant, USAF

AFIT-ENY-MS-16-J-053

DEPARTMENT OF THE AIR FORCE
AIR UNIVERSITY

AIR FORCE INSTITUTE OF TECHNOLOGY

Wright-Patterson Air Force Base, Ohio

AFIT-ENY-MS-16-J-053

PARTICLE IMAGE VELOCIMETRY AND ANALYSIS METHODS USING

CLEAN SEEDING IN SUPERSONIC FLOW

THESIS

Presented to the Faculty

Department of Aeronautical Engineering

Graduate School of Engineering and Management

Air Force Institute of Technology

Air University

Air Education and Training Command

in Partial Fulfillment of the Requirements for the

Degree of Master of Science in Aeronautical Engineering

Paul A. Gulotta, B.S.A.E.

Second Lieutenant, USAF

May 25, 2016

AFIT-ENY-MS-16-J-053

PARTICLE IMAGE VELOCIMETRY AND ANALYSIS METHODS USING

CLEAN SEEDING IN SUPERSONIC FLOW

THESIS

Paul A. Gulotta, B.S.A.E.
Second Lieutenant, USAF

Committee Membership:

Dr. M. Reeder, PhD
Chair

Dr. M. Polanka, PhD
Member

Lt. Col. A. DeLuca, PhD
Member

AFIT-ENY-MS-16-J-053

Abstract

Particle Image Velocimetry (PIV) was successfully conducted in the Air Force Research Lab Mach 3/ Mach 6 Facility (M3M6F) for the first time. Particle response experiments evaluating the performance of dry ice particles across an oblique shock wave were conducted using a 15 degree half-wedge in nominal Mach 3 flow. Solid carbon dioxide particles are generated through rapid expansion of liquid carbon dioxide via a small nozzle within a simple shroud tube or a tube containing static mixing elements. Particles are injected directly into the settling chamber of the Mach 3 tunnel. The particle response of carbon dioxide particles is compared to that of water particles produced from ambient moisture content in the tunnel system. Carbon dioxide particles produced particle response curves indicating particle diameters of approximately 2 microns acclimating to the asymptotic change in velocity across the shock between 25 and 30 mm on a path normal to the shock wave. Ambient water particles had a somewhat faster response acclimating within 20 to 25 mm. Analysis methods in Dantec DynamicStudio 2015a, such as cross correlation in 32x32 pixel and 64x64 pixel Interrogation Regions (IR), were compared to other techniques, namely the Adaptive PIV method and the Least Squares Method. The effects of analysis method on both freestream velocity and particle response were investigated. Other augmentations such as peak validation, Gaussian window functions, and image pre-processing techniques were evaluated using the same performance metrics.

Acknowledgements

Table of Contents

. List of Acronyms

AFIT Air Force Institute of Technology

AIAA American institute of Aeronautics and Astronautics

AFRL-RQ Air Force Research Labs Aerospace Systems Directorate

BBO Basset Boussinesq Oseen

CCD Charged-coupled Device

CMOS Complementary metal-oxide semiconductor

FFT Fast Fourier Transform

IFFT Inverse Fast Fourier Transform

IR Interrogation Region

LED Light Emitting Diode

M3M6F Mach 3/Mach 6 Facility

NASA National Aeronautics and Space Administration

PIV Particle Image Velocimetry

PSV Particle Shadow Velocimetry

TGF Trisonic Gas Dynamics Facility

WPAFB Wright-Patterson Air Force Base

. **List of Symbols**

d_p Particle diameter

ρ_p Particle density

ρ_f Fluid density

μ Dynamic viscosity of the fluid

Re_p Reynolds number of the particle

V Instantaneous relative velocity

U_p Instantaneous relative velocity of the particle

V_p Instantaneous relative velocity of the fluid

s Density Ration

Δt A small change in time

C Characteristic frequency of the particle

C_D Coefficient of drag

τ_p Characteristic response time of the particle

τ_k Kolmogorov time scale

L Length

U_o Freestream Velocity

x_M Mie Parameter

λ Wavelength of Light

$R(s)$ Spatial cross correlation

D_{32} Sauter mean diameter

n_i Total number of particles

D_i Particle diameters

u_n Particle velocity normal to the shock

t Time

x_n Particle position normal to the shock

ξ_p Particle Relaxation Length

M Mach number

$M_{n,1}$ Mach number upstream and normal to the shock

$M_{n,2}$ Mach number downstream and normal to the shock

a Speed of Sound

γ Ratio of Specific Heats

T Tempurature

T_0 Stagnation Temperature

T_{0VM} Velocity Match Stagnation Temperature

β Wave angle

β_c Compensated Wave Angle

β_{image} Deflection angle according to linear regression

θ Deflection Angle

θ_c Compensated Deflection Angle

θ_{offset} Deflection angle offset

θ_{image} Deflection angle according to linear regression

A_1^* Area Required for Sonic Flow

q Heat released during condensation per unit mass

Q Ration of heat release per unit mass via condensation

Q_{max} Max Q at a given Mach number

L Latent Heat of vaporization

m_v mass of water vapor

m_a mass of water vapor

p_v partial pressure of water vapor

p_∞ partial pressure of water vapor

p_0 Stagnation pressure

U Horizontal Velocity Component

V Vertical Velocity Component

V_{norm} Velocity normal to the shock

α Flow angle

$\alpha_{average}$ Average Flow angle

$V_{average}$ Averaged Freestream Velocity

V_{theory} Velocity from theory

List of Figures

List of Tables

PARTICLE IMAGE VELOCIMETRY AND ANALYSIS METHODS USING
CLEAN SEEDING IN SUPERSONIC FLOW

I. Introduction

Since the Wright Brothers took flight in 1903, aerodynamicists have been challenged with the fundamental issue of visualizing the invisible movements of fluids, such as air. Though much information can be gleaned from pure aerodynamic theory, it is often difficult to understand certain phenomena unless they are observed visually. Thus, the art and science of flow visualization was born. Fluids have been visualized in many different ways. Some examples include smoke injection into gas, the injection of dye into moving liquids, and even surface visualization using oil films [15]. While these visualization techniques provided amazing visual representations of effects previously disguised by fluid transparency, they are limited by the fact that they do not reveal any additional information about the numeric magnitude of the velocity fields.

Figure 1. Dye visualization in water tunnel (Left), oil film visualization (Middle) on wind tunnel wall, smoke visualization (Right) over an airfoil [15]

The most traditional means of observing velocity magnitudes in a flow field are through sensors such as pitot tubes or hot wire anemometers. These sensors enable the aerodynamicist to collect data on fluctuating pressure and velocity magnitudes.

1

While these sensors are extremely useful, they are hampered by two fundamental flaws. The first flaw is the fact that they are physically inserted into the region of interest and disturb the natural direction of the flow. Thus, by measuring a flow's characteristics, the aerodynamicist slightly alters its behavior. The second flaw of traditional measurement techniques is that they only measure a single point in space. In order to measure an entire flow field, multiple sensors must be arrayed to capture the necessary information, or a single sensor must be moved systematically to capture the data.

Over the past three decades, researchers have developed a technique which utilizes the concept of visualizing an entire flow field, while simultaneously measuring the velocity. This technique is called Particle Image Velocimetry (PIV). Figure 2. shows an example of PIV over an airfoil.
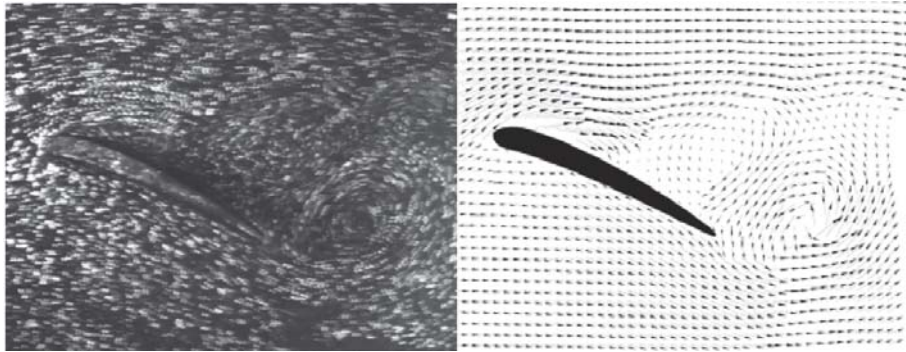
Figure 2. PIV over an airfoil. Particle image used for PIV (Left), velocity field (Right)[17]

1.1 Background

The desire to measure the instantaneous states of fluid motion as a holistic structure has lead aerodynamicists to develop and refine PIV techniques [21]. The principle behind PIV is not so different from classical flow visualization using smoke. Small particles are introduced into fluids such as air or water. These particles are carried by

the flow to a region of interest and are illuminated. Often this is accomplished using a thin pulsed laser sheet in precise temporal alignment with one or more high speed cameras. These high-resolution cameras capture two images, known as an image pair, which may have a very small time increment between them. These image pairs are divided into many smaller interrogation regions (IR), within which the movement of individual particles is examined and quantified via cross-correlation. From the analysis of the image pair, vectors can be drawn which describe the movement of particle fields during the time elapsed. Hence, the displacement, direction, and time elapsed between image capture is known, and, therefore, the particle velocity can be determined [21]. This principle is extended to the entire flow field and provides both a qualitative and quantitative representation of the flow. Particle imaging measurements have been captured in a variety of ways with two dimensional (classical), quasi two dimensional (stereoscopic), and even three dimensional (tomographical) techniques [6]. Research conducted in this thesis will focus on the application of a simplistic form, classical two dimensional PIV.

Since its conception, PIV has provided researchers in the fluid mechanics discipline with the opportunity to study a wide variety of flow regimes under drastically different situations. An early pioneer of PIV, Dr, R. J. Adrian, originally utilized this technique to examine the turbulent boundary layer phenomenon known as hairpin vorticies [1]. However, PIV techniques have also been extended to see flow patterns on the insides of internal combustion engines [19], to study the exhausts of rocket engines [4], and even to record measurements through a micro-channel only 30 nanometers wide [13]. The limits of this technique often lay in the creativity of the experimentalist and scope of the problem.

However, in order to implement PIV, the flow must be optically accessible to both a laser sheet and a camera system. There must also be particles present to observe the phenomena of interest. Lastly, the particle motion must be fully representative of the fluid motion in order to precisely detect velocity fields.

1.2 Research Problem Motivation

As the list of PIV applications continues to grow, so do the requirements for adaptive PIV systems and techniques. A subtle but critical component of the PIV process is the tracer or seed particles themselves. The definition of a quality seed particle varies with the application, but must meet several criteria in order to be effective. Seed or tracer particles must be "small enough" to be carried by a fluid in such a way that it responds sensitively to changes in velocity experienced by that fluid. The particles must also be "reflective enough" and in great enough numbers to be seen distinctly by the cameras within defined interrogation regions. Since reflection increases with particle size, there are two competing traits, and compromise on particle size is common. The direction that the light is scattered also directly impacts the ideal positioning of the cameras [21]. To give perspective on the importance of particle

4

choice, Dr R. J. Adrian, a pioneer of PIV, confessed at AIAA Aviation in 2015 that he "would rather give money to a researcher who would make better particles rather than someone making a more powerful laser or better software" [2] .

Common particles that are used frequently in wind tunnel tests include atomized vegetable oil, glycol water solutions, and titanium dioxide particles [21]. While all of these materials have been found to produce good results in a wide variety of conditions, they share a fatal flaw, which often denies them applicability in many facilities. Their weakness lies not in the performance of the particles, but in the aftermath of the experiment. Many wind tunnels operate in closed-loop formats, which do not release the particles into the open atmosphere. Thus, after the test has concluded, these particles accumulate on virtually all surfaces within the tunnel. Eventually, these surfaces and exposed systems need to be cleaned for a variety of reasons, including the fact that some other diagnostics require a particle free environment. For large tunnels, this cleaning process can be very costly in both time and money—so costly in fact, that PIV is seldom used in those facilities as a result. One example of a facility that experienced this exact problem is the Icing Research Tunnel at NASA Glenn. Susan Gordan, a NASA engineer, described a setback her team experienced in the late stages of experimental planning. The team realized that the particles they intended to use in the tunnel would not be allowed due to the contamination they would incur [2]. Though it is rarely described in publication, these facilities represent a gap in PIV capability. For purposes of expanding the applicability of PIV as a flow visualization and measurement technique, it is important that an additional requirement be imposed on the particles; if possible they should evaporate, sublimate, or otherwise leave a minimal footprint on the facility in which they are operating.

The concept of using particles that do not degrade their operating facility has been described as Clean Seeding [12]. The Air Force Research Lab (AFRL) at Wright

Patterson Air Force Base (WPAFB) has a vested interest in developing a reliable Clean Seeding PIV technique. One tunnel in particular, the Trisonic Gas-Dynamics Facility (TGF), is a closed-loop wind tunnel, which is afflicted by the same particle limitations previously described. For several years now, under the direction of Dr. Mark Reeder and with the support of AFRL, Air Force Institute of Technology (AFIT) researchers have been developing the concept of using solid carbon dioxide particles (dry ice) as seed for PIV experiments. The main advantages of dry ice particles are that they sublimate — leaving virtually no residues on the tunnel. The production of these particles is extremely cost efficient. The disadvantages of this particle type lie in the difficulty involved in producing consistently-sized and sufficiently small particles. Another factor is the particle size does not remain constant as it travels, due to a rate of sublimation that changes with respect to the operating conditions.

In recent years, researchers at AFIT have studied particles generated by a shroud tube system, which converts liquid carbon dioxide to a two-phase dry ice and gaseous carbon dioxide mix. Research conducted by Captain Love in 2010, Major Wolfe in 2012, and Captain Liber in 2014 has investigated many variables, which affect the size of particles produced by the shroud system and the respective sublimation rates of those particles. Some factors that have been explored are ambient stagnation pressure, freestream velocity, shroud type and size, temperature regulation, and the use of particle sizing grids [11, 24, 12]. These techniques will be discussed in greater detail in Chapter two. Much of the work done by Captain Liber and Major Wolfe was focused on establishing a boundary layer profile in the TGF, the work enhanced the understanding of image filtering techniques which can improve the interpretation of less than ideal PIV data [11, 24]. The research conducted by Capt Love was completed in a supersonic setting using shock waves to determine particle response rates and sizing. This effort, while producing promising results, was hampered by the

6

use of a ramp initiating from a tunnel-wall. This factor allowed a shock-boundary layer interaction to conflate particle response with shock wave motion[12].

Though much was learned from previous researchers at AFIT, several questions still require additional clarity:

- What factors influence particle size and number density as they are generated?

- Which particle injection configuration produces the best and most consistent performance?

- What filtering techniques can be applied to make the best use of less than ideal particle images?

1.3 Research Objectives and Brief Description of Methodology

The accuracy and applicability of any PIV technique relies heavily on the quality of the tracer particles, their generation process, and injection techniques. Thus, if PIV is to be used in closed-loop wind tunnel systems such as the TGF, it is important that the process of generating dry ice particles and adequately seeding the region of interest is honed to the point of consistent application and predictable results. Thus the following research objectives and generalized methods have been set for this research endeavor:

- Demonstrate Clean seeding PIV in the AFRL Mach 3/ Mach 6 Facility

  - Install seed injection ports in various configurations in settling chamber

  - Use Dantec PIV system to capture and process PIV image pairs

  - Apply filtering and post processing techniques to analyze image pair and produce vector maps

- Directly Investigate Particle Performance of Carbon Dioxide Particles

- Use acquired vector maps to analyze the Particle Lag across the shock wave generated by a 15 degree wedge in the center of the tunnel test section

- Compare Dry Ice Particle Performance to Other Seed Particles

  - Collect similar particle lag data across a shock wave from other particle types for performance comparison

- Create a Large Particle Filter

  - Develop a novel image filter which can remove only the largest particles from the image data

  - Compare results between the filtered and non-filtered data

- Investigate PIV analysis methods using Dantec DynamicStudio 2015a

  - Compare results between traditional Cross Correlation, Adaptive PIV, and Least squares analysis methods

  - Characterize the effects of method augmentations such as Peak Validation and Gaussian window functions

  - Characterize the effects of filtering techniques utilizing the Dantec Image Processing library

This research is funded by AFRL-RQVX and incorporates equipment both from AFRL and AFIT facilities. The Mach 3/Mach 6 Facility (M3M6F) is the primary experimental location. Developing capabilities in that tunnel will advance understanding of clean seeding while expanding the capabilities of AFRL-RQVX as a whole.

II. Background

2.1 PIV Fundamentals

2.1.1 PIV Operating Principle

A modern PIV system includes several core components which work in harmony in order to capture an entire flow field of interest. In order to use PIV in a flow field, the region of interest must be seeded with small tracer particles. The plane of interest is interrogated by a laser sheet generated from a pulsed laser directed through a cylindrical lens. These particles scatter the light which is directed at them from the laser sheet. Ideally, this scattered light is captured in the form of two images collected in quick succession by an optical sensor. This image pair is then transferred to a computer for analysis. In order to analyze an image pair, it must be divided into sub-regions known as Interrogation Regions. Within this interrogation region, a technique called cross-correlation may be employed to determine the mostly likely path that particles traveled within the time difference, Δt, which represents the time that separates the two images in the image pair.
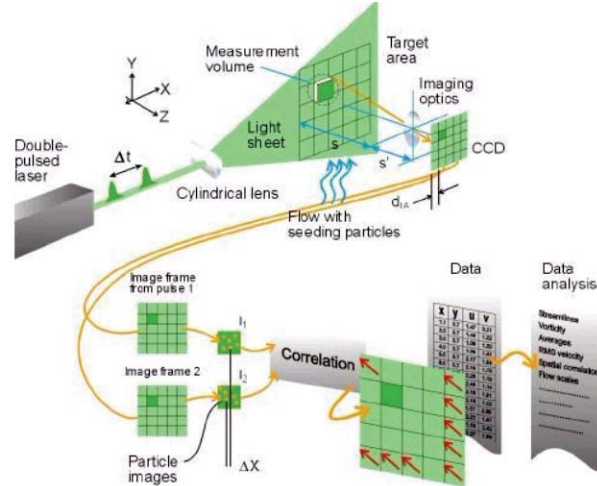
Figure 3. Diagram of PIV process [10]

9

2.1.2 Particle Illumination and Optical Equipment

A critical component in the PIV system is the light source which illuminates the particles for image capture. The ideal situation is one in which a light sheet uniformly illuminates an area with equal intensity and directionality. This ideal situation is never quite achieved, but it is most closely approximated through the use of a collimated light source and a specialized lens, which redirects the light into a thin light sheet. While this collimated light source cannot illuminate an entire area equally, the energy density should be high enough that the light scattered by the particles can be captured by the optical sensor anywhere within the region of interest.

Currently, the light source best suited for this task is a laser. However, there are additional qualities which narrow down the type of laser that is used for PIV applications. If a laser light is directed in a continuous manner, images captured by the optical sensors will capture particle streaks rather than discrete particle locations. While this may be useful for flow visualization, in order detect a velocity more accurately, a particle must be observed at two distinct points in time. Thus, the laser must be pulsed at a time interval Δt. While there are ways in which a pulsed laser effect can be achieved using a continuous wave laser, a pulsed laser is the light source of choice for most PIV applications [10].Pulsed lasers have the advantage over continuous wave lasers, because they are capable of producing extremely small pulse durations (typically around 9 nanoseconds). This small pulse duration reduces the aforementioned streaking effect seen in a continuous light source. A common type of pulsed laser is a double cavity Neodymium: Yttrium Aluminum Garnet Laser (Nd:YAG). The key words in the description of that laser are "double cavity". Not only must the laser system have very small pulse duration, it must also have a very short time between pulses in order to capture an image pair with a small Δt. A "double cavity" laser implies that there are essentially two identical lasers operating in a single unit. While

a single laser may be pulsed at a relatively high frequency, two lasers operating in tandem allows for a Δt which is significantly smaller and controllable through a very wide range [10]. This concept can be seen in Figure 4.

Typical Values
δt = few to several nanoseconds
Δt = micro-seconds to milliseconds
T = 0.03 to 0.1 seconds
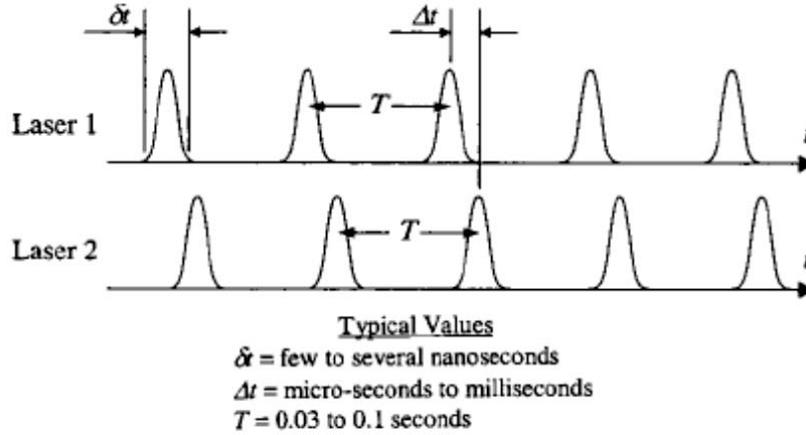
Figure 4.   Visual representation of dual cavity laser pulse times[10]

The laser unit itself produces a cylindrical beam of collimated light. This beam must be manipulated via a set of lenses which convert the cylindrical beam to a linearly-expanding sheet. A typical configuration uses two lenses in series, a plano-concave lens and a spherical lens. The plano-concave lens expands the beam linearly in one plane, while the spherical lens confines that plane to a thin laser sheet [16]. A visual representation of this can be seen in Figure 5.

Particles that cross the laser sheet scatter light, which is then captured by the optical sensor. In a modern PIV setting, the optical sensor will either be a charged coupled device (CCD) or a complementary metal oxide semiconductor (CMOS). Both of these camera technologies convert analog light signal to a digital format.

2.1.3   Flow Seeding Requirements

Proper illumination, while very necessary, does not necessarily guarantee high-quality PIV results. A critical component for good PIV data is the seed particles
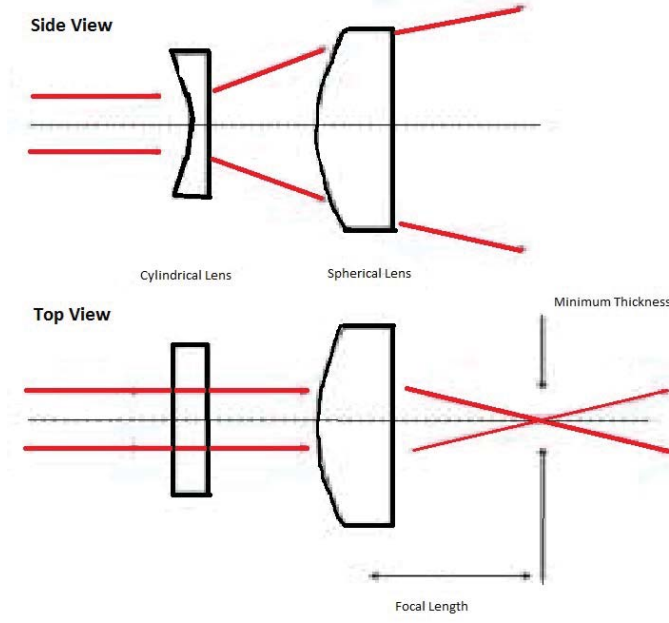
Figure 5. Visual representation of laser sheet optics [16]

themselves. The two primary characteristics are the ability of the particle to follow the flow and the ability of that particle to scatter the light that is directed at it. To identify whether or not a particle will acceptably follow the flow, several equations must be addressed. Melling [14] discusses the Basset Boussinesq Oseen equation (BBO), present here as equation (1), which represents the equation of motion for a small sphere moving in a low Reynolds number fluid. In the equation, $\hat{V}$, is the "instantaneous relative velocity" [14] where $\hat{V} = \hat{U}_p - \hat{U}_f$. Velocity, $\hat{U}_p$, is the instantaneous velocity of the particle and, $\hat{U}_f$, is the instantaneous velocity of the fluid.

$$\frac{\pi d_p^3}{6}\rho_p\frac{d\hat{U}_p}{dt} = -3\pi\mu d_p\hat{V} + \frac{\pi d_p^3}{6}\rho_f\frac{d\hat{U}_f}{dt} - \frac{1}{2}\frac{\pi d_p^3}{6}\rho_f\frac{d\hat{V}}{dt} - \frac{3}{2}d_p^2(\pi\mu\rho_f)^{\frac{1}{2}}\int_{t_0}^{t}\frac{d\hat{V}}{d\xi}\frac{d\xi}{(t-\xi)^{\frac{1}{2}}} \quad (1)$$

where:

d_p is the particle diameter

12

ρ_p is the particle density

ρ_f is the fluid density

μ is the dynamic viscosity of the fluid

The left-hand side of the equation is an acceleration force resulting from Stokes' Law. The terms on the right-hand side represent the following in order from right to left: viscous resistance of the particle to the flow, force on the particle due to a pressure gradient, fluid resistance to the acceleration of the sphere, and the "Basset history integral" defining the resistance to unsteadiness in the flow field. Some other parameters must be specified to understand the particle motion. One such parameter is the Reynolds number for a particle, which Melling [14] represents as:

$$Re_p = \frac{\rho_f \hat{V} d_p}{\mu} \tag{2}$$

A second important ratio is the density ratio of the particle to the fluid defined as:

$$s = \frac{\rho_p}{\rho_f} \tag{3}$$

If the density ratio is significantly greater than 1, Melling [14] simplified equation 1 to the following form:

$$\frac{d\hat{U}_p}{dt} = -C(\hat{U}_p - \hat{U}_f) \tag{4}$$

where C is the characteristic frequency which can be defined as:

$$C = \frac{3}{4} C_D Re_p \frac{\mu}{\rho_p d_p^2} \tag{5}$$

Melling [14] explains that coefficient of drag, C_D, in this situation can be approximated by the Stokes' approximation of drag

13

$$C_D = \frac{24}{Re_p} \tag{6}$$

Substituting C_D into Equation 5 the characteristic frequency C becomes

$$C = \frac{18\mu}{\rho_p d_p^2} \tag{7}$$

This leads to the characteristic response time of the particle τ

$$\tau_p = \frac{1}{C} = \frac{\rho_p d_p^2}{18\mu} \tag{8}$$

In PIV applications, a small characteristic response time is desirable. For a given fluid, τ_p increases linearly with density. Moreover, τ_p increases with the square of the particle diameter. Hence, a low density, small diameter particle is preferred. Now that the characteristic response time of the particle has been introduced, the principle of the non-dimensional Stokes number St_k can be discussed.

$$St_k = \frac{\tau_p}{\tau_k} = \frac{\tau_p U_o}{L} \tag{9}$$

The Stokes number represents a ratio, which compares the characteristic response time of the particle, τ_p, to the Kolmogorov time scale, which represents the time associated the passage of the smallest eddies in a turbulent fluid. The Kolmogorov time scale is $\tau_k = \frac{L}{U_0}$ where L is the length of the smallest eddies in a turbulent flow and U_0 is the freestream velocity of the fluid. It is a desirable seeding characteristic for the Stokes number to be less than 0.1, as this produces a particle tracing error of less than 1 percent [21]. Thus, given information about the particle diameter and density, as well as characteristics of the fluid of interest, the Stokes number provides a valuable metric for determining whether or not a particle will accurately follow the flow.

Adequate particle response is really only half of the restriction imposed on PIV particles. The other half of the requirements focuses on whether or not a particle can be viewed by the optical sensor. In the realm of PIV, particles diameters, d_p, are typically much smaller than wavelength of the laser light which hits them. This places them in Mie light scattering regime. If a particle is in the Mie regime, this implies two key traits about the particle. The first trait is that the particle scatters the greatest amplitude of light in the forward direction and less light at every other angle. The second trait is that the amplitude of the light scattered is governed by the Mie Parameter defined as [21]:

$$x_M = \frac{\pi d_p}{\lambda} \tag{10}$$

where d_p is the particle size and λ is the wavelength of the light that strikes the particle. As the Mie Parameter increases in value, so does the amplitude of the scattered light [21].
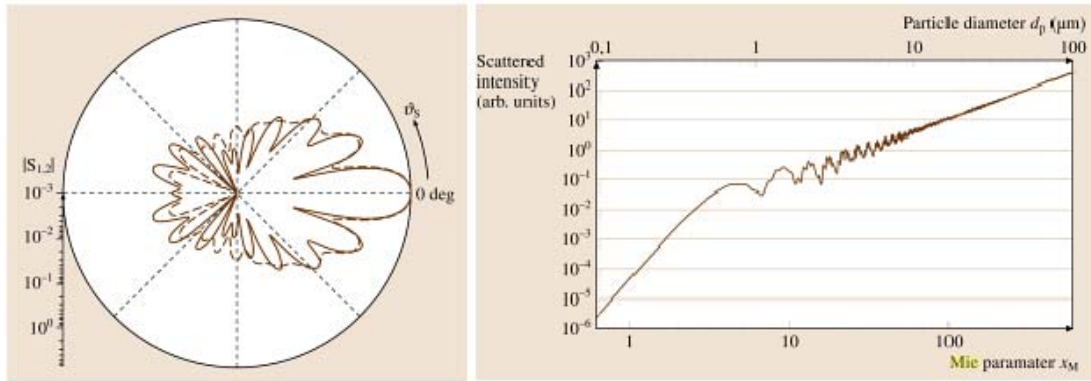
Figure 6. Diagram of scattered light intensity (Left) , graph comparing scattered light intensity and the mie parameter (Right)[21]

It may be noted that for PIV there is a conflict of interest between the amount of light a particle can scatter, and the particle response in a flow. As the particle diameter d_p increases, so does the Mie Parameter; however, the Stokes number also

increases. This means that while particles with bigger diameters will tend to scatter more light, bigger particle diameters inevitably lead to greater error in the particle response. Thus, a PIV experimentalist must find a balance between particle light scattering attributes and the particle's tendency to follow the flow. However, this analysis is based on the assumption that the diameter of the particle is known. In many instances, determining particle size or producing consistently sized particles can be very difficult. As a result, these areas are a primary focus for this research.

2.2 Image Capture and Processing Techniques

2.2.1 PIV Recording Modes and Classical PIV

The requirement for proper illumination and seeding remain relatively similar in most PIV applications. However, the image recording techniques and camera configurations can vary significantly depending on the situation.Broadly, all PIV image recording techniques fall into one of two camps: single frame multi-exposure image capture or multi-frame single exposure image capture.

In this context, the frame refers to a distinctly recorded image and an exposure refers to the illumination pulse. In single frame multi-exposure capture, the experimentalist would see two or more sets of the same particles, in the same image, at two or more periods in time. Understandably, this leads to some ambiguity in the temporal order of the particles relative to their spacial position. In multi-frame single exposure image capturing, the experimentalist sees only one set of particles per image and each image gets an independent laser pulse. With this method, there is no ambiguity of particle position with respect to time, because only one set of particles in included in each image [10]. The former method was originally used because camera image capture speeds where inadequate. However, with the advent of high speed CCD and CMOS cameras, the multi-frame single exposure image capturing method

is used more often in modern settings [11].

In classical PIV or two dimensional PIV, images are recorded on a single camera configuration seen in Figure 7. The camera is typically oriented perpendicular to the plane of interest in which the vertical and horizontal velocity components are captured. Calibration for this technique is relatively simple. An object of a precise length, typically a ruler or a dot board, is placed directly in line with the laser plane. A calibration image is taken and the object's length is measured within the software to determine the magnification and scale factor of the image.

Much has been learned, especially in the areas of turbulence and very small flows, from this simplistic configuration. However, the downside to using one camera is that it can only account for fluid motion in two dimensions and is subject to error, when particles move in and out of the image-capturing plane.
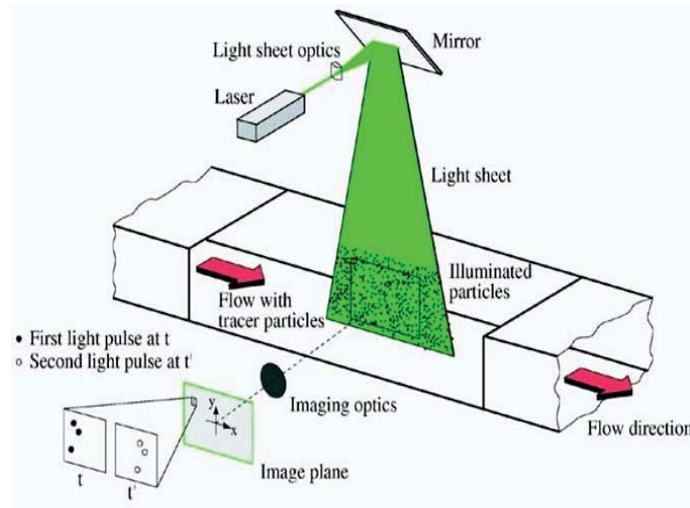
Figure 7. Schematic of classical PIV system [17]

On the other side of the PIV spectrum, three-dimensional multicamera techniques (usually 4 or more) exist such as holographic PIV or tomographic PIV, which are extremely difficult to achieve and often require resolutions exceeding the modern digital camera [1]. Stereoscopic PIV, using a two camera system, is often the method

of choice for the researcher who seeks some consideration for three-dimensional effects, but also seeks to avoid the extreme cost and complexity associated with full three dimensional techniques.

When deciding which technique to apply to a specific flow it is important to consider the type of flow the research is examining. As three dimensional effects become significant, using either stereoscopic or tomographic PIV techniques becomes more necessary. Complexity and cost are also driving factors when choosing a technique to apply. If the flow field is exhibits quasi two dimensional behavior , not much can be gained from a third velocity component given by stereoscopic or tomographic techniques. In this investigation, a single camera approach was sufficient and was thus utilized.

2.2.2   Cross Correlation

To understand the core of the PIV cross-correlation techniques, it is appropriate to start at the image sensor. On a basic level, the CCD or CMOS camera integrates the intensity of the scattered light over a very small area known commonly as a pixel. These pixels are discretized into a matrix of values which form an image [21]. Each image is subdivided into several smaller interrogation regions (IR), which are sometimes referred to as windows. These windows tend to be on the order of 32 x 32 pixels, 64 x 64 pixels, or 128 x 128 pixels — depending on the number density of the particles and their relative velocity. For good results, it is generally suggested that the windows be sized such that at least 10 particles are included [24]. By means of a fast Fourier transform (FFT), images are transported from the time domain to the frequency domain. In an image pair, light intensities of the pixels in corresponding windows are compared using a spatial cross correlation relation R(s) [21].

$$R(s) = \int W_1(\mathbf{x})I_1(\mathbf{x})W_2(\mathbf{x}+\mathbf{s})I_2(\mathbf{x}+\mathbf{s})dx \tag{11}$$

Where I_1 and I_2 represent the first and second images in an image pair, and W_1 and W_2 represent functions which describe the interrogation windows within the first and second images. Separation vector, $\mathbf{s}$, represents a displacement for every particle in the window. From the correlation, a peak represents the most likely displacement of particles within the window. If the velocities of all particles within the IR are very similar, a distinct peak will appear [24]. The correlation can then be converted back to the time domain by means of an inverse fast Fourier transform (IFFT). Since an average displacement was determined by the correlation procedure and the time Δt is known, a local vector can be determined for that IR. This process is repeated for all IR within the image, and a vector map is formed from the results. Figure 8 depicts the entire process.
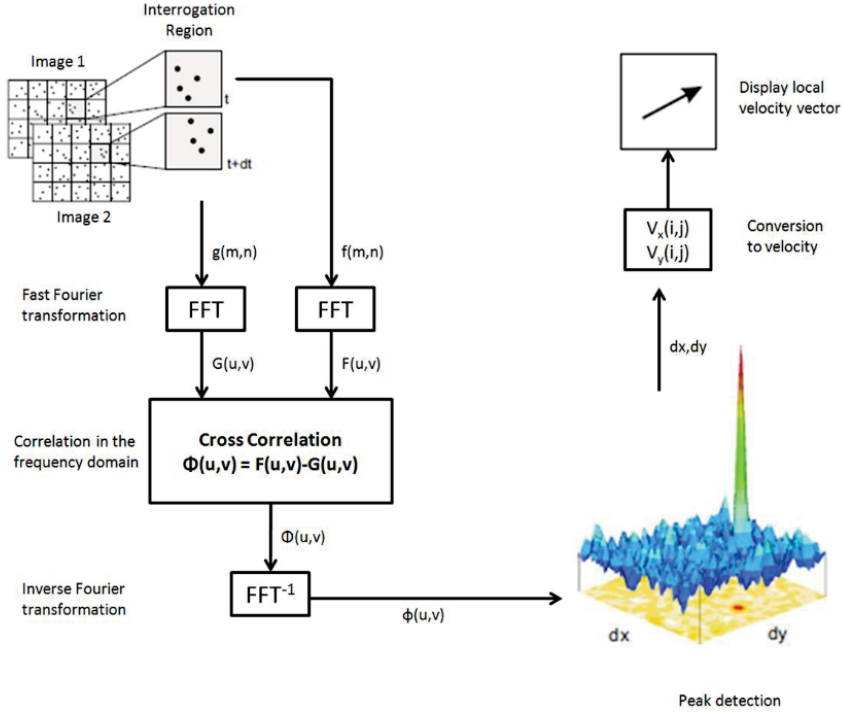
Figure 8. Diagram of cross correlation process [11]

2.3 Particle Sizing, Generation, and Shock Response

2.3.1 Classification of Particle Diameters

Particle diameter is an extremely important characteristic for determining both the reflected light and responsiveness of the particle. Thus, when considering a seed material, it is critical to be able to accurately measure and classify particle diameters. Prior research at AFIT has identified two ways of classifying particle diameter size. Liber [11] used Particle Shadow Velocimetry (PSV) to approximate particle diameter. This techniques involves the use of a Light-Emitting Diode (LED) to back-lit particles and capture their projected shadows. The results of this technique are 2D projections of non-spherical dry ice particles which can be seen in Figure 9.
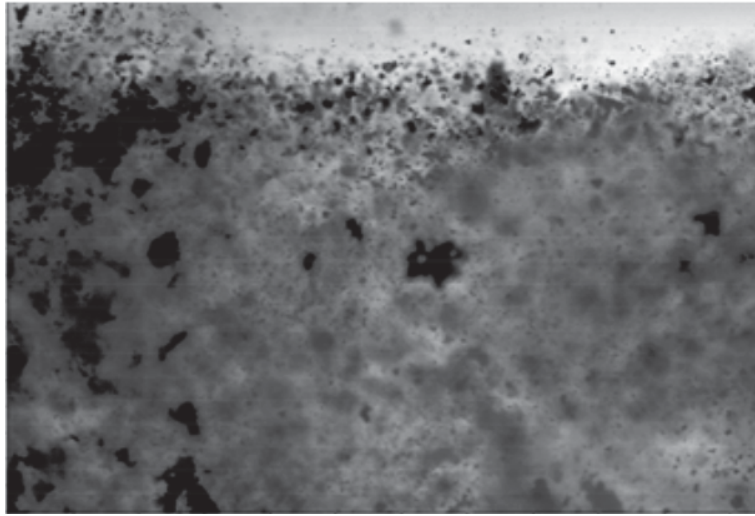
Figure 9. Example of particle shadow velocimetry on dry ice particles [21]

Liber [11] applied the following approximation of particle diameter, d_p, by using the projected area A.

$$d_p = \sqrt{\frac{4A}{\pi}} \tag{12}$$

Love [12] used a Malvern Spraytec particle size analyzer to collect data on particle sizes. The Sauter mean diameter, D_{32}, is a convenient method for describing the mean diameter of an equivalent sphere.

$$D_{32} = \frac{\sum_{i=1}^{N} n_i D_i^3}{\sum_{i=1}^{N} n_i D_i^2} \tag{13}$$

In the equation for Sauter mean diameter, n_i, is the total number of particles and D_i is each particle diameter. This metric is particularly convenient when comparing results of this research to previous to previous sizing data collected at AFIT.

Love [12] also used an indirect method of approximating particle size by measuring the particle response across the shock and comparing it to theoretic particle diameters. The experimental method for determining particle response will be presented in section 2.3.3 , however both the Malvern Spraytec and the Particle response experiments performed by Love [12] indicated that carbon dioxide particle diameters were around 2-3 microns.

2.3.2   Previous CO_2 Particle Generation Techniques

Content in this section summarizes the advancements in AFIT-based CO_2 particle generation since 2008 developed by researchers Greene [8], Love [12], Wolfe [24], and Liber [11].Liber [11] provides a good summary of research done prior to 2008. Principally, CO_2 particles have been generated in a very similar way, and the various researchers have explored different variables, which could affect the size and dispersion of the CO_2 particles.

Particles start as highly-pressurized liquid carbon dioxide $CO_{2(l)}$ in a large tank.

Driven by pressure from the tank, $CO_{2(l)}$ is siphoned off via a metal hose, which routes the liquid to the location of interest. This metal hose is linked to a small diameter feed tube interfacing with a nozzle. This nozzle is connected to a larger diameter shroud tube. At the interface between the nozzle and the shroud tube, the $CO_{2(l)}$ rapidly expands and simultaneously decreases in temperature. The result of this rapid expansion is a two phase solid $CO_{2(s)}$ and gaseous $CO_{2(g)}$ mixture, which is ejected from the shroud tube into the surrounding atmosphere [11]. Figure 10 shows the generation process starting from the feed tube.
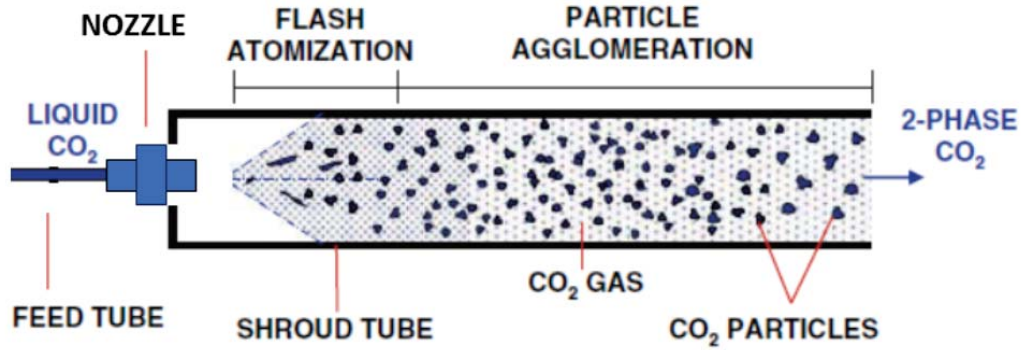
Figure 10. Schematic of dry ice particle generation [21]

In 2008, Greene [8] explored different configurations of shroud tube and feed tube lengths, as well as their respective inner diameters. Greene's results, based on measurements using the Malvern Spraytec system, revealed that the following manipulations resulted in increased particle size: increasing shroud tube length, increasing inner diameter of the shroud tube, and decreasing the inner diameter of the feed tube.

More research in the control of particle size followed in 2010, when Love [12] compared the effects of a standard shroud tube with a more advanced tube containing an embedded mixing device. He found that the mixing tube produced significantly smaller particles but was prone to clogging issues. He also attempted to regulate the shroud temperature, but found that it produced negligible effects on particle sizing.

Wolfe [24] was able to extend the CO_2 research to the Tri-sonic Gas Dynamics facility in 2012. Particles were ejected into the settling chamber of the wind tunnel, and dispersed via an eight-shroud tube manifold. Results from tests in the operating wind tunnel confirmed Greene's [8] assertion that increased shroud tube size leads to increased particle size. Unlike his predecessors, Wolfe was also able to determine some trends regarding the effects of freestream conditions on particle size. He found that increased stagnation pressures within the tunnel decreased the sublimation rates of the CO_2 particles. Also, operating the tunnel at higher velocities gave particles less time to sublimate — preserving larger particle sizes at the test section.

Figure 11.   Shroud Tube manifold developed by Wolfe for use in TGF [21]

In 2014, Liber [11] augmented the Shroud-Tube nozzle interface by including another injection tube which delivered gaseous $CO_{2(g)}$ and increased the overall mass flow rate exiting the shroud tube. A visual representation of this augmentation, when opened in a humid atmosphere, can be seen in Figure 12. Researchers concluded that,

as the injected mass flow rate increased, particle size was decreased. Particle size regulation was also attempted using external stainless steel meshes; however, severe clogging issues hampered data collection.
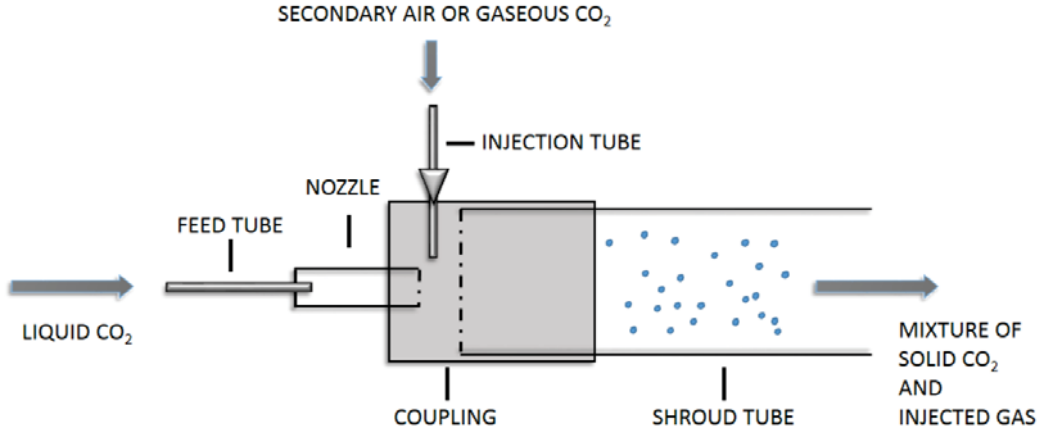
Figure 12. Shroud tube with injected $CO_{2(g)}$ [11]

In summary, CO_2 particles can be generated using any number of shroud tube configurations. Configuration variables such as shroud diameter, feed tube diameter, mixing devices, and gaseous injection have been shown to alter particles sizes. Freestream conditions such as stagnation pressure and velocity also play a large role in the rate of sublimation, as well as the residency time associated with the particles generated.

2.3.3 Particle Response Across a Shock

Though significant research has been devoted to determining particle size, the performance of the particle is ultimately what determines its applicability to a flow situation. One method for measuring particle response is to subject the particle to a supersonic shock. A shock is a relatively thin accommodation region within a supersonic flow, which signifies an abrupt change in both density and velocity. Air molecules, which are significantly smaller and less dense than any seed particle,

experience a near asymptotic drop in velocity, as they cross the shock. However, tracer particles of any kind will experience a transition which resembles an exponential decay. As particle size increases, the exponential decay becomes less and less asymptotic, and particle lag becomes more apparent. This phenomenon can be seen in Figure 13.
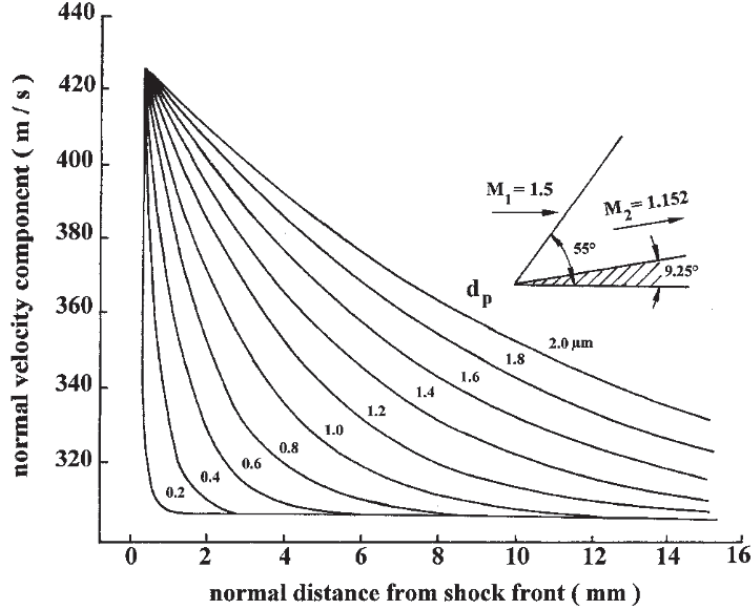
Figure 13. **Graph showing increased particle sizes resulting in particle lag across and oblique shock [14]**

Recalling from section 2.1.3, Characteristic frequency, C, and characteristic response time, τ_p, which can be described by following equation.

$$C = \frac{3}{4}C_D Re_p \frac{\mu}{\rho_p d_p^2} = \frac{1}{\tau_p} \tag{14}$$

For a particle in a fluid subjected to an oblique shock, the following relationship is given by Ragni [18]:

$$\frac{u_n - u_{n2}}{u_{n1} - u_{n2}} = e^{-Ct} = e^{\frac{-t}{\tau_p}} \tag{15}$$

where u_n is given by the following equation:

25

$$u_n = u_{n2} + (u_{n1} - u_{n2})e^{-1} \qquad (16)$$

In equations 15 and 16, u_n represents the particle velocity normal to the shock. Velocities u_{n1} and u_{n2} signify the upstream and downstream normal velocities respectively. This can be seen visually in Figure 14.
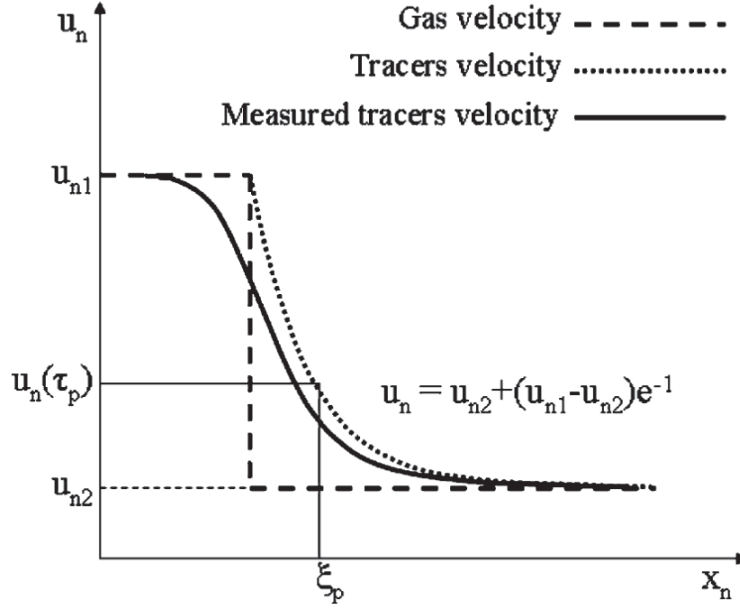
Figure 14. Graph depicting particle response parameters across an oblique shock [18]

With some integration and manipulation, Equation 15 can be used to produce an equation for, x_n, which describes the particle position normal to the shock:

$$x_n = u_{n2}\tau_p \ln\left(\frac{u_{n1} - u_{n2}}{u_n - u_{n2}}\right) + \tau_p(u_{n1} - u_n) \qquad (17)$$

A relationship also exists to describe a relaxation length, ξ_p, which is related to the characteristic time τ_p [18]. This relationship is given as:

$$\xi_p = \tau_p(u_{n1} + (u_{n1} - u_{n2})e^{-1}) \qquad (18)$$

26

Equation 18 can also be linearly approximated by the following relationship [18]:

$$\frac{-t}{\tau_p} \approx \frac{x_n}{\xi_p} \tag{19}$$

Equation 19 allows the experimentalist to compute τ_p using both the relaxation length and the velocity distribution data gathered from a PIV vector map [18].

As indicated by Figures 13 and 14, Particle response data is typically displayed as V_{norm} or the velocity normal to the shock and plotted against the distance normal to the shock where the zero point coincides with the shock location. However, velocity data is typically collected in terms of its horizontal and vertical components. The conversion from the U (horizontal velocity component) and V (vertical velocity component) is given by the following equation [12] :

$$V_{norm} = U \sin\beta + V \sin\beta \tag{20}$$

Love [12] performed a particle response experiment using a 10 degree ramp in the AFIT Supersonic 6"x6" wind tunnel and was able to resolve the resulting shock using carbon dioxide particles. A snapshot of results obtained by Love [12] are displayed in the Figure 15 as a contour of normal velocity.

As a means to indirectly characterize the size of the carbon dioxide particle, Love [12] plotted data against theoretical curves graphed using equations 14 and 17. Theoretical curves given in Figure 16 assume particle diameters of 1.0, 2.0 , and 3.0 microcrons and the density of solid carbon dioxide 1.18 g/cm^3. As Figure 16 suggests, particles seemed to follow a theory curve of about 2 microns.

While this experiment met with success, several complications hampered data collection. Shlieren visualization showed that weak shock waves associated with boundary layer structure might have led to variation in the location of the oblique shock
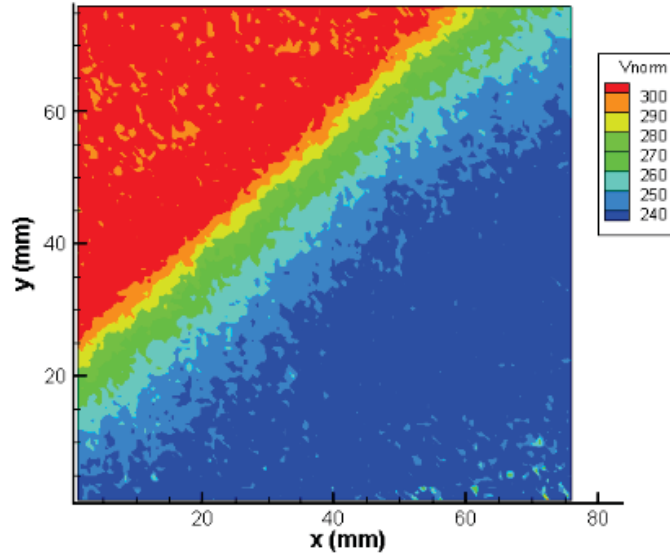
Figure 15. **Velocity Normal to the shock collected by Love [12] using 64x64 pixel IR**
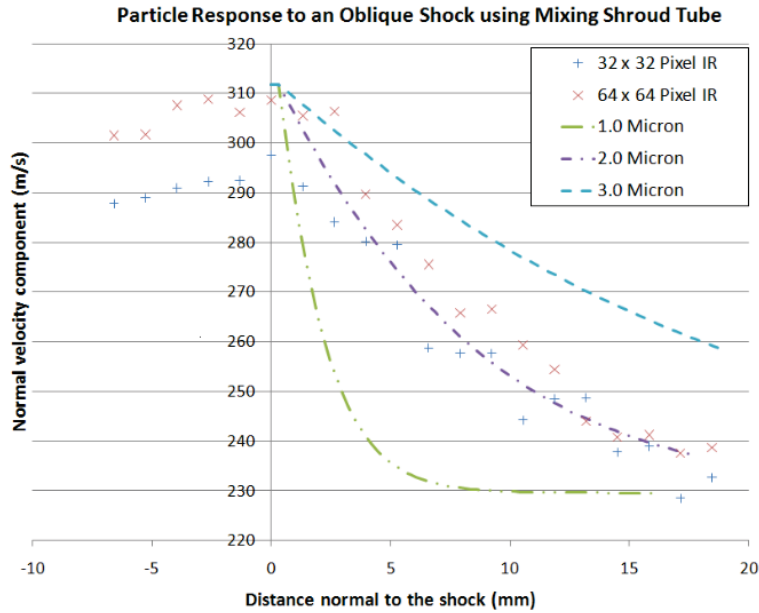
Figure 16. **Particle response plot collected by Love [12] IR**

wave within the region of interest. In summary, the fact a ramp was used instead of a suspended wedge, left some doubt as to whether or not boundary layer interactions may have also interfered with Love's results. [12] In this research a half-wedge was

utilized to avoid similar complications.

Researchers outside of AFIT have used this method to measure the Particle Responses of non-carbon dioxide particles. Beresh et al [5] conducted a particle settling velocity experiment in 2014 to test a custom particle seeder producing a particle seeder producing 1.5 micrometer particles for use in a Lockheed Martin Transonic Wind Tunnel. This test was used to verify that particles produced a sufficiently small stokes number to track local velocity gradients [5]. Ragni et al.[18] published a journal article in 2011 which compared the particle responses of several particle types including liquid DEHS, solid silicon particles, and solid titanium dioxide particles. These particles measured diameters of 12 to 550 nano meters and acclimated to a shock wave velocity gradient within 3 mm normal to the shock [18]. In an article by Williams et al. [23], the validity and variability of particle responses based on the strength of the shock wave is examined. Particles used in their experiments were Kronos 3333 titanium dioxide particles with diameters of 20 nanometers which were tested in particle response experiments between Mach 2 and Mach 10 [23]. Thus, there is clear precedence and interest in this particle response experimental method as a means for describing particle performance.

2.4 Fundamental Compressible Flow Relations

In a well designed wind tunnel operating with dry air, several isentropic relations can be used to approximate the freestream conditions within that tunnel. Mach number is defined as [3]

$$M = \frac{V}{a} \tag{21}$$

where "V" is velocity and "a" is the speed of sound. The speed of sound for a calorically perfect gas is [3]:

$$a = \sqrt{\gamma R T} \tag{22}$$

For dry air, the specific gas constant is R= 287 J/kg-K and the ratio of specific heats is γ= 1.4. If the gas constant and γ are held as constants, then the speed of sound varies only with the freestream temperature T. This freestream temperature can be approximated using the Mach number and a total temperature T_o via the following equation [3]:

$$\frac{T_o}{T} = 1 + \frac{\gamma - 1}{2} M^2 \tag{23}$$

If the flow is assumed to be isentropic, that implies that it is also adiabatic and that the stagnation temperature is conserved. So if stagnation temperature and Mach number are known, freestream velocity , V , can be approximated by the following equation [3]:

$$V = M \sqrt{\frac{\gamma R T_o}{1 + \frac{\gamma-1}{2} M^2}} \tag{24}$$

When an object with a constant deflection angle θ is introduced to a supersonic flow, a shock wave is generated with a wave angle β. The relationship between θ, β, and the Mach number is called the θ-β-Mach relation which following relation [3]:

$$tan\theta = 2cot\beta \frac{M_1^2 sin^2\beta - 1}{M_1^2(\gamma + cos2\beta) + 2} \tag{25}$$

Using this relation, a Mach number can be numerically approximated if θ and β are known. The θ and β angles are used in the following equations describing the Mach number normal to the shock and prior to the shock $M_{n,1}$, the Mach number normal to the shock and after the shock $M_{n,2}$, and the non-normal post shock Mach number M_2 [3].

$$M_{n,1} = M_1 sin\beta \tag{26}$$

$$M_{n,2} = \sqrt{\frac{1 + \frac{\gamma-1}{2}M_{n,1}^2}{\gamma M_{n,1}^2 - \frac{\gamma-1}{2}}} \tag{27}$$

$$M_2 = \frac{M_{n,2}}{sin(\beta - \theta)} \tag{28}$$

Temperature rises across an oblique shock. T_1 is the temperature of the freestream upstream of the shock and T_2 is the temperature of the freestream following the shock. The relationship with respect to Mach number for a perfect gas is:

$$\frac{T_2}{T_1} = [1 + \frac{2\gamma}{\gamma + 1}(M_1^2 - 1)]\frac{2 + (\gamma - 1)M_1^2}{(\gamma + 1)M_1^2} \tag{29}$$

Using T_1 and T_2 as the freestream temperatures before and after the shockwave, the normal velocity before the shock, V_{n1}, and after the shock , V_{n2}, can be approximated by the following equations:

$$V_{n1} = M_{n,1}\sqrt{\gamma R T_1} \tag{30}$$

$$V_{n2} = M_{n,2}\sqrt{\gamma R T_2} \tag{31}$$

2.5   Non-Isentropic Condensation Effects

In modern wind tunnels dryers are used to ensure that dry air enters a wind tunnel and well known relations can be easily applied. For that reason, little research has been done since the 1960's on the subject of condensation in supersonic nozzles. However, from the 1930's to the 1960's significant research was conducted on the sub-

ject which documents some of the behavior of moist air through a supersonic nozzle. A brief summary is provided in this section, for a thorough account of these effects refer to Wegener and Mack [22]. This discussion is included in this thesis, because ambient water particles were detected during wind tunnel testing. Thus research was conducted to understand possible implications of the presence of moisture content within a supersonic nozzle.

The first researchers of condensation phenomena reported the appearance of shock-like structures appearing just downstream of the nozzle throat [22]. As moist air expands in a supersonic nozzle, the relative humidity of the moist air increases dramatically as the Mach number rises. The water vapor reaches a supersaturated state and then collapses. Water vapor is supercooled and condenses into liquid droplets or ice particles while heat is released into the air [22]. This process can occur over a very short distance, and can look very similar to an oblique shock. Due to their appearance, these condensation based disturbances were initially a called "Condensation Shocks", though the phenomenon is not actually a shockwave [22].

There are several metrics for expressing water vapor content in air. One metric is the relative humidity, Φ , defined as the following:

$$\Phi = 100\frac{p_v}{p_\infty} \tag{32}$$

where p_v is the partial pressure of water vapor and p_∞ is the static pressure. As relative humidity increases, the strength of the "condensation shock" also increases and the onset of the condensation shock occurs closer to the throat and at a lower Mach number[22]. Figure 17 shows the Mach number at which the condensation occurs as it correlates to relative humidity. Note that for high Mach numbers, condensation shocks can occur at low relative humidities.

Condensation shocks are inherently non-isentropic and are modeled in conden-
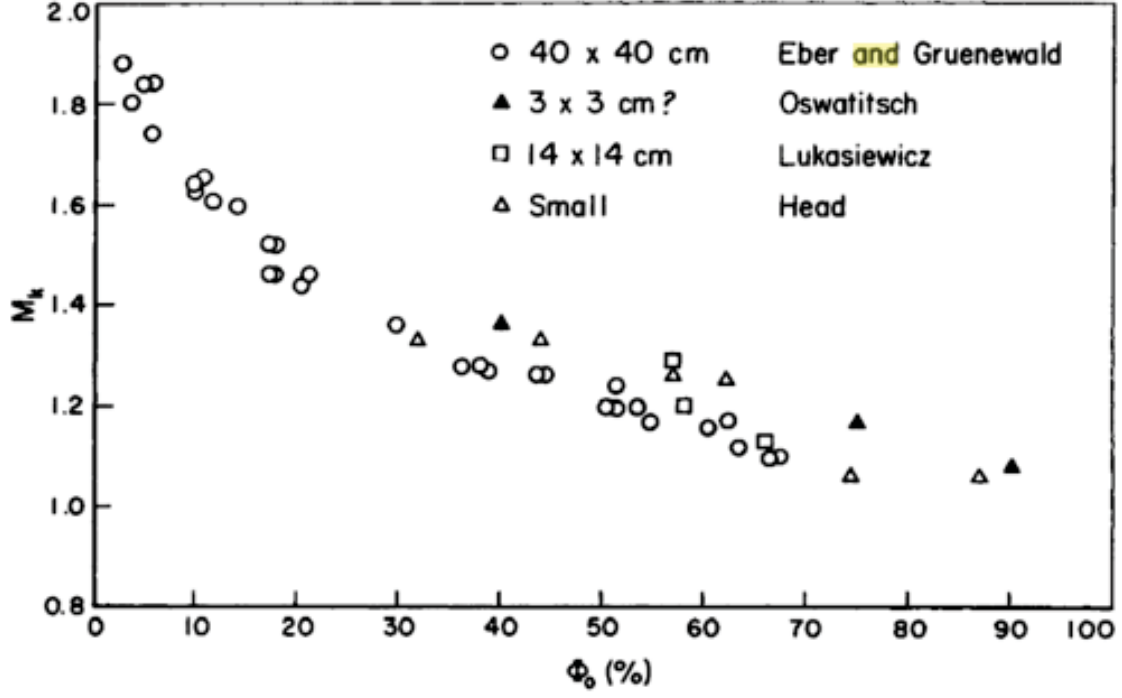
Figure 17. Mach number at which condensation occurs plotted against initial relative humidity [22]

sation shock theory as heat released into a flow. This heat added is expressed by Wegener and Mack [22] as a ratio $\frac{Q}{Q_{max}}$. Q is itself a ratio of heat released per unit mass via condensation, q, and the energy per unit mass already present in the flow. Q_{max} is the dimensionless quantity representing the maximum Q value at a given Mach number. Wegener and Mack [22] express Q and Q_{max} in the following equations:

$$Q = \frac{q}{c_p T_{O1}} = \frac{T_{01}}{T_{02}} - 1 \tag{33}$$

$$Q_{max} = \frac{(M_1^2 - 1)^2}{2M_1^2(\gamma + 1)(1 + \frac{\gamma - 1}{2}M_1^2)} \tag{34}$$

The heat added q via condensation is given as [22]:

33

$$q = \frac{m_v}{m_a + m_v}L \tag{35}$$

where m_v is the mass of water vapor, m_a is the mass of air, L is the latent heat of vaporization, T_{01} is the initial stagnation temperature, and T_{02} is the stagnation temperature after the condensation shock [22].

While stagnation temperature is shown to increase due to a condensation shock, stagnation pressure is will ultimately decrease following a condensation shock [22]. Figure 18 shows this effect in terms of Mach number and $\frac{Q}{Q_{max}}$.
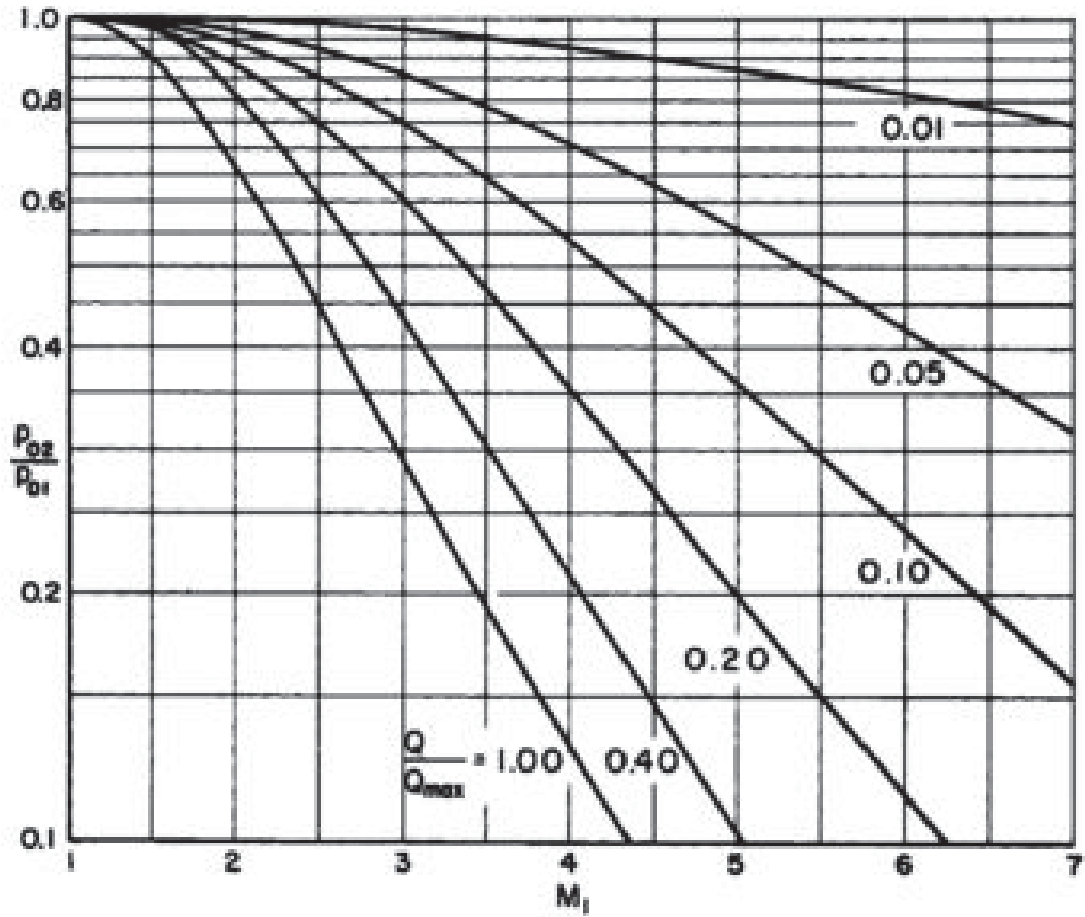
Figure 18. $\frac{p_{O2}}{p_{O1}}$ plotted with curves of $\frac{Q}{Q_{max}}$ as function of Mach number [22]

Based on the continuity equation, the equation of state, and the speed of sound,

it was shown by Wegener and Mack [22] that downstream of the condensation shock, the area required for sonic flow, A^*, increases as stagnation pressure drops and heat is added. The following relationship presented by Wegener and Mack [22] shows this principle:

$$\frac{A_2^*}{A_1^*} = \frac{p_{01}}{p_{02}}\sqrt{1+Q} \tag{36}$$

where A_1^* and A_2^* are the areas required for sonic flow before and after the condensation shock respectively. An expression which represents the effects of condensation in terms of the ratio $\frac{A_2^*}{A_1^*}$ is given by Wegener and Mack [22] as:

$$\frac{A_2^*}{A_1^*} = \frac{M'}{M}\left[\frac{1+\frac{\gamma-1}{2}M^2}{1+\frac{\gamma-1}{2}M'^2}\right]^{\frac{\gamma+1}{2(\gamma-1)}} \tag{37}$$

A graphical representation of this expression is also presented in Wegener and Mack [22] and can be seen in Figure 19.

In addition to condensation shock theory, Wegener and Mack [22] present quantitative descriptions of condensation effects downstream of the condensation shock. They note the following in regards to condensation effects:

" ...we find that at higher humidities the entire flow appears to be foggy downstream...At lower humidities the fog droplets are less dense and initially smaller, particularly in short nozzles. However, the droplets can be made visible when a collimated beam of light is passed through the nozzle. Light scattering investigations show the fog to appear rather abruptly downstream from the location of the condensation shock..." [22]

In summary, the presence of moisture in a supersonic wind tunnel can lead to a phenomenon known as a condensation shock. This phenomenon causes both a decrease in stagnation pressure and an increase in stagnation temperature due to a
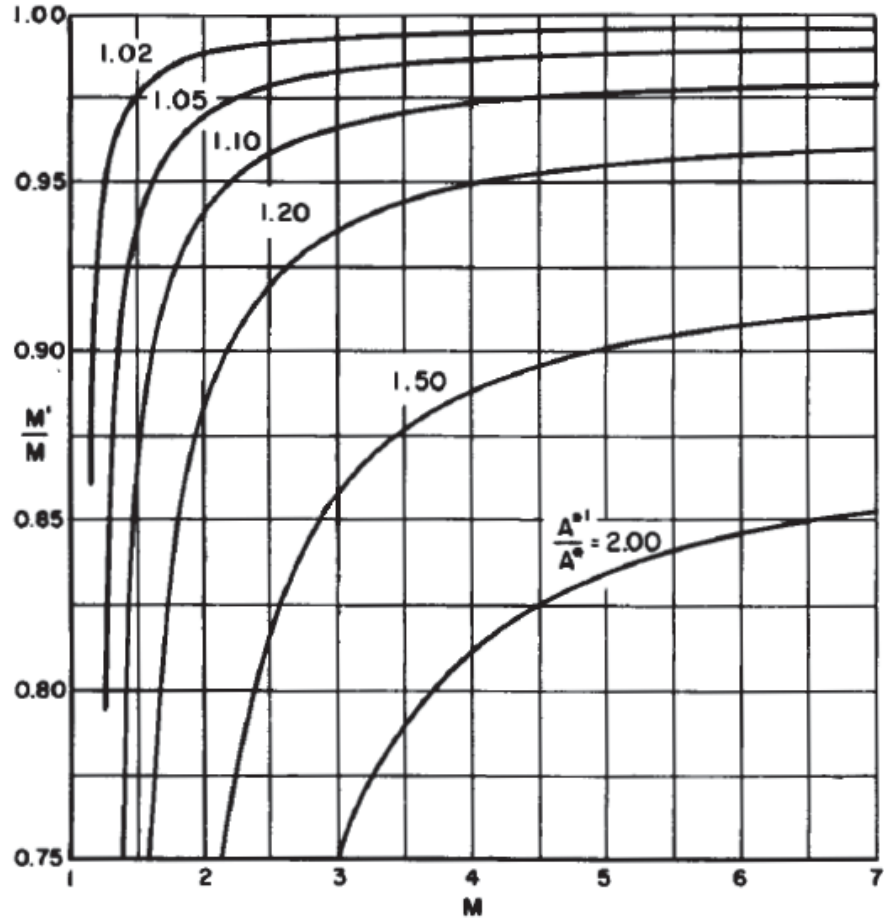
Figure 19. $\frac{M'}{M}$ **plotted with curves of** $\frac{A_2^*}{A_1^*}$ **as function of Mach number [22]**

sudden collapse of supersaturated water vapor. Following a condensation shock, the presence of fog or water droplets visible by collimated light can be expected, as well as a drop in the test section Mach number.

III. Research Methodology

3.1 Experimental Concept Overview

In order to determine the particle response of carbon dioxide and other particles, a relatively simple experiment using a 15 degree half-wedge in a Mach 3 flow was performed. Particles of a given size and density will theoretically acclimate to the sudden change in velocity induced by a shock wave within a certain distance "s" on a path normal from the shock. Figure 20 below gives a pictorial representation of the experimental concept.
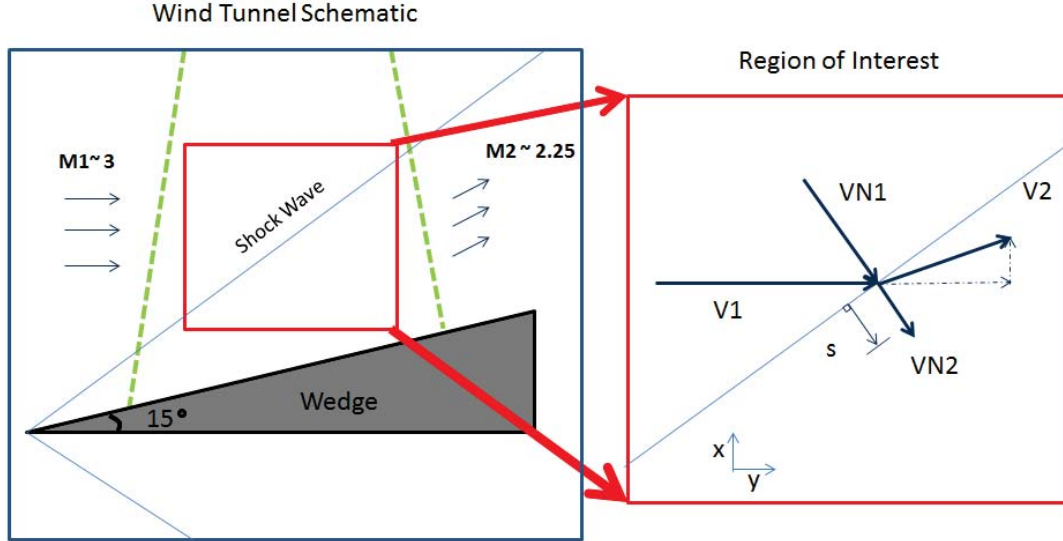
Figure 20. Diagram of experimental concept

Supersonic flow over a wedge is quasi two dimensional in nature, and therefore a classical, single camera, two dimensional PIV configuration was adequate to examine the flow over the wedge. A laser sheet was inserted on the topside of the wedge with a camera perpendicular to the laser sheet and the flow. The evaluation of three different particle types was attempted including: solid phase carbon dioxide particles, condensed water particles, and oil particles. Two different lenses with different

37

magnifications were also used to categorize the effect that increased magnification would have on examining particle response. A region of interest containing the shock wave was examined using Averaged Cross Correlation, Adaptive PIV, and the Least Squares method. Various parameters within those two methods were explored to categorize the effects on particle response and measurement accuracy.

3.1.1 Mach 3 Tunnel Overview

The Mach 3/Mach 6 Facility (M3M6F) is located on Wright Patterson Air Force Base. As the name implies, the facility features both a Mach 3 tunnel as well as a Mach 6 tunnel. Research included in this thesis was conducted exclusively in the Mach 3 tunnel. The M3M6F is a high Reynolds number facility designed to operate at a stagnation pressure of 570 psia, stagnation temperature of 500 degrees Rankine, and a mass flow rate of 200 lbm/sec [9]. Table 1. describes the operational ranges and capabilities of the Mach 3 tunnel.

Mach Number	3.0 (2.98 measured during facility calibration)
Storage pressure	1000 to 3000 psia
Storage temperature	Ambient (no heat sink)
Mass flow range	10 to 200 lbm/sec
P_0 range	20 to 600 psia Poor flow quality experienced below 85 psia
Starting time	3 sec
Run time	60 sec at 200 lbm/sec flow rate (based on a 7000 ft^3 storage volume

Table 1. Mach 3 wind tunnel operating conditions [9]

This tunnel operates in a "blow down" configuration in which high pressure air is stored in a series of tanks outside of the facility [9]. Pressurized air is relieved through the test section and exits via a pressure relief stack located on the facility

exterior. Figure 21 is a diagram of the portion of the wind tunnel which is located on the inside of the facility.
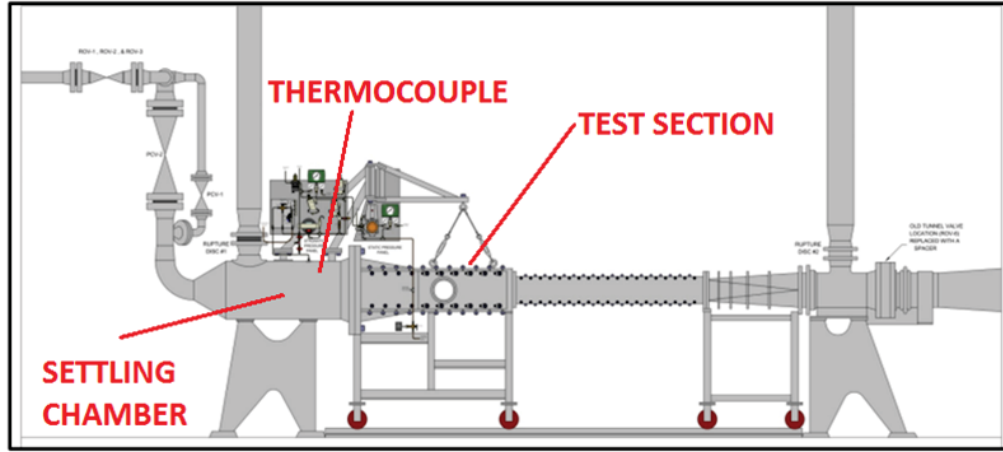
Figure 21. Wind tunnel diagram, side view [9]

Prior to modification, the test cabin had multiple options for optical access on both sides. This provided several options for PIV camera configurations. However, the tunnel's lack of optical access from either the top or bottom was a limiting factor.

During the experiment, a fixed sting model support was used to suspend a 15 degree half wedge within the flow. The tunnel operated nominally at Mach 3 with velocities around 570 m/s in the freestream. Stagnation temperatures were maintained at 100 psi, and stagnation temperatures ranging from 250-260 K were measured via a thermocouple in the settling chamber. The AFRL/RQ team of tunnel operators used valve control while monitoring stagnation pressure to enable wind tunnel experiments which lasted between 60 to 150 seconds depending on the run.

3.1.2 Tunnel Modification for PIV

Without optical access from the top of the test section, laser sheet introduction into the test section would be less than ideal. However, the top of the tunnel included a removable circular block which provided a feasible entryway for the laser if properly

modified. Therefore, a significant effort was made in collaboration with the AFIT
Model Shop and Engineers at AFRL RQVX to design, fabricate, and implement a
modified version of the circular block which included a small window for laser sheet
optical access. Figure 22 shows the top of the test section prior to modification.
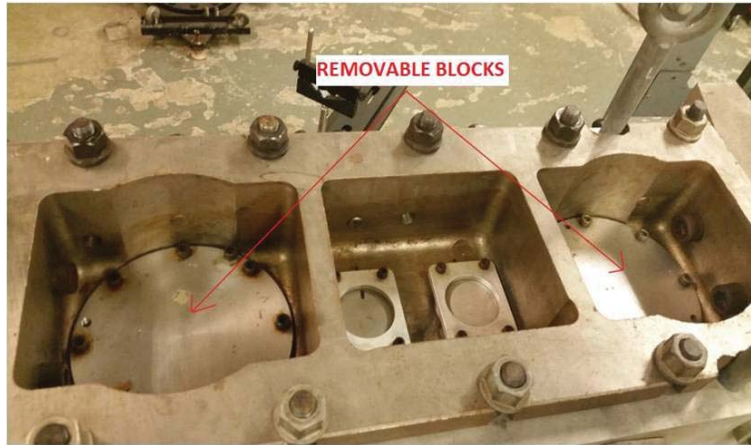
Figure 22. Top of test section prior to modification

Based on drawings provided by AFRL RQVX, the author redesigned and provided
engineering drawings for a modified block which included a high grade quartz window
acquired from Quality Quartz Engineering in Dayton. In collaboration with AFRL
RQVX, the redesigned block underwent structural analysis and was deemed safe for
use in the tunnel. The modified block was then machined by the AFIT model shop,
assembled and seated by members of AFRL RQVX team, and placed in the tunnel
for use. Figure 24 shows the modified block installed into the wind tunnel as viewed
from inside the test cabin.

Figure 23. Modified window viewed from cabin interior

3.2 Experimental Set Up

3.2.1 Camera and Laser Configuration

Wind tunnel experiments were conducted in the test cabin of the Mach 3 tunnel. An AD20 support structure was constructed on an optical table positioned near the tunnel test section. This support structure was designed to maintain the position of both the CCD camera and a light arm which redirected the light emitted from a laser resting on the optical table. The optical table was carefully positioned such that no portion of the base was resting beyond the vibration isolation fault on the floor of the facility. The camera was mounted perpendicular to the flow on the AD20 support structure. Figure 25 shows a side view of the tunnel test section with the camera mounted on the AD20 support structure.

As is partly visible in Figure 24, the light arm is mounted to the AD20 structure and routed above the top of wind tunnel test section. Figure 25 shows the optical access point for the laser entering the tunnel.

The laser used for this experiment was a Litron Nano L200-15 PIV which is a double pulse Nd:YAG laser capable of emitting a 200mJ pulse with a frequency of around 2.5 Hz. The CCD camera used for data acquisition was the Dantec Dynamics

41
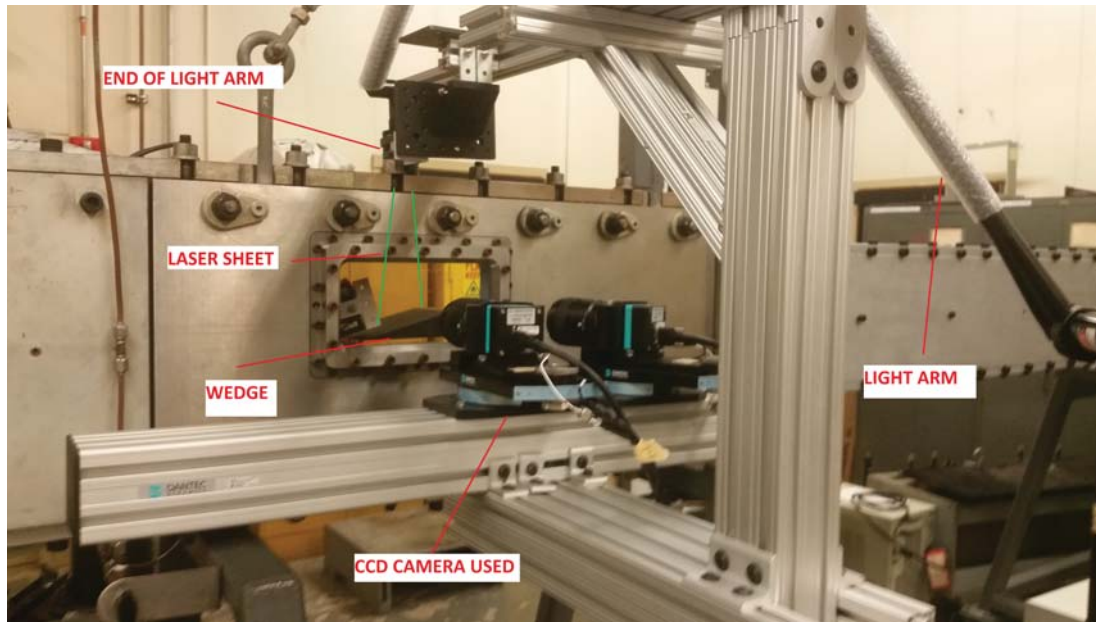
Figure 24. Camera mounting and tunnel configuration. Only left camera was used
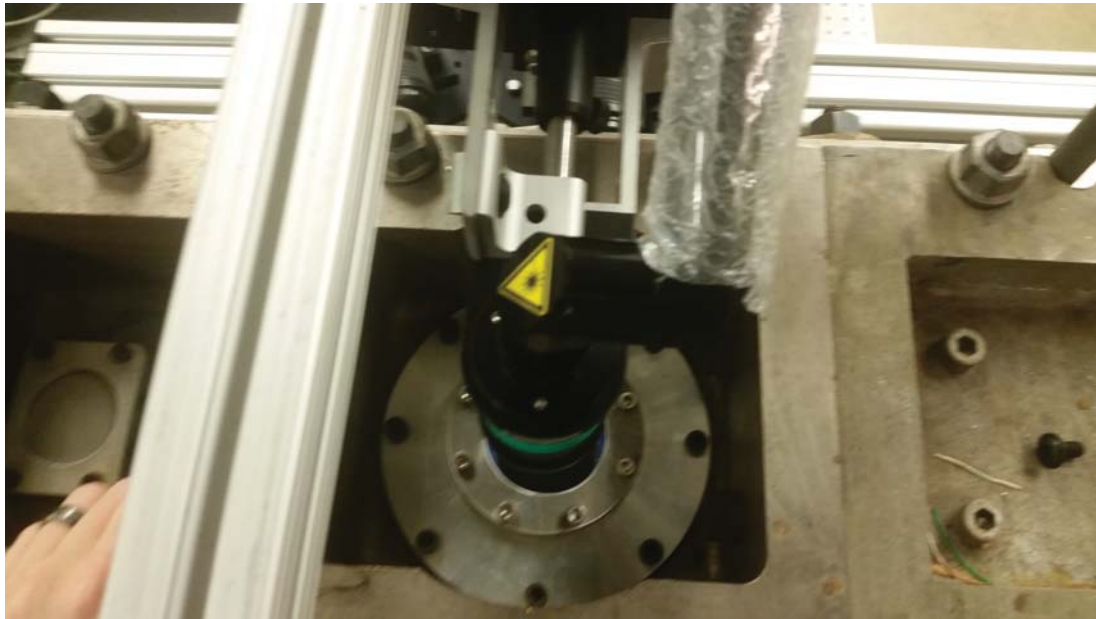
Figure 25. Laser light entry from the top of the wind tunnel test section

FlowSenseEO 11M which records 8-bit images with a resolution of up to 4032 x 2688 pixels. Two different lenses were used during experimentation, a Nikon 60 mm Micro Nikkor lens and a Nikon 105 mm lens. The Δt for all tests was maintained at 500

nanoseconds.

3.2.2 Particle Generation Methods

Particle seeding was attempted from 2 different ports that were present from the initial tunnel design. The upstream port was located on the top of the settling chamber and it permitted the insertion of a 3/8 inch outer diameter tube. It may be noteworthy that for this positioning, a screen was located between the port and the nozzle block. The downstream port was located on the bottom of the settling chamber between the aforementioned screen and the nozzle block. This port only permitted insertion of a 1/4 inch outer diameter tube. Figure 26 shows the location of the two seed ports on the settling chamber.

Figure 26. Upstream seed port (Left) and downstream seed port (Right)

From these injection ports a variety of configurations were tested. Table 2 contains a summary of the configurations attempted. As can be seen in Table 2, only two types of seed were intentionally injected into the flow, carbon dioxide and oil. The oil particles were injected into the settling chamber via a high pressure seeder. Unfortunately this seeder failed to produce noticeable seed at the test section. This seeder used a 1/4 inch outer diameter tube, with small slits at the end of the tube by which oil particles were supposed to exit. After a few tests running the tunnel, it became apparent from PIV images that no detectable oil seed had reached the cross section. These tests were conducted with a known presence of ambient water particles

(to be discussed in 3.2.3), so the presence of oil seed may have been obscured by other particles. However, following a wind tunnel test, the oil seeder tube was removed and examined. The examination revealed that the small slits where seed was supposed to exit, had been frozen and clogged. Thus, with no evidence of any successful seeding, the effort was abandoned, and results concerning oil particles will be excluded from the results section.

Table of Seeding Test Configurations				
Type of Seed Particle Used	Port Location	Generation Method	Tube Size	Orientation Description
Carbon Dioxide	Down Stream	Simple Shroud Tube	1/4 inch Outer Diameter	90 Degree Bend
Carbon Dioxide	Down Stream	Simple Shroud Tube	1/4 inch Outer Diameter	Long Straight Tube
Carbon Dioxide	Upstream	Simple Shroud Tube	3/8 inch Outer Diameter	Medium Length Straight Tube
Carbon Dioxide	Upstream	Static Mixing Tube	3/8 inch Outer Diameter	Medium Length Static Mixer
Oil	Downstream	Pressurized Oil Seeder	1/4 inch Outer Diameter	Long Straight Tube

Table 2. Table of seeding test configurations

The primary objective of this experimentation was to evaluate the performance of $CO_{2(s)}$ particles. The initial state of dry ice particles, is highly pressurized (approximately 345 Psi) liquid carbon dioxide $CO_{2(l)}$ in a large Dewar which can contain up to 180 liters [11]. When a valve is opened at the Dewar, pressure driven $CO_{2(l)}$ is siphoned off via a metal hose routing the liquid to the settling chamber. Figure 27 shows a picture of the Dewar that the $CO_{2(l)}$ originates from.

The hose is connected to a small atomizer nozzle of the same design used by Wolfe [24] which marks the beginning of particle formation. From the nozzle interface, one of two configurations could be used to form $CO_{2(s)}$ particles, the simple shroud tube or the static mixing tube. For the simple shroud tube, the nozzle interfaces

Figure 27. Dewar used for carbon dioxide seeded experiments
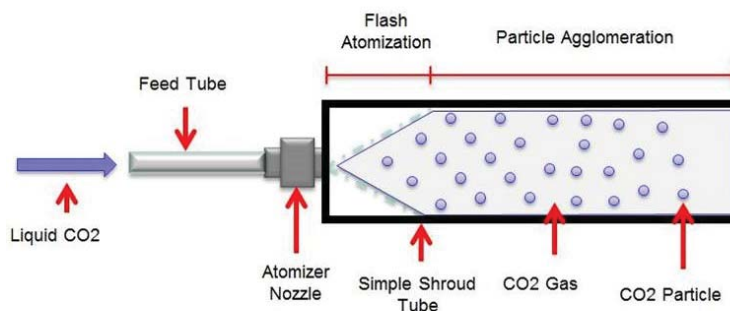
Figure 28. Shroud tube schematic (Top) and reference picture (Bottom)
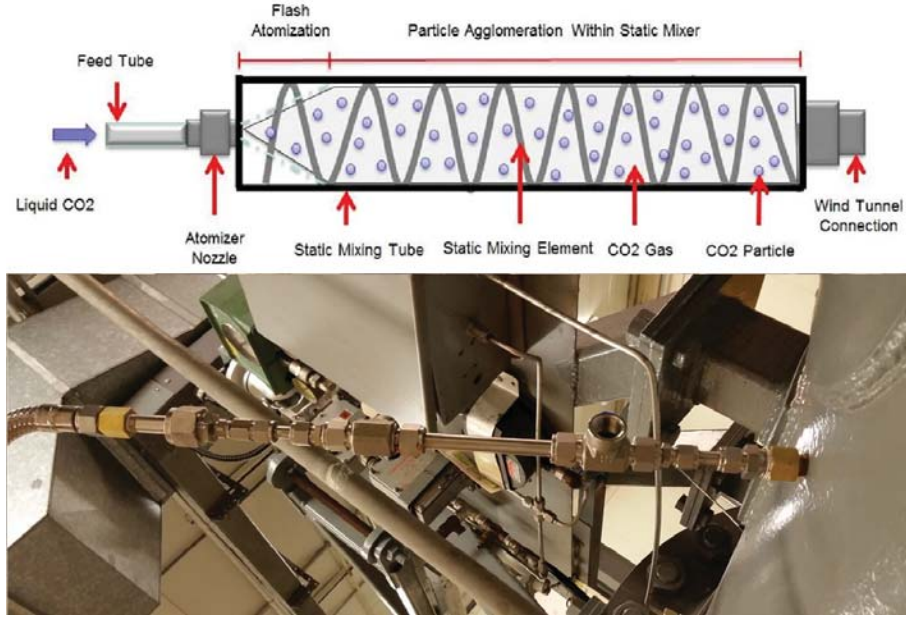
Figure 29. Static mixing tube schematic (Top) and reference picture (Bottom)

with a straight, unobstructed, tube (3/8 or 1/4 inch outer diameter) in which the $CO_{2(l)}$ rapidly expands and simultaneously decreases in temperature. The result of this rapid liquid expansion is a two phase solid $CO_{2(s)}$ and gaseous $CO_{2(g)}$ mixture which is ejected from the shroud tube into the settling chamber. Figure 28 shows the schematic for the simple shroud tube configuration and the actual tube that was used.

The other $CO_{2(s)}$ particle generation method utilizes a static mixer within the shroud tube. The overall process is similar as rapid liquid expansion and particle agglomeration occur within the 3/8 outer diameter tube. However, static mixing elements lead to higher shear rates within the tube. Both of these techniques were used by Love [12]. Figure 29 provides another schematic for the static mixing tube and a reference picture of the actual static mixer used.

3.2.3   The Presence of Ambient Seeding

For this section, please refer to Appendix A for a Full Test Matrix which may be supplemental to this explanation. Wind tunnel testing occurred from January 20th, 2016 to March 11th, 2016. Early test results collected on Febuary 5th produced usable carbon dioxide seeded data. Unfortunately, in the middle of the last run of that day (Run 9 in Appendix A), the tunnel experienced large stagnation pressure fluctuations caused by equipment failure. A hiatus of approximately three weeks was necessary to repair the tunnel.

During this three week time span, outside temperatures shifted from below freezing to above freezing. As was previously noted, high pressure air for the tunnel's blow down configuration is stored in exterior tanks. Testing resumed February 29th through March 1st between which several data collection cycles had passed. During this time seed densities varied significantly, despite consistent application of the same carbon dioxide particle generation technique. It was decided on March 1st (Run 31), that running the tunnel without active seeding could identify the presence of new unintentional seeding.

Running the tunnel without $CO_{2(s)}$ identified a surprisingly densely seeded environment. The leading theory at this time, was that ambient water particles were being detected by imagery data. That theory was solidified by video footage taken of the test section. Figure 30. shows two images, one taken with the tunnel off and one during tunnel shutdown where fog became particularly dense.

The presence of water particles did not abate for the remainder testing (March 3rd through March 11th), which made distinguishing $CO_{2(s)}$ particles from water particles exceedingly difficult. However, the particles provide a valuable comparison to presumed $CO_{2(s)}$ data collected on February 5, prior to the tunnel maintenance period. A comparison of particle images is provided for the reader in Appendix D to
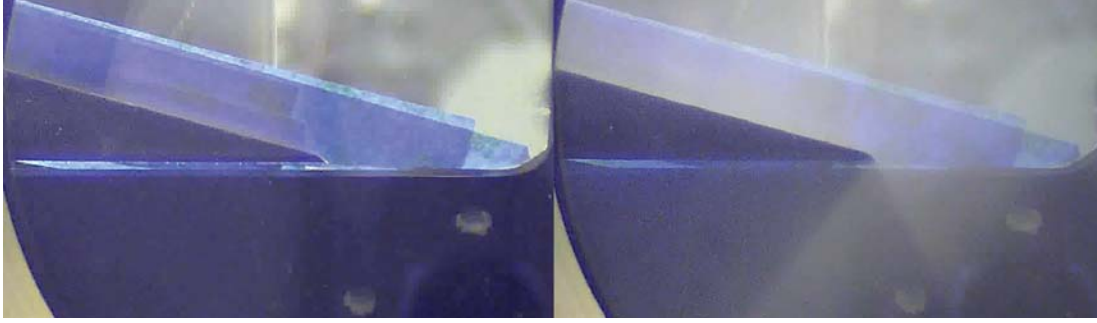
Figure 30.   Images showing the presence of fog in Mach 3 wind tunnel

show the differences between particle images for the all cases examined.

The source of the water particles has not be entirely identified. The following theories have been offered by engineers at AFRL RQVX. The first theory is that the source of the moisture could be residual water in the high pressure tanks remaining from hydrostatic testing that occurred the previous summer. While the tunnel was in frequent operation since the hydrostatic testing, the high pressure tanks are never run completely empty due to the time and energy resources it takes to restore the tanks to an operating pressure. The second theory is that the dryers in the compressors used to pressurize the external tanks could be malfunctioning and introducing moisture into the system. It is also unclear whether the particles are condensing within the nozzle or if the particles are somehow atomized upstream.

3.2.4   Data Acquisition and Calibration techniques

Data was collected and analyzed remotely from the M3M6F control room using Dantec DynamicStudio 2015a software. Timing was controlled through a computer operated BNC Model 575 Timing unit. The time between pulses, Δt, was 500 nanoseconds for all test cases. With the 60mm lens, this led to a pixel shift of approximately 8 pixels in the freestream region prior to the shock wave. With the increased magnification of the 105mm lens the pixel shift was about 12 pixels in the freestream

region.

To properly calibrate the system for data acquisition, the first step was to use a reliable seeding source to focus the lens and set an appropriate F-stop setting. For this purpose exclusively, a TSI Six-Jet Atomizer was set up in the cabin interior to provide a constant particle source that could be easily focused using the DynamicStudio preview functionality. Figure 31 shows a picture of the 6 jet Atomizer set up within the test cabin interior.
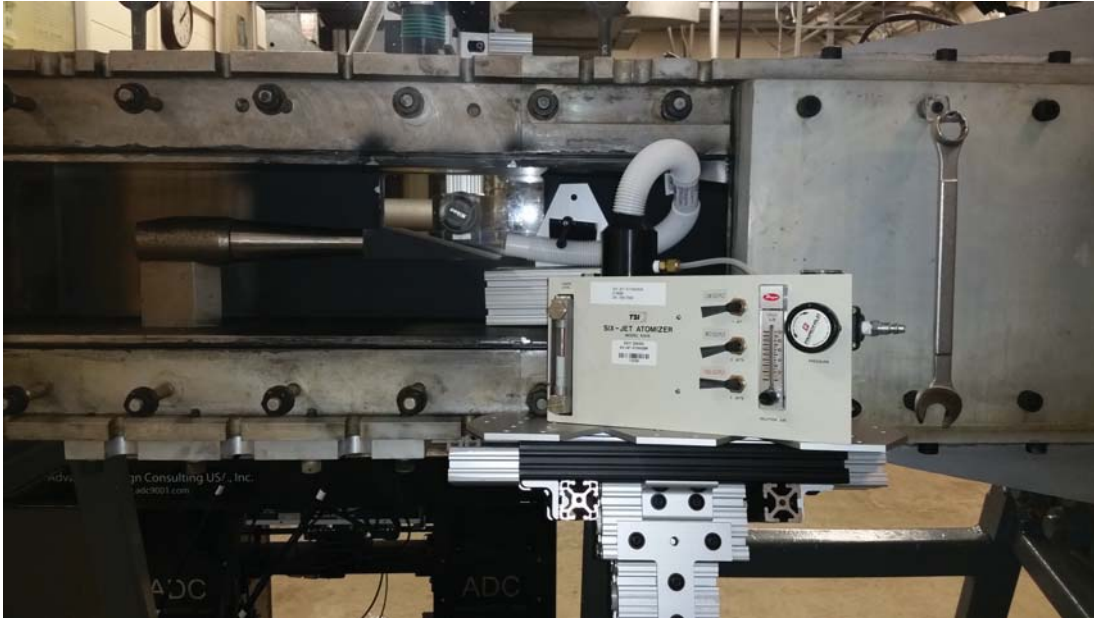
Figure 31.   Calibration configuration with 6 jet atomizer in test section

Once the proper aperture setting and focus was achieved, a calibration image was also required to attain a spacial reference for the DynamicStudio 2015a software. This allows for accurate vector magnitudes to be identified through correlation methods. For a classical two dimensional PIV taking a calibration image is straight forward. An object of known length must be placed precisely in the plane of the laser sheet. A Dantec prescribed calibration dot board was used which has dots spaced 5 millimeters from center to center. The program requests an origin, two other reference points (points A and B), and the absolute distance between those points. From that

information, a scale factor is determined and automatically applied to correlation methods in order to determine vector magnitude. Figure 32 shows points A and B selected within the program used to produce scale factor.
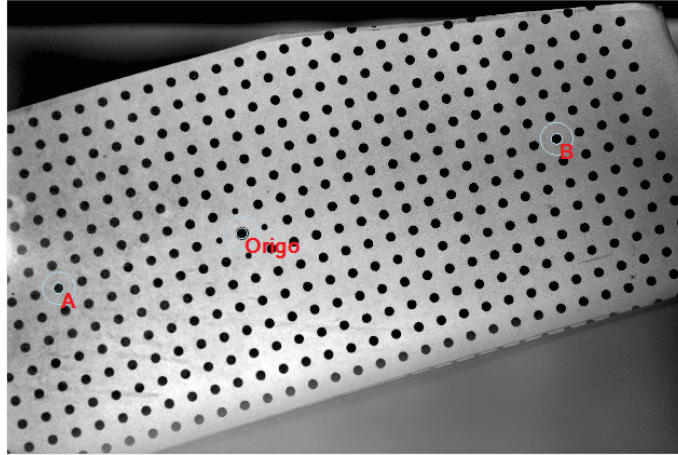
Figure 32. Example of software spacial reference and scale factor identification

A total of three calibration images where taken. The first two calibration images were taken before and after data collection with the 60 mm lens. Predictably, the two independent calibrations produced scale factors that were very similar at around 28 pixels per millimeter. Figure 33 shows a side by side of the pre-test and post-test images taken by the 60 mm lens. The third calibration was taken to measure the scale factor for the 105 mm test cases. The scale factor for the 105 mm lens was approximately 40.5 pixels per millimeter and the image is included in Figure 34.
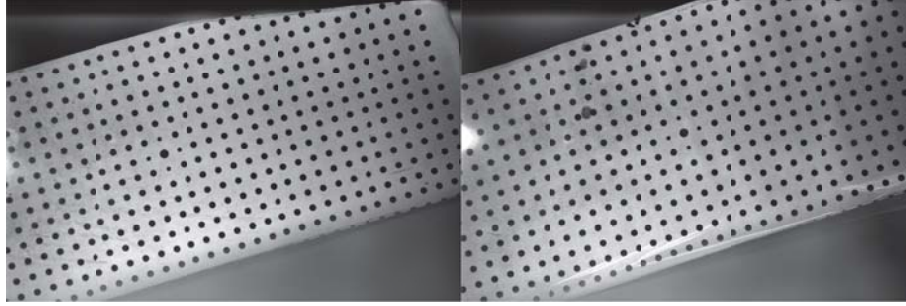
Figure 33. Calibration images taken by 60mm Lens. Pre-test (Left) and post-test (Right). Scale factor for these images is about 28 pixels/mm
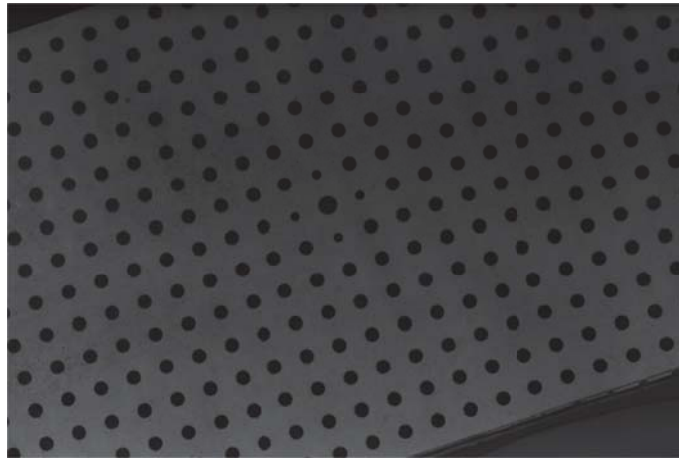
Figure 34. Calibration image taken by 105mm Lens. Scale factor for these images is about 40.5 pixels/mm

3.3 Data Analysis Methods

3.3.1 Correlation Methods

The sudden change in velocity generated by a shock region is a challenging environment for implementation of PIV. Three different analysis methods are explored: traditional Cross Correlation, Adaptive PIV, and the Least Squares Method. These options are all readily available in Dantec DynamicStudio 2015a. Within the software's user interface, there are also several standard features available to manipulate the processing method and presumably affect the accuracy of the results.

51

The first task for applying any of these methods was to identify a region of interest which contained the shockwave. Within the data collections it was reasonably common to have a lighting discontinuity which visually exposes the location of the shock wave. Once a region of interest extraction is identified, the same region was considered for every data set containing images taken with the same lens. Dantec DynamicStudio performs a region of interest extraction by cropping a user identified selection out of every image contained in the designated ensemble. Figure 35 shows the region of interest that was extracted from the 60 mm lens images.
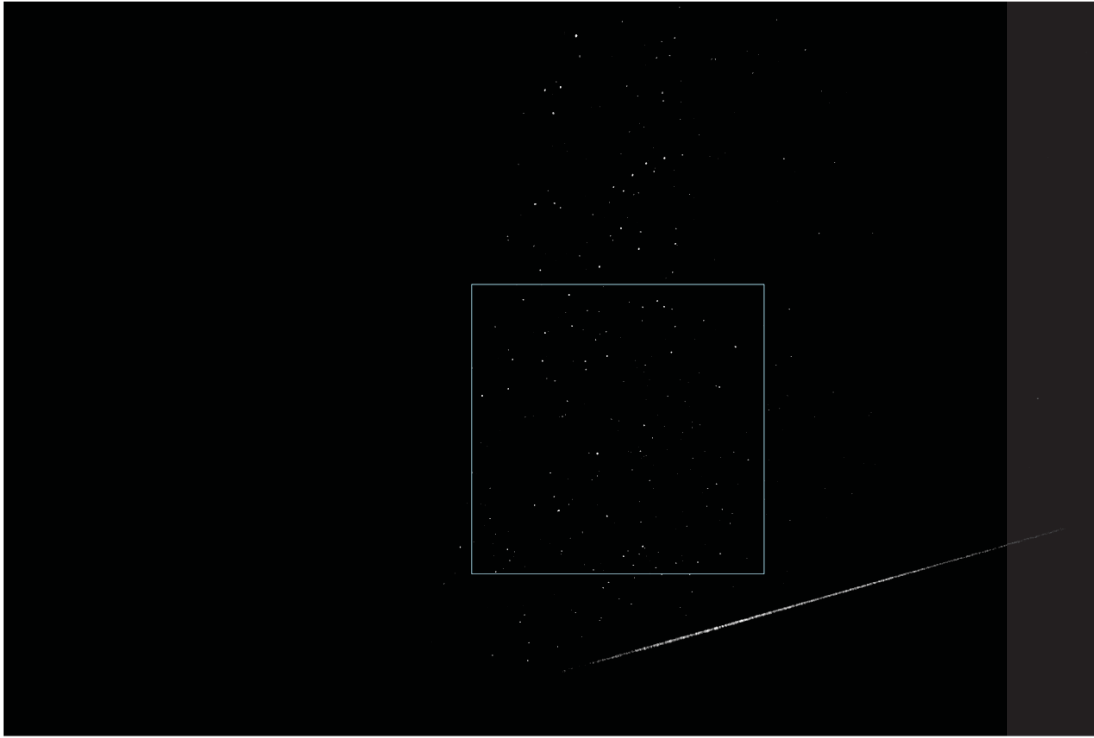
Figure 35. Region of interest extraction taken by the 60 mm lens

Once a region of interest extraction has been made, the image pairs can be analyzed in any number of ways. The first method attempted was the cross correlation technique. This process generates vector maps for each image pair. Within the user interface, many features are available for user input including the fixed interrogation region size, interrogation region overlap, window filtering options such as a Gaussian

window function, and validation methods such as peak ratio validation. After the images have been processed with the user defined customizations, a set of vector maps is produced based on the number of image pairs included in the ensemble. Vectors within these correlation maps can then be further filtered by independent peak validation and range validation functions. After vectors have been adequately filtered, the resulting ensemble of vector maps can then be averaged by the "Vector Statistics" function which produces a single vector map containing the averaged results of all non-filtered vectors. The results of the averaged vector data can be displayed within the program or exported to a text file for analysis in different software.

The Adaptive PIV technique is similar to the traditional cross correlation technique but it is an iterative method which attempts to adapt the interrogation region based on the number of particles it detects and velocity gradients within the flow[7]. For the interrogation region, minimum and maximum interrogation region dimensions can be specified as well as the step size by which it can be adapted. Window filters and peak validation can also be applied within the first step of the analysis. The result of the Adaptive PIV is one vector map per image pair. The same process for using the "Vector Statistics" function is also applied to obtain a single vector map.

The 2D Least Squares Matching technique is a fundamentally different analysis technique. It is an iterative method which uses cross correlation for initialization, but attempts to capture the effects of fluid element translation, rotation, and deformation[7]. The user interface is also somewhat different. The initial Interrogation region size can be set independently in the X and Y directions. Interrogation region overlap is defined as a "shift" which can also be set independently in the X and Y direction. A "Search Factor" defines the real size of the interrogation region as the initial Interrogation region is matched to that dimension multiplied by the factor you define. The user can also specify the number of iterations the method uses before

it keeps or rejects a vector. If the solution fails to converge before the number of maximum iterations is reached, the default setting is to reject that vector. However, those non-converged vectors can be also be kept if the user desires. Like the cross correlation method, a vector map is produced for each image pair and an independent range validation function can be applied to reject outlier vectors. Filtered vector maps are then averaged by the same "Vector Statistics" function which produces a single vector map.

3.3.2   Window Filtering, Validation Methods, and Specified Inputs

As was mentioned in the previous section, each method has a number of options which can be applied in order to manipulate the results of an analysis method. Some of these options include: interrogation region dimensions, range validation, peak ratio validation, Gaussian window functions, and universal outlier detection.

Interrogation region dimensions are somewhat self explanatory. During analysis an image is usually broken up into equally sized square interrogation regions for cross-correlation or the Least Squares method analysis. The exception to this trend being the Adaptive PIV method which adjusts the interrogation region size based on particle density. Two different interrogation region sizes were used, 32x32 pixel and 64x64 pixel. As previously mentioned, the Least Squares method does not apply interrogation regions in the same way, but the least squares method was applied such that a similar spacial resolution to 64x64 pixel cases were used. Attempts were made at increasing the spacial resolution to a 32x32 interrogation region, however the program always crashed during these attempts, so the effort was abandoned.

Range validation is always applied to the Cross Correlation, Adaptive PIV, and Least Squares methods. For all cases, the horizontal component of velocity was limited to values between 365 and 713 m/s. The vertical component of velocity was limited

from -20 m/s to 163 m/s. These boundaries give a 25 percent buffer on the low and high end of expected values based on theory.

Peak ratio validation compares the two highest correlation peaks for a given interrogation region [7]. If the ratio between them is lower than the specified threshold, then the vector is rejected. For the purposes of this research the two peak ratio values used were 1.25 and 1.5 with the higher value being a more stringent criteria.

Gaussian window functions attenuate the signals near the edges of interrogation regions, this limits their contribution to the correlation and therefore biases the results to the center of the interrogation window [12]. The extent by which this filter biases the results is determined by the input K value. A K value of 1.2 was used during data analysis.

Universal outlier detection was pointedly omitted from most analysis because this method uses a 3x3 ,5x5, 7x7, or 9x9 structural element which compares the relative velocities of vectors within that square [7]. Due to the sudden velocity changes experienced by a shock, it was anticipated that this would likely reduce the shock-resolution. However, the Adaptive PIV method mandates the use of this technique to validate its vectors. Table 3 shows the combinations of Analysis methods and method augmentations explored during this research. Note that a large table of case configurations is given in Appendix B. Table 3 is a condensed representation of iterations completed on several cases.

3.3.3 Image Pre-Processing Method through Dantec Image Processing Library

The Dantec DynamicStudio 2015a software package offers a number of image processing tools including options for thresholding, low-pass filters, median filters, high pass filters, and image arithmetic options[7]. Image ensembles with carbon

55

Condensed Table of Analysis Methods and Augmentations				
Analysis Method		Range Validation (m/s)	Analysis Method Augmenations	
Analysis Method Type	Interrogation Region Size (pixels)		Peak Ratio Validation	Gaussian Window Function
Cross Correlation	32x32	365<U<713 -20<V<163	1.25	Not Applied
Cross Correlation	32x32	365<U<713 -20<V<164	1.5	Not Applied
Cross Correlation	32x32	365<U<713 -20<V<165	1.25	k=1.20
Cross Correlation	64x64	365<U<713 -20<V<166	1.25	Not Applied
Adaptive PIV	32x32 to 64x64	365<U<713 -20<V<167	1.25	Not Applied
Least Squares Method	64x64	365<U<713 -20<V<168	Not Applicable	Not Applicable

Table 3. Table of specified inputs to Analysis Methods

dioxide particles often experience bursts of cloud-like imagery. The clouds of carbon dioxide condensate tend to produce non-favorable results when correlation methods are applied, often producing outlandishly small velocities. Figure 36 shows an example of these "clouds" as they sometimes appear in flows seeded with carbon dioxide.

It was discovered that if an image was filtered first by a 3x3 Low Pass Median Filter, then by a 5x5 Low Pass Minimum Filter that the resulting image appears to be only the "cloudy" background of the initial image. Figure 37 shows an example of the image after filtering. When the filtered image is subtracted from the original, the result is an image that largely removes the presence of the cloud. Figure 38 shows an example of this cloud removal technique. This technique was often applied to cases where carbon dioxide imagery was analyzed.

Figure 36.   Clouds of carbon dioxide condensate sometimes seen in flows seeded by carbon dioxide particles

Figure 37. Image after 3x3 Low Pass Median Filter and 5x5 Low Pass Minimum Filter

Figure 38. Image after subtraction of filtered image

3.3.4 Development of a Bright Particle Filter

When collecting particle image data, the ideal particle is one with a small diameter and excellent light scattering properties. However, the experimentalist is often faced with the choice of setting a laser power such that only the largest and presumably brightest particles can be seen at the expense of missing smaller particles, which more accurately track the flow, but do not have a strong signal. Alternatively, the laser power could be set higher which allows dimmer, presumably smaller particles, to be viewed at the risk of overexposing large particles and introducing non-physical image distortions. This reality can lead to a desire for a method to remove overly bright and sometimes overexposed particles. Moving forward under the assumption that bright particles are the largest and worst performing, the author independently developed a bright particle filter as a means to pre-process images before velocimetry analysis.

This filtering technique is built around Matlab 2015a image processing tools. Matlab reads an 8-bit raw image with each pixel ascribed a value between 0 and 255. With

0 indicating a completely black value and 255 indicating a completely white value. The bright particle filter function is written with two user input values, an "ambient black threshold" and a "white threshold". The ambient black value indicates an estimate of the average background signal. This input value was often around 4 to 6 on the scale from 0 to 255. The white threshold indicates the user defined minimum brightness for pixels within particles that should be removed.

Based on these inputs, a new image is formed. Initially every pixel within the new image is set to the ambient black value. In the non-filtered image, the location of every pixel with a value greater than the white threshold is identified. At this point a square structural element, 5x5 pixels, is created and centered on the pixel locations identified. These square structural element positions mark 5x5 pixel blocks that will set equal to 255. From these block locations, the new image has only two values, pure white blocks (255) where particles will be removed, and the ambient black level (4 to 6) for the background. The final step is to subtract the new image from the original image. Since there can be no negative pixel values, any differences greater than zero will be set to zero. Theoretically, the result is a new filtered image where only the particles with pixel values dimmer than white threshold remain, and the ambient background is set completely to zero.

Figure 39 shows a representative example of what the 5x5 bright particle filter can do. Assume that the brighter gray is above the white threshold and the darker gray is not. The image on the left is the original image with three particles. The middle is created based on the white threshold and ambient black threshold. The image on the right is the result after the middle image is subtracted from the left image.
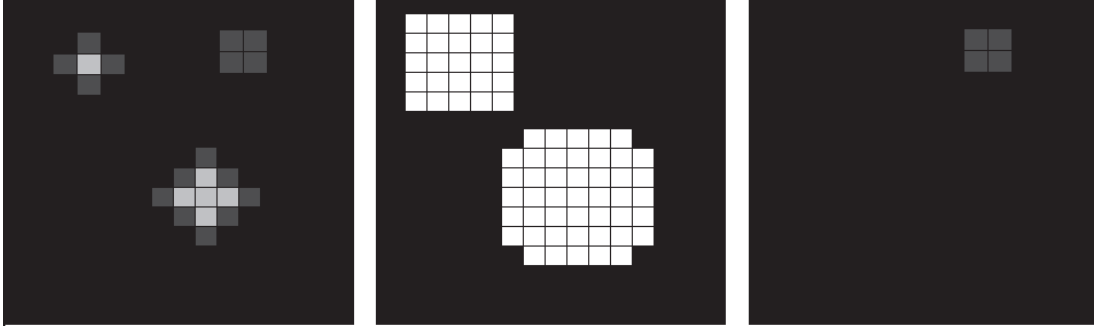
Figure 39. Example of 5x5 Bright Particle Filter functionality. Left image is unfiltered. Middle image is the subtracted from the left image to produce the filtered Right image.

3.4 Data Reduction Techniques

3.4.1 Determination of Average Upstream Flow Angle and Average Freestream Velocity

Due to some variances in the velocities measured between different runs, it became necessary to account for small differences that may have occurred with respect to upstream flow angle and freestream velocity. This section will explain how those quantities are extracted from the data.

The upstream flow angle is a obtained relatively simply from the combination of the horizontal velocity component U, and the vertical velocity component V obtained from PIV data. The equation for the flow angle, α, of a given vector is described below:

$$\alpha = \arctan\left(\frac{V}{U}\right) \tag{38}$$

From that equation, an angle can be obtained from every vector in the region of interest. These results can be plotted on a contour plot like the example plot in Figure 40. It is difficult to ascertain an average from the contour plot, therefore the author chose to plot all flow angles between 0 and 15 degrees on a histogram. An

example histogram is found on in Figure 41.
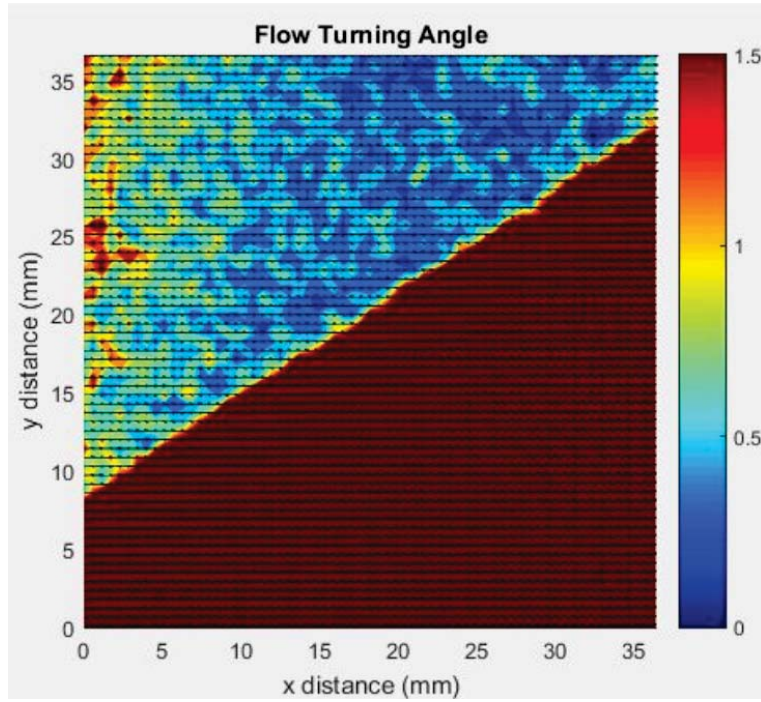
Figure 40.   Example upstream flow angle contour plot
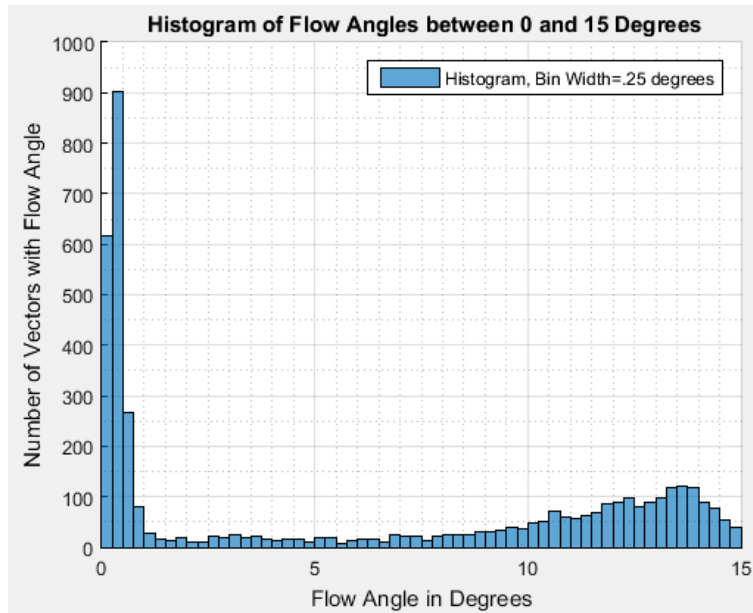
Figure 41.   Example histogram of flow angles between 0 and 15

The first peak within the histogram is representative of the freestream values.

That peak is generally contained within 0 to 1.5 degrees, which is the angle range used for all upstream flow angle determinations. An example of a histogram with this reduced range can be seen in Figure 42.
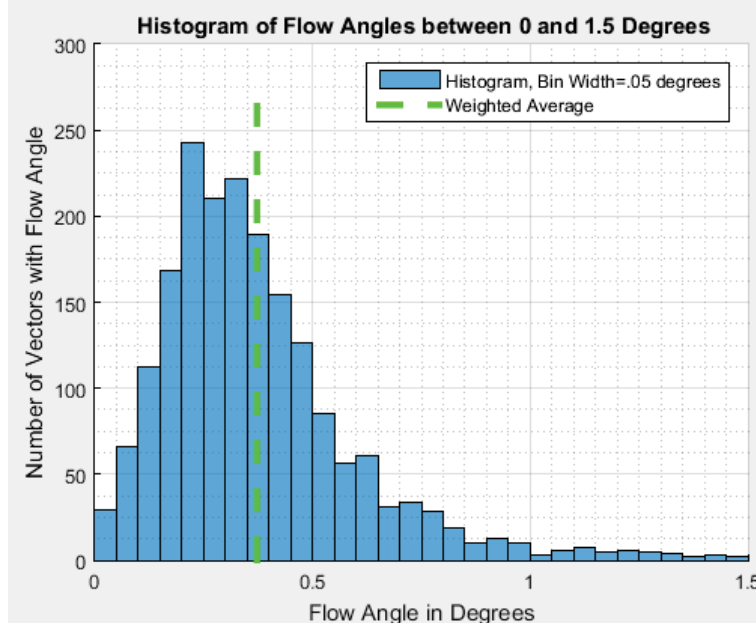
Figure 42. Example histogram of flow angles between 0 and 1.5

Also plotted in figure 42 is a weighted average generated from the matlab histogram output data, a weighted average can be found using the following equation:

$$\bar{X} = \frac{\sum_{i=1}^{N_{bins}} X_i * n_i}{\sum_{i=1}^{N_{bins}} n_i} \qquad (39)$$

where $\bar{X}$ is the weighted average of a given quantity, N_{bins} is the number of bins or columns in the histogram, X_i is the center of bin i, and n_i is the number of data points in bin i.

A very similar process can be used to find the average freestream velocities (discussed in Chapter 4) from the magnitude of the vector lengths. An example of this is shown in Figure 43. Both the upstream flow angle and freestream velocity will be discussed extensively in Chapter 4.
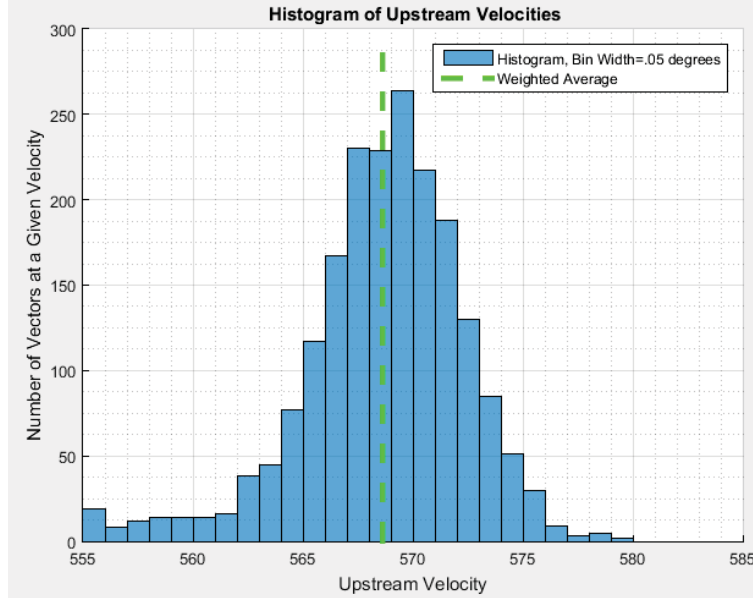
Figure 43.   Example of upstream velocity histogram

3.4.2   Approximation of Mach Number from the θ-β-Mach Relation

The well known θ-β-Mach Relation shown in Equation 25 in Section 2.4 can be used to approximate the Mach number if both the wedge deflection angle θ and the angle of the shock β are known.

The β angle can be determined relatively easily from the reflection of the laser light on the wedge. Figure 44 shows an example of a cropped image from the 105 mm test cases where the wind tunnel is turn off.

Figure 44.   Cropped image of wedge reflection line

Using Matlab image tools, the non-black points can be plotted, and a linear regression can be used to determine the slope of the line. By use of basic trigonometry,
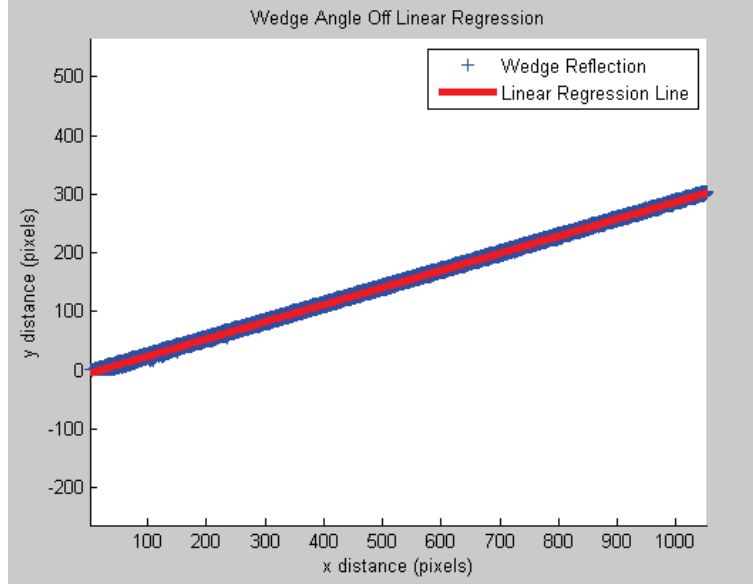
Figure 45. Wedge reflection line linear regression used to determine wedge angle

the wedge angle (relative to the camera) can be determined from the slope of the regression line. Figure 45 shows an example of the regression line determined from the image in Figure 44.

This "tunnel off" angle (nominally 15 degrees) is computed using the same process for each data set. The wedge used for the experiment is actually a half wedge, so it experienced some movement from higher pressure on the top face which caused it to increase its angle (relative to the flow and the camera) by about 0.2 degrees. Therefore, for all cases, 0.2 degrees were added to the "tunnel off" value.

Measurement of the shock angle, β , can be achieved in a manner that is very similar the wedge. Shock waves are often identifiable by a lighting discontinuity in the image, which is very distinct in most cases. This shock wave can be marked with a line using photo editing software. Figure 46 shows an example of an image containing a visible shock wave highlighted through photo editing software.

The right image in Figure 46 can be further cropped and edited such that the only the white line of the where the shock discontinuity appears can be seen. At that
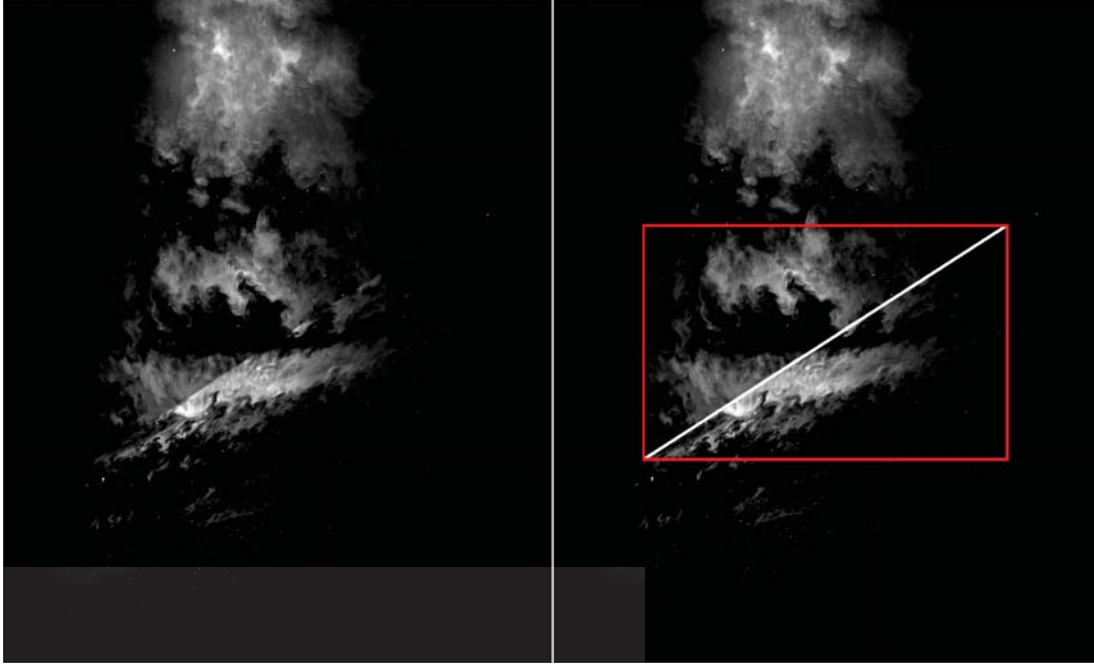
Figure 46. Image containing visible shockwave (Left), Photo edit highlighting shockwave (Right)
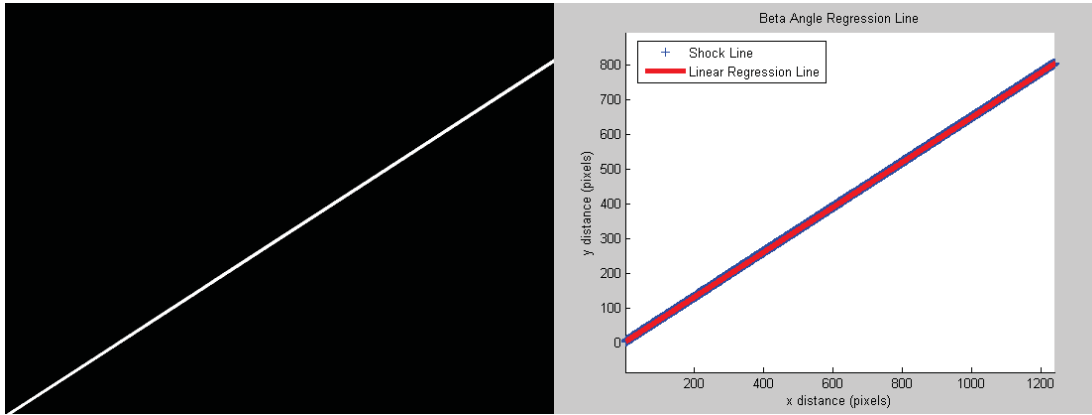
Figure 47. Edited shock angle picture (Left), Corresponding Regression line (Right)

point the same linear regression technique can then be reapplied for the shock angle. Figure 47 shows this process.

The methods for identifying the following quantities have been presented: upstream flow angle α, the wedge angle θ, and the shock angle β. If the camera and the wind tunnel were perfectly aligned, the upstream flow angle should be equal to

zero and the velocity before the shock should be purely horizontal. However, because there is a non-zero average for α, it quite possible that the camera and the wind tunnel are rotationally offset by that very small angle angle. That means that the true β and θ are also offset by an angle α. Thus the equations for the compensated β_c and θ_c angles are the following:

$$\beta_c = \beta_{image} - \alpha_{average} \tag{40}$$

$$\theta_c = \theta_{image} - \alpha_{average} + \theta_{offset} \tag{41}$$

where β_{image} and θ_{image} are values determined from the linear regression methods and θ_{offset} (also determined from linear regression) is the amount that the theta angle increases when the wind tunnel turns on. Note that θ_{offset} was found to be essentially constant and equal to 0.2 degrees for all cases. If the compensated β_c and θ_c are used in the θ-β-Mach Relation, the Mach number of the freestream can be determined analytically. Compressible Flow theory can then be applied to find theoretical freestream velocities that can be compared to the Averaged Freestream Velocities determined by methods in Section 3.4.1. Results of this Mach number analysis and average freestream velocity comparisons will be presented in Chapter 4.

3.4.3 Normal Velocity Contour Plots and Normalized Particle Response

Once a Mach number and β angle have been established for a given data set, the process for producing a normal velocity contour plot is reasonably simple. Recall the following equation mentioned in Chapter 2:

$$V_{norm} = U sin\beta + V sin\beta \tag{42}$$

From this equation, matching U and V vectors can be used in conjunction with β_c to produce a new V_{norm} contour plot resembling the example plot in Figure 48.
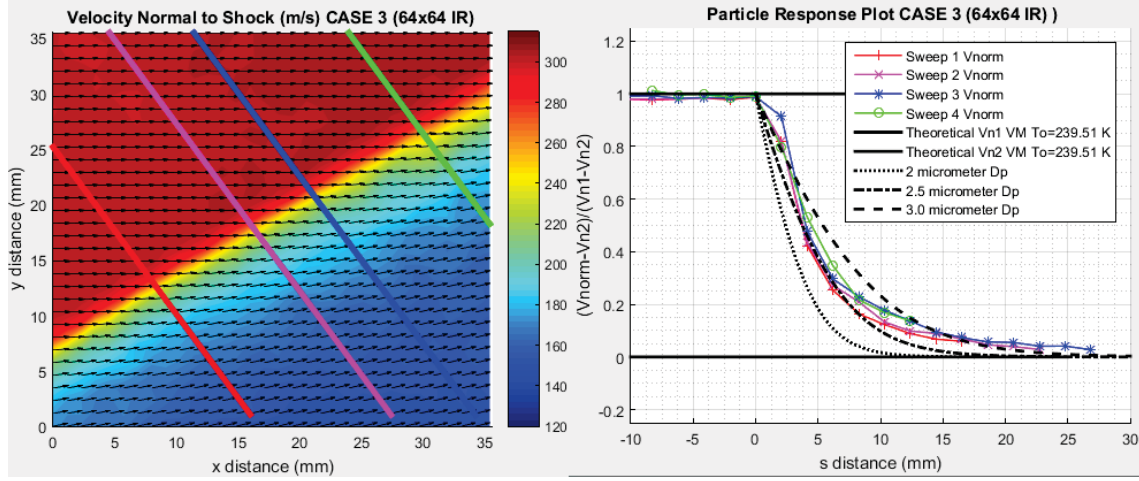
Figure 48.   Example Normal Velocity Contour Plot(Left) and Normalized Particle Response Plot (Right)

Lines of data have been highlighted on the contour plot in Figure 48. These lines of data are perpendicular to the shock. It is noteworthy that because velocimetry data is provided only at discrete data points, Y values are linearly interpolated in order to obtain a value at a measured X coordinate. Figure 49 illustrates this principle.

Lines of data extracted from the velocity contour can then be presented on a normalized particle response plot. An example of normalized particle response plot is given by Figure 48 on the right. The vertical axis displays V_{norm} normalized by $V_{n,1}$ and $V_{n,2}$ which are theoretical velocities before and after the shock. This scales the data from zero to one, were zero corresponds to the theoretical post-shock normal velocity, and one is the pre-shock normal velocity. The normal velocities before and after the shock can be determined from Equations 30 and 31 given that an initial freestream Mach number, M_1, and stagnation temperature, T_0, are known. The
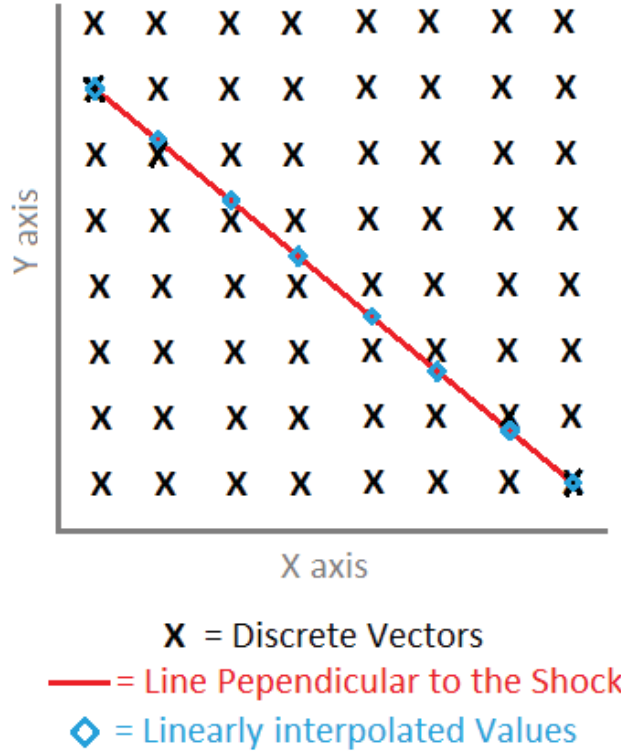
Figure 49. Illustration of linear interpolation in the Y direction

dashed lines represent theoretical response curves assuming a particle density (1.18 g/mm^3 for Carbon Dioxide) and particle diameter (actual particle diameters discussed in Chapter 4). These curves are a result of equation 17 shown in Chapter 2. The horizontal axis is the distance normal to the shock with the zero value marking the location of the shock.

The average upstream velocity is often under-predicted when compared to expected values (determined from Mach number and measured stagnation temperatures) for various analysis methods (explored in chapter 4). For this reason, normal velocities prior to s=0 mm , may sometimes appear significantly below 1 on the particle response plots. In order to correct for this problem in such a way that the response curves can be properly compared to theoretical curves, particle response plots in Chapter 4 are often plotted in terms of a "Velocity Matched Stagnation

Temperatures", T_{0VM} , this is a quantity defined on here the basis of the following equations:

$$a = \frac{V_{average}}{M} = \sqrt{\gamma R \left[\frac{T_{0VM}}{1 + \frac{\gamma-1}{2} M^2} \right]} \tag{43}$$

$$T_{0VM} = \frac{(1 + \frac{\gamma-1}{2} M^2) V_{average}^2}{M^2 \gamma R} \tag{44}$$

Using T_{0VM} values allows for normal velocities upstream of the shock to become closer to 1 on the normalized particle response plots by "matching" the stagnation temperature to a referenced Mach number and average velocity. A rationale for applying such a change in T_0 is that a measurement of T_0 could be biased high. Herein however, its use is simply an expedient way to compare particle lag for different particle introduction schemes whose freestream velocities may not precisely match expected values.

3.4.4   Analysis Method Performance Statistics

In Chapter 4, four primary statistics will be used to quantitatively compare the results of different analysis methods, analysis method augmentations, and image pre-processing techniques. These four quantities include: 1) the percent difference of average freestream velocity from theory predicted values, 2) the average percentage of vectors used in the vector map, 3) the average standard deviation of velocity vectors in the horizontal Direction, and 4) the average standard deviation of velocity vectors in the vertical direction.

As was explained earlier, analysis methods produce one vector map per image pair contained in an ensemble of images that are analyzed within Dantec DynamicStudio 2015a. Those individual vector maps are then filtered via peak ratio validation and

range validation. The non-filtered vectors have components in the horizontal and vertical directions which are then averaged to produce a single vector on a vector map. Component magnitudes of each vector can be exported in a large vector array. Other quantities can also be exported for each vector included in the averaged vector map. Some of these quantities include: the number of vectors used within the average of a specific vector, the standard deviation of the horizontal components of velocity, and the standard deviation of the vertical components. Note that the number of vectors used within the average of a specific vector can be normalized as a percentage of the total number of vectors (rejected and non-rejected, one per image pair).

The technique for obtaining the upstream average velocity was presented in Section 3.4.1. The percent difference in average freestream velocity from theory predicted values can be calculated with the following equation:

$$PercentDifference = \frac{V_{average} - V_{Theory}}{V_{Theory}} * 100 \tag{45}$$

The process for finding weighted averages of the other three metrics (percent of vectors used, horizontal standard deviation, and vertical standard deviation) is similar, but the full range of values for the entire region of interest are utilized, not just the upstream values.

IV. Results

4.1 Results Overview

For the first time, particle image velocimetry was successfully conducted in the M3M6F examining a shock region produced by a 15 degree wedge in Mach 3 flow. Two primary types of seed material were used including solid phase carbon dioxide particles and ambient water particles. Images were captured using a double pulse Nd:YAG laser and a CCD camera arranged in a classical 2D PIV configuration.

The initial premise of this research was to objectively compare the response of carbon dioxide particles using various particle generation methods and then to compare those results to other more traditional particle types. However, the unexpected and uncontrolled presence of moisture in the tunnel during warmer outside temperatures meant that the ability to objectively compare particle types was significantly reduced. Fortunately early results taken with sub-freezing outside temperatures, produced some insight into the behavior of carbon dioxide particles. These early cases imaged with the 60 mm lens are compared to cases containing exclusively ambient water particles (no seed introduced) and also cases with a mix of carbon dioxide and ambient water particles. Table 4. below contains a table displaying seven cases examined.

Note that this data is a subset of a larger body of data, and a full test matrix is included in Appendix A. However, with most of the data being biased by an unquantified mix of ambient water, the author seized the opportunity to closely examine a small number of cases and observe various effects that analysis methods, method augmentations, and image pre-processing techniques can have on both the accuracy of velocity measurements and the resolution of the shock wave via particle response analysis. Thus the seven primary cases are collectively examined within 39

different combinations of analysis methods, analysis method augmentations, and pre-processing techniques. These 39 sub-cases are aimed at isolating the specific effects of each iteration. Appendix B contains a table record the 39 sub-cases examined. A comparison of particle images is also provided for the reader in Appendix D to show the differences between particle images for the all seven cases examined.

Table of Case Test Conditions										
Case	Particle Type	Test Date	Lens Size (mm)	Number of Runs Included	Number of Image Pairs	Laser Power	Upstream Port Configuration	Downstream Port Configuration	To (Kelvin)	Po (psi)
1	CO2	2/5/2016	60	1	109,129	Low	Simple Shroud Tube	Not Used	253	100
2	CO2	2/5/2016	60	2	196	Low	Static Mixing Tube	Not Used	253	100
3	Water	3/3/2016	60	2	266	High	Not Used	Not Used	255	100
4	Water	3/9/2016	60	1	280	Low	Not Used	Not Used	256	100
5	Water	3/11/2016	105	1	181	High	Not Used	Not Used	257	100
6	CO2/Water Mix	3/11/2016	105	3	392	High	Static Mixing Tube	Not Used	252	100
7	CO2/Water Mix	3/11/2016	105	3	406	High	Simple Shroud Tube	Not Used	250	100

Table 4. Table Overview of Cases Examined

4.2   Particle Seeding Trends and Imaging Effects

As can be seen in Table 4, data in Cases 1 and 2 are early test cases featuring carbon dioxide particles. In Cases 3 through 5, no seed was added to the flow and velocimetry was conducted exclusively with ambient water particles. Cases 6 and 7, were seeded with carbon dioxide and a known presence of ambient water particles. These seven Cases were imaged using two different lenses with cases 1 through 4 imaged with a 60 mm lens, and Cases 5 through 7 imaged with a 105 mm lens. It is also noteworthy that Cases 1,2, and 4 are illuminated with a lower laser intensity than Cases 3, 5, 6, and 7. Section 4.2 attempts to track the qualitative and quantitative trends incurred by these variables. Please refer to Appendix D for representative

72

examples of particle images for all seven cases included in this thesis.

4.2.1 Carbon Dioxide Particle Seeding Qualitative Observations

The use of carbon dioxide particles produced a spectrum of images whose quality varied depending on the image. However, some visual trends did emerge within the imagery. Imagery from early Cases 1 and 2, show that flows imaged with carbon dioxide particles can produce image pairs which give favorable results. Figure 50 shows an image pair from Case 2 showing the particles.
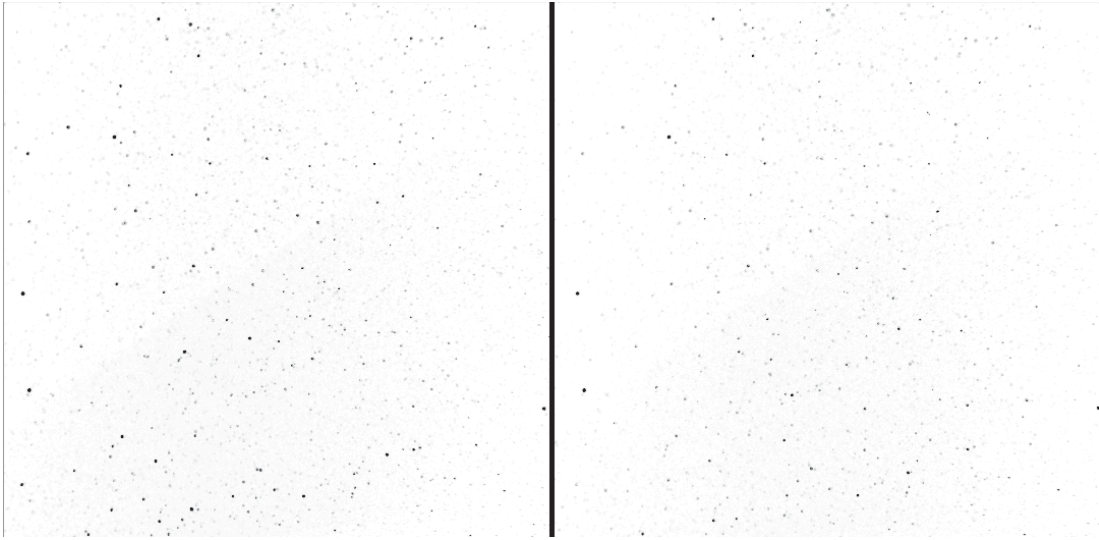
Figure 50. **Image pair from Case 2 presenting a favorable results. Image is inverted from black to white for viewing purposes**

The most obvious factor which distinguished carbon dioxide imagery from imagery captured exclusively with ambient water particles, was the presence of fine condensate resembling "clouds" within in the images. An example of these "clouds" of condensed carbon dioxide can be viewed in the image pair displayed in Figure 51. In many images, the intensity of the scattering also increased downstream of the shock wave.

The "cloudy" sections of the images tend to have pixel values that can be very uniform with a single interrogation region. Thus there is a tendency for low vectors
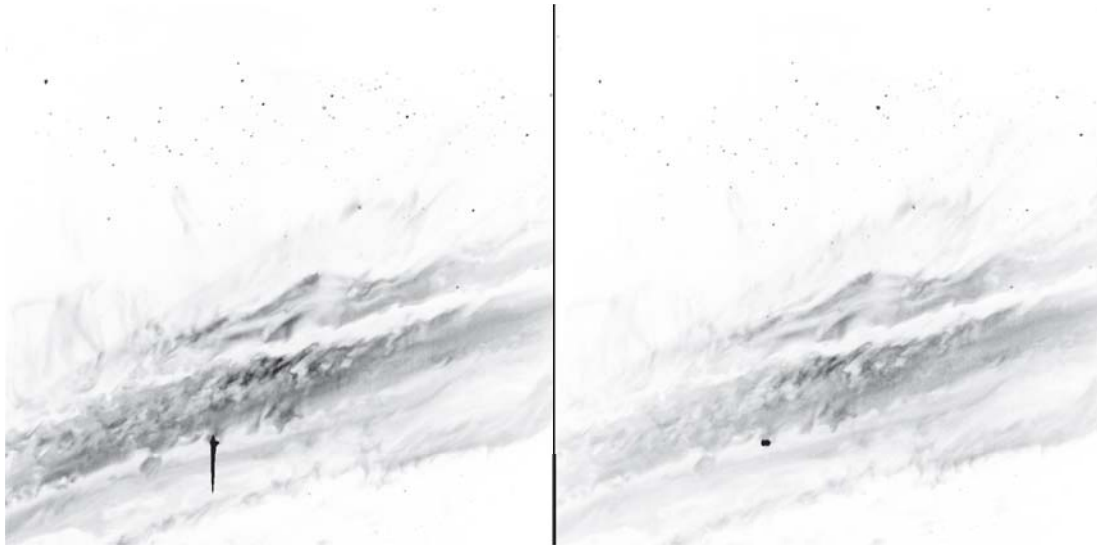
Figure 51. Image pair from Case 1 showing an example of carbon dioxide "clouds". Image is inverted from black to white for view purposes
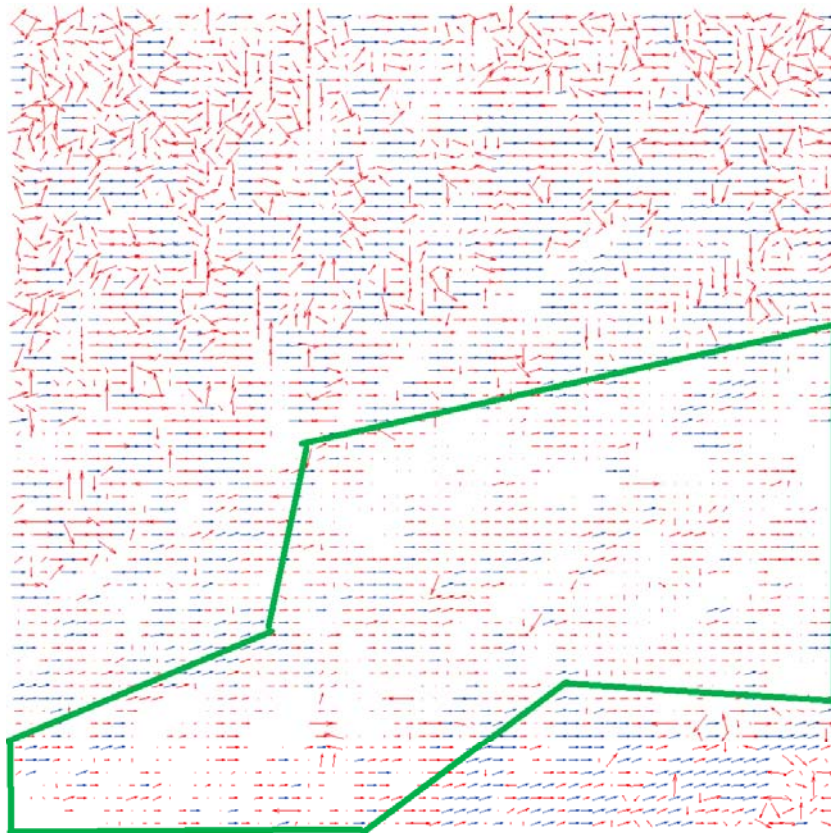
Figure 52. Individual vector map produced from Figure 51 image pair

which tend to be rejected by a range or peak ratio validation. The vector map produced from the image pair in Figure 51 can be viewed in Figure 52. The section highlighted in green encircles this effect. Red vectors are those rejected by validation methods.

Early cases indicated that the static mixing tube produced more favorable images pairs than the simple shroud tube seeding configuration. However, due to the known presence of water particles in later test cases, more tests in a water-free environment are needed to conclude this definitively.

4.2.2   Ambient Water Particle Seeding Qualitative Observations

Ambient water particles are known to have been present in later test cases, namely Cases 3 through 7. These particles were subject to varying densities depending on the test and laser intensity. Figure 53 presents an example of a high particle density image taken with a higher laser power side by side with an image with low particle density and lower laser power. Laser power was set using an attenuator on the unit, specific values for the "high" and "low" setting can be found in Appendix A.
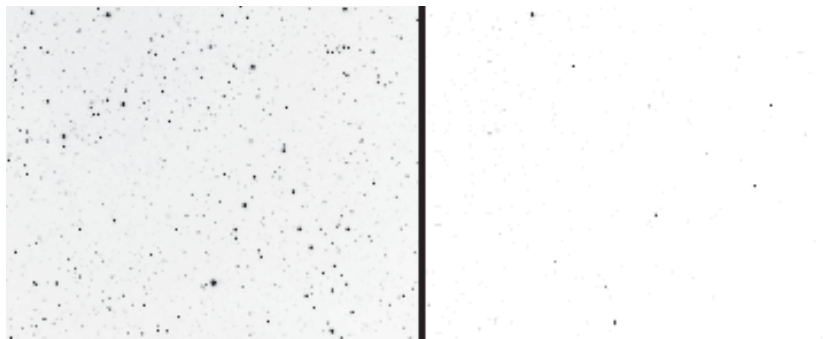
Figure 53.   Image comparing High Density ambient seed from Case 3(Left) and Low Density Ambient Seed Case 4 (Right)

Water particles appear very similar to particles seen in earlier cases, except that there are no clouds present. Some visible lighting distortions happened occasionally

75

around the shock region, but they were not nearly as distinct as the condensate seen while using carbon dioxide seeding.

4.2.3   Laser Intensity Related Imaging Effects

In flows seeded with either carbon dioxide or water (or both), there was a tendency toward overexposing particles at higher laser intensities. These over-exposures led to streaks on the image. This effect can be seen in the image pair included in Figure 54.
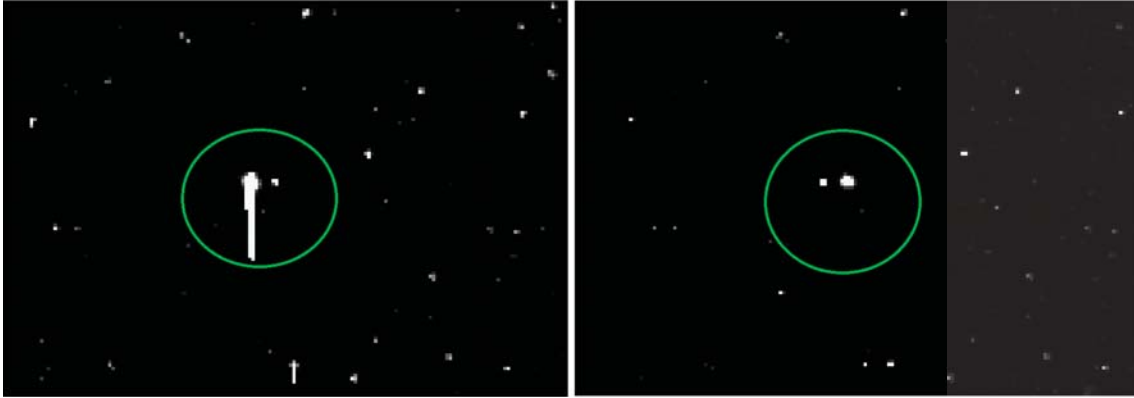
Figure 54.   Case 3 example of over exposed and double imaged particles. Frame 1 is on the Left and Frame 2 is on the right. Double imaging effect circled in green.

In addition, there was often a "double imaging" effect that occurred in places where particles were overexposed. When this effect occurred, a single particle could be seen in both images, appearing almost like two separate particles that do not move from Frame 1 to Frame 2. This effect is also seen in Figure 54. This commonly occurs when particle over-exposure is combined with a small Δt.

4.2.4   Particle Performance Comparison

While the imaging properties of particles observed in the previous sections are important, the true purpose of PIV as a method is to produce vector fields. As explained in chapter 3, averaged velocity may be represented by a vector map. In

this body of research,the averaged velocity field is derived from an array of vectors whose size varies depending on the interrogation region size. For each case, the average is based on a minimum of 109 image pairs with some cases as high as 406 image pairs to produce a single vector map. A welcomed bi-product of this averaging process, is the vector statistics that are also produced as a result. These statistics are given for each point in the vector array, and can also be represented in a contour plot. As a measure of the quality of vector maps produced with different particle generation methods, several accompanying contour plots have been displayed in this section.

Figures 55, 56, and 57 each show 6 contour plots corresponding to Cases 1, 2, and 4. The contour plots included are the following: the horizontal velocity components,the vertical velocity components, the standard deviation of velocity in the horizontal direction,the standard deviation of velocities in the vertical direction, the percentage of total vectors used in the average, and the velocity normal to the shock. Cases 1, 2, and 4 are chosen for particle performance comparison because the image data is captured using the same lens and lower laser intensity, thereby eliminating possible bias due to those factors. As a reminder, Case 1 features carbon dioxide particles generated by a simple shroud tube configuration. Case 2 is also imaged using carbon dioxide particles, but the particles were generated using a static mixing tube. In Case 4, no active seeding was used, and only ambient water particles were imaged. Cases 3, 5, 6, and 7 are shown in Appendix C for reference. All iterations displayed use the cross correlation 64x64 pixel IR, range validation, and a peak ratio validation of 1.25.

Globally, several trends emerge from contour plots in Figures 55, 56, and 57. As expected, freestream velocities prior to the shock wave are relatively uniform, showing the highest variation in Case 1 (simple shroud tube). In the immediate shock region, velocity in the horizontal direction decreases sharply while the vertical direc-

tion begins to increase. Standard deviations in the horizontal and vertical directions are typically the highest around the shock region and the percentage of vectors used in the average tends to decrease significantly. Standard deviations in the vertical direction are generally higher in the entire region downstream of the shock. These trends are not entirely surprising as particle response varies the most immediately following the steep velocity decrease.

It is noteworthy that the vector maps resulting from images in Case 1 are of the lowest quality produced in any of the cases. The high standard deviations and generally erratic measurements of velocity in Case 1 are probably due to two major factors. The first factor is that this data set contains the lowest number of image pairs of all of the cases (129 image pairs). The second and perhaps more significant factor, is that the images themselves contain a larger percentage of carbon dioxide condensate "clouds". Case 2, produced by the static mixing tube, had markedly fewer "cloudy" images which led to much more consistent vector plots. Note that all Cases with Carbon Dioxide seeding are prone to this clouding effect. This can be observed in Appendix D. It is also worth noting, that in most cases, the percentages of vectors used tended to be higher in the middle portions of the the region of interest, and dropped off in leftmost and rightmost portions of the region of interest. This may have been induced by some uneven illumination on the part of the laser sheets between Frame one and Frame two.

A more concise way to visualize and compare the particle response is by using normalized particle response plots. Figure 63 contains six plots. The top row shows carbon dioxide Case 1 with particles generated by the simple shroud tube. The second row shows carbon dioxide Case 2 with particles generated by the static mixer tube. Lastly, the bottom row shows the ambient water particle Case 4. The left plots are normal velocity contour plots, and the plots on the right are particle response plots.

The colored lines through the normal velocity contours show where data was extracted to make the response plots on the right. Note, that for ease of comparison all three sets of theoretical response curves are based on solid carbon dioxide density of 1.18 g/cm^3 and "velocity matched" T_{0VM} values are used (defined in section 3.4.3). Cases 3, 5, 6, and 7 can also be viewed in appendix C.

Using the same analysis methods, it is apparent that early test carbon dioxide particles and ambient water particles have slightly different responses to the shock wave. While all three cases initially follow a theory curve of 1.5 micrometer diameter particles, the carbon dioxide cases experiences an elongated response after about $s = 5mm$. Case 1, with particles produced by the simple shroud tube, does not respond to the full change in velocity within the region of interest. The carbon dioxide particles in Case 2, produced by the static mixing tube, showed an improved response, and could be projected to adjust to the shock induced velocity change within 25 to 30 mm. Lastly, the water particles had the shortest response and followed the flow from about 20 to 25 mm.

These results have some implications for the particles' ability to track flow perturbations within a certain length scale. Recall the Stokes' number presented in Chapter 2:

$$St_k = \frac{\tau_p}{\tau_k} = \frac{\tau_p U_o}{L} \tag{46}$$

where τ_p is given as:

$$\tau_p = \frac{1}{C} = \frac{\rho_p d_p^2}{18\mu} \tag{47}$$

According to literature, a Stokes' number of less than 0.1 is desirable [6]. Under conditions seen in the Mach 3 tunnel, water particles and carbon dioxide particles

79

followed theoretical trends indicating particle diameters of 1.5 to 2.0 micrometers (as seen in Figure 58). Equation 46 can be used to solve for a length scale by which perturbation in a flow will be captured by particle motion with negligible error induced via particle lag. Assuming a particle density of 1.18 g/cm^3, a fluid dynamic viscosity of air equal to $6.92*10^{-6}$ Pa-s , and a particle diameter of 2.0 micrometers, the particle response time, τ_p , is about 38 microseconds and with a characteristic frequency of about 26 kHz.

Following Williams et al.[23], a turbulent velocity is assumed to be 5 percent of a freestream velocity of 570 m/s (nominal condition in Mach 3 tunnel). Therefore assuming a $U_0 = 28.5$ m/s, τ_p equal to 38 microseconds, and a Stokes' number equal to 0.1, carbon dioxide particles should be able to fully capture flow perturbations within a length scale of about 1 centimeter or greater within 1 percent error. Ideally, this length scale would be on the same order of the Kolmogorov scale in order to resolve the smallest turbulent eddies in a flow. It is important to note that perturbations of smaller magnitude will still be captured using carbon dioxide, but subject to error greater than one percent induced by particle lag.
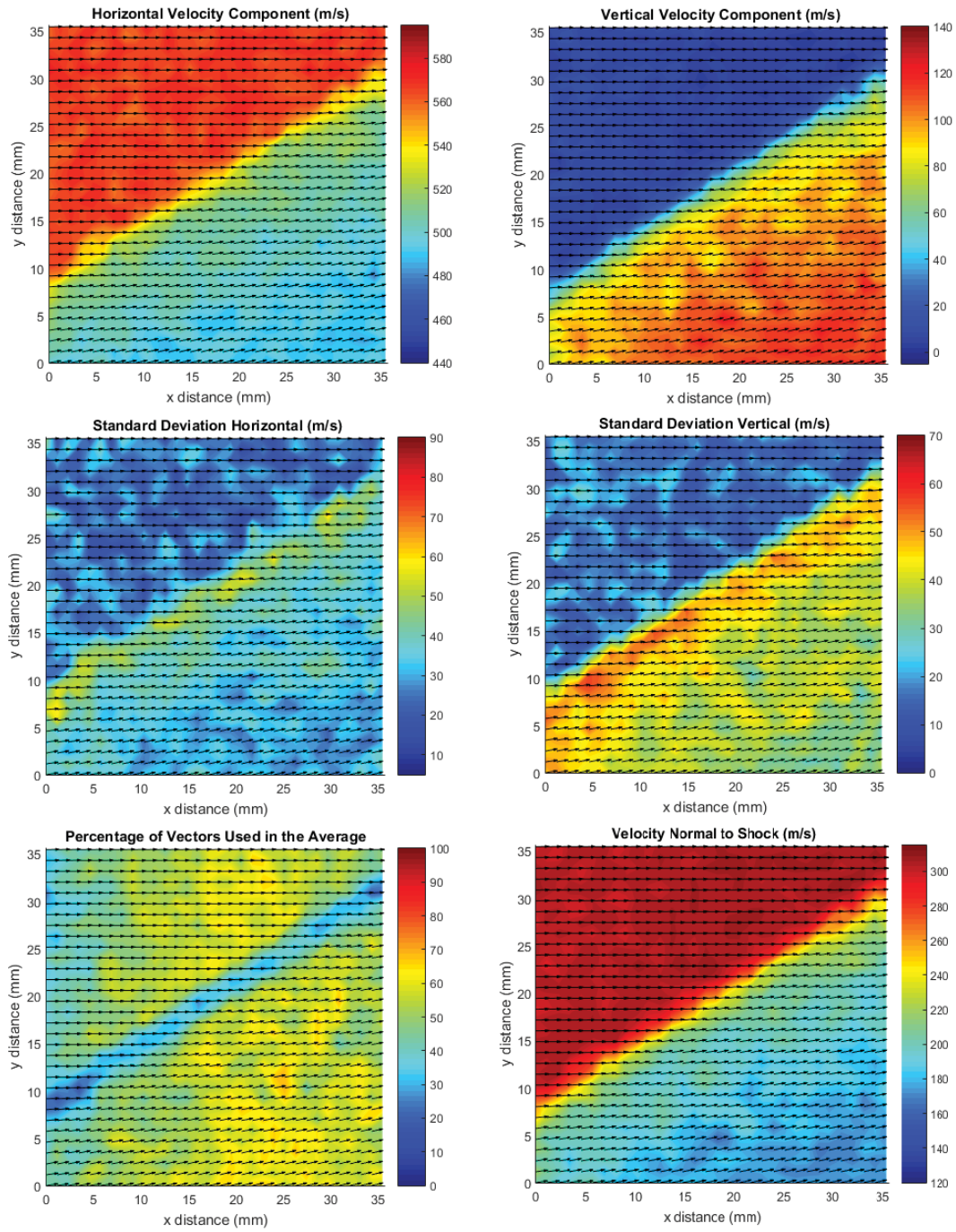
Case 1 Cross Correlation 64x64 IR

Figure 55. Case 1 represented in contour plots of horizontal velocity, vertical Velocity, standard deviation of horizontal and vertical velocity components, percentage of vectors used in the average, and velocity normal to the shock
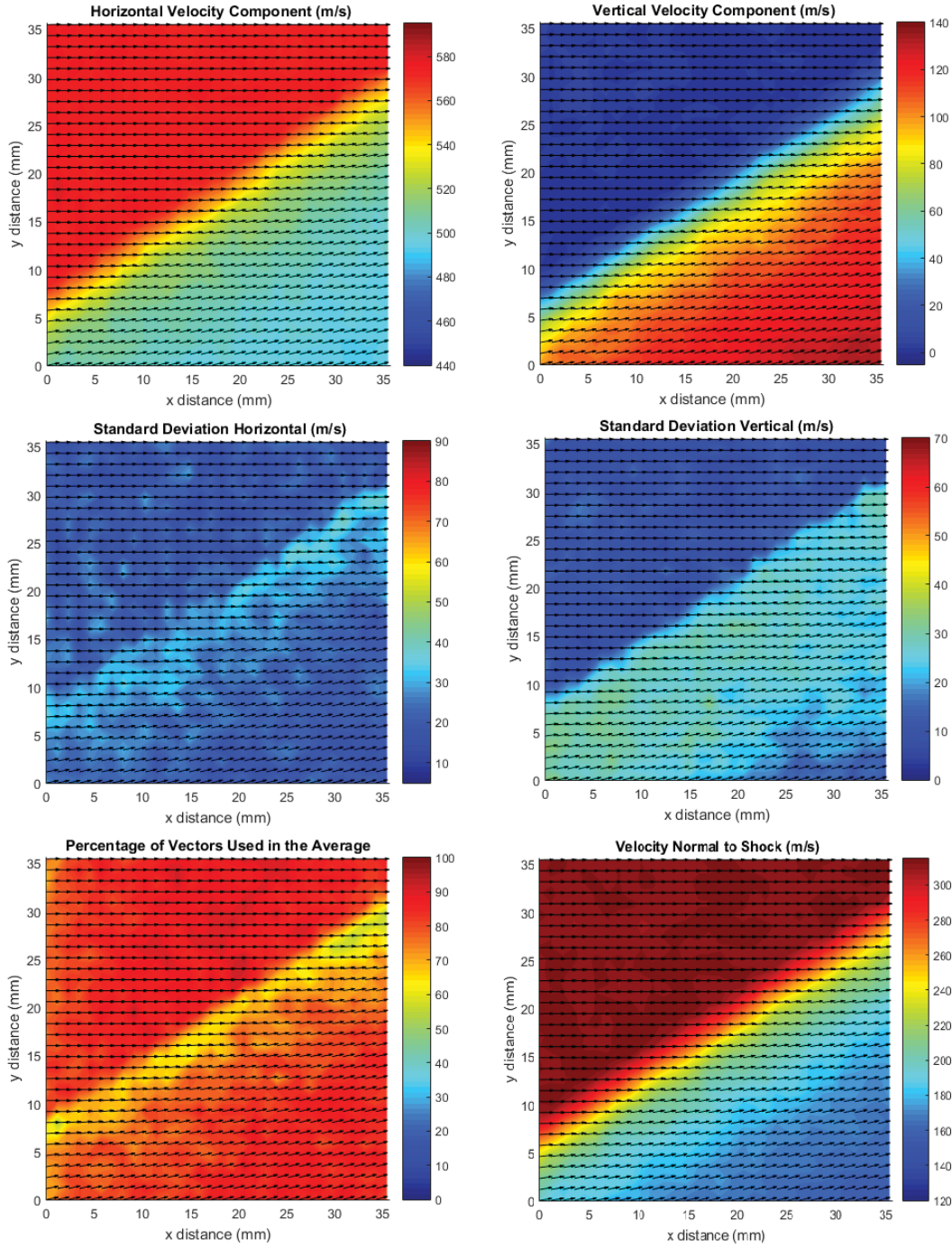
CASE 2 Cross Correlation 64x64 IR

Figure 56. Case 2 represented in contour plots of horizontal velocity, vertical Velocity, standard deviation of horizontal and vertical velocity components, percentage of vectors used in the average, and velocity normal to the shock
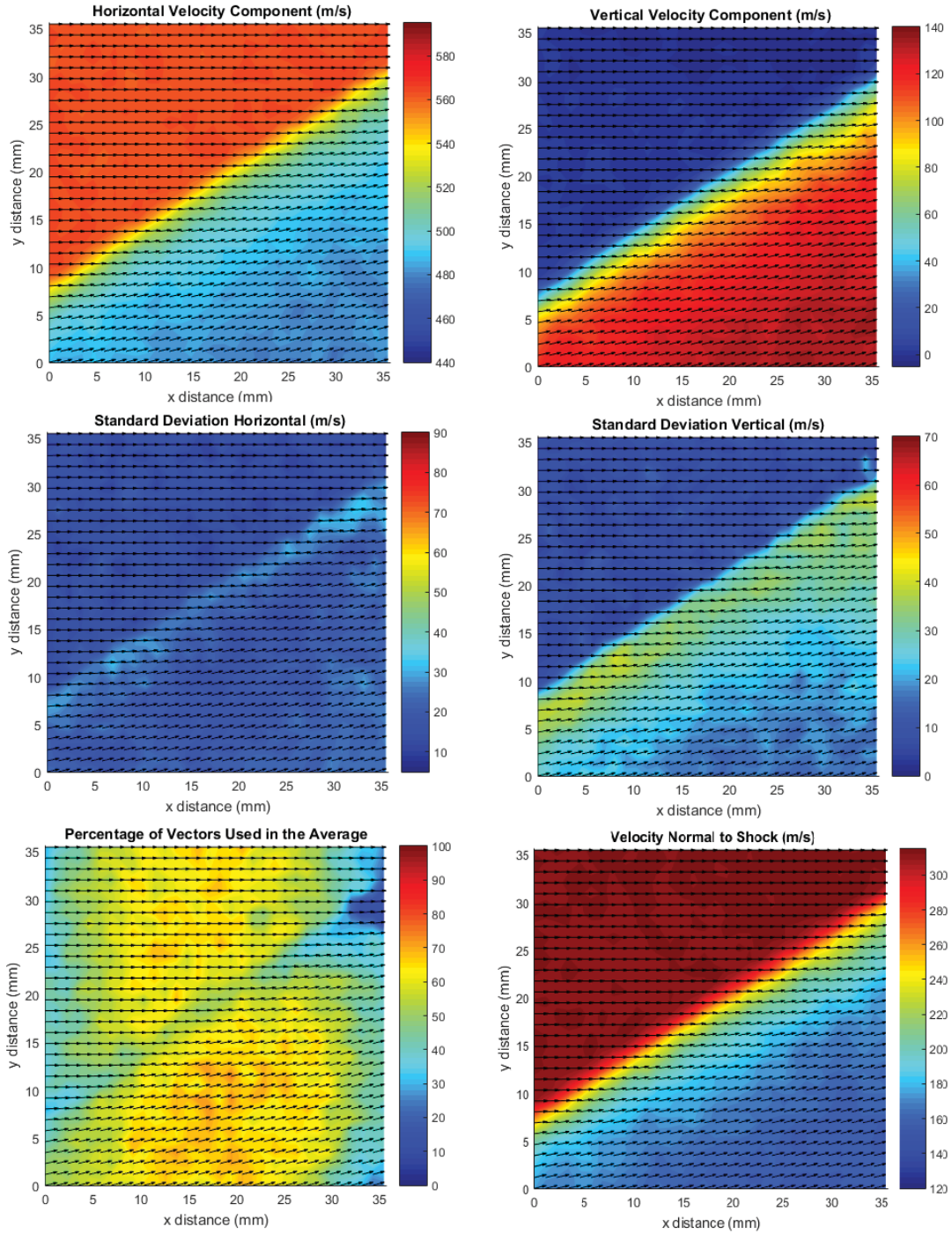
Case 4 Cross Correlation 64x64 IR

Figure 57. Case 4 represented in contour plots of horizontal velocity, vertical Velocity, standard deviation of horizontal and vertical velocity components, percentage of vectors used in the average, and velocity normal to the shock
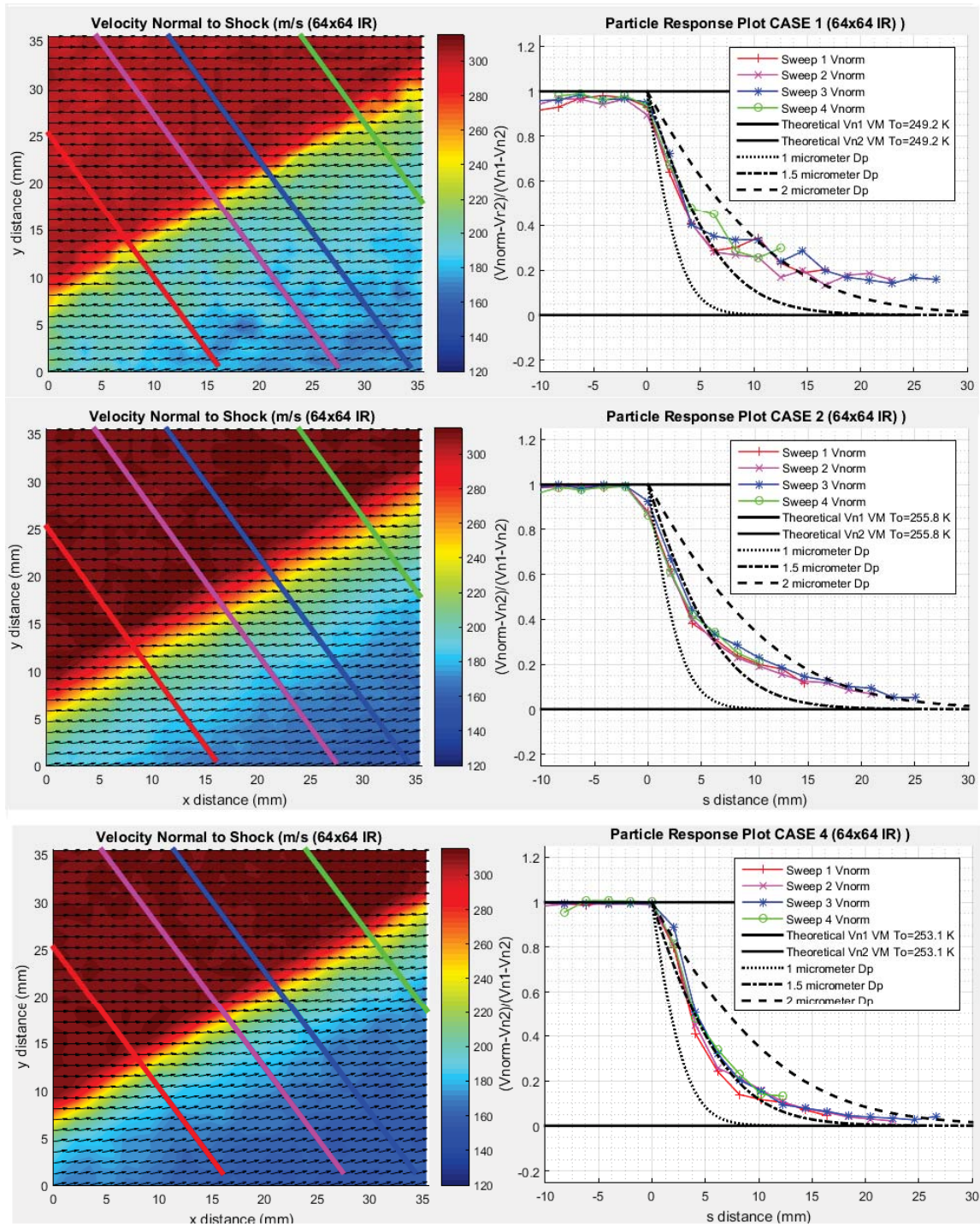
Figure 58. 6 plots comparing Cases 1 (Top Row),2 (Middle Row),and 4 (Bottom Row) in terms of normal velocity contour (Left Column) and particle response plot (Right Column)

4.3   Analysis Method Performance Trends

While the performance properties are ultimately governed by the size and density of the particle, the methods by which velocimetry data is analyzed are also important. This section compares the Cross-Correlation, Adaptive PIV, and Least Squares Methods offered by Dantec DynamicStudio 2015a. These methods can also be augmented with a peak ratio validation filter or a Gaussian window filter. These analysis methods and augmentations are examined in terms of accuracy of velocity measurements in the freestream, the average percentage of vectors used, average standard deviations of velocity in the horizontal and vertical direction, and the particle response across a shock wave.

4.3.1   Mach Number Analysis Results

In order to establish a baseline for the accuracy of velocity measurements, both experimental Mach number and deflection angle , θ, must be known. The nominal Mach number for the wind tunnel is Mach 3 and the nominal deflection angle is 15 degrees. However, the presence of condensation combined with reduced velocity measurements casted some doubt on the accuracy of the nominal value. Thus, some additional effort was invested in determining Mach number based on the β angles and θ angles observed through image data. This process was more thoroughly explained in Section 3.4.2 . The results of this effort are presented in Table 5. This method is limited by the ability of linear regression to resolve the location of the angles of the wedge and the shock wave. The angle determination is limited by the smallest unit of measure within an image, that is, the pixel. The slope of the lines was determined using images that were on the order of 1050x305 pixels for the β angle and 775x515 pixels for the θ angle. These dimensions correspond to the slopes of the lines, where the smaller pixel value is in the vertical direction. Assuming that

the angle determination can be resolved within ± 1 pixel via linear regression, the β and θ angles can be resolved within ± 0.05 degrees. Propagating this potential error into Mach number calculations, this implies that Mach number can be measured within ± 0.02. The Mach Numbers and θ angles presented in Table 5 are the basis of all "expected" velocities seen in subsequent analysis. "Expected" velocities utilize insentropic flow theory, Mach numbers given in Table 5, and measured stagnation temperatures. Equations 40 and 41 were used to compile results in Table 5.

Table of Angle Compensations and Theta-Beta-Mach Predictions								
Case	Particle Type	Image Beta (Degrees)	Image Theta (Degrees)	Upstream Angle (Degrees)	Theta Offset (Degrees)	Compensated Theta (Degrees)	Compensated Beta (Degrees)	Theta Beta Mach Prediction
1	CO2	33.39	16.44	0.81	0.2	15.84	32.58	2.98 ± 0.02
2	CO2	32.9	16.01	0.37	0.2	15.77	32.5	2.99 ± 0.02
3	Water	33.22	15.78	0.21	0.2	15.77	32.67	2.93 ± 0.02
4	Water	33.63	15.73	0.26	0.2	15.68	33.38	2.88 ± 0.02
5	Water	33.6	16.32	0.56	0.2	15.93	33.04	2.92 ± 0.02
6	CO2/Water Mix	34.1	16.36	0.57	0.2	15.96	33.53	2.86 ± 0.02
7	CO2/Water Mix	34.02	16.3	0.63	0.2	15.86	33.39	2.88 ± 0.02

Table 5.   Table of θ_c, β_c and predicted Mach numbers
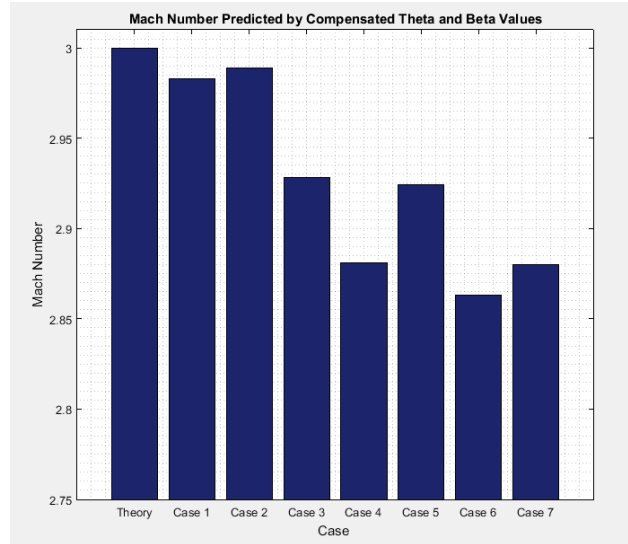
Figure 59.   Bar graph of Mach numbers predicted by θ_c and β_c

A noteworthy result of this analysis was that the Mach number in cases with known ambient water content (cases 3 through 7), indicated a reduced Mach number. Figure 59 is a visual representation of the results.While the variations in Mach number are small, a reduction in Mach number with the presence of condensation is consistent with literature presented in Section 2.5 .

4.3.2   Analysis Method Statistics

In order to quantitatively compare the performance of different analysis methods, several weighted averages, using the techniques described in Chapter 3, were compiled for seven cases examined in 39 different combinations. These results are compiled in Appendix B, but are presented in this section for visual comparison using bar charts. There are four primary statistics that will be analyzed: the percent difference in freestream velocity predicted by compressible flow theory and the weighted average velocity measured by velocimetry (see Equation 45 in Section 3.4.4), the average percentage of vectors used in the vector map produced, the average standard deviation of velocities in the horizontal direction, and the average standard deviation of velocities in the vertical direction.

The first of these four quantities that will be examined, is the accuracy of velocity measurements in the freestream. Each of the seven cases was examined with a minimum of four analysis Methods: 32x32 pixel IR Cross Correlation, 64x64 pixel IR Cross Correlation, Adaptive PIV 32x32 pixel IR to 64x64 pixel IR, and the Least Squares Method (64x64 pixel IR). The weighted averages of the upstream velocities are plotted against the expected velocity values (determined from Mach numbers in Table 5 and measured stagnation temperatures) in Figure 60. These variations in freestream velocity can also be interpreted as a percent difference from the expected values, which is plotted in Figure 61 as an additional visual aid.
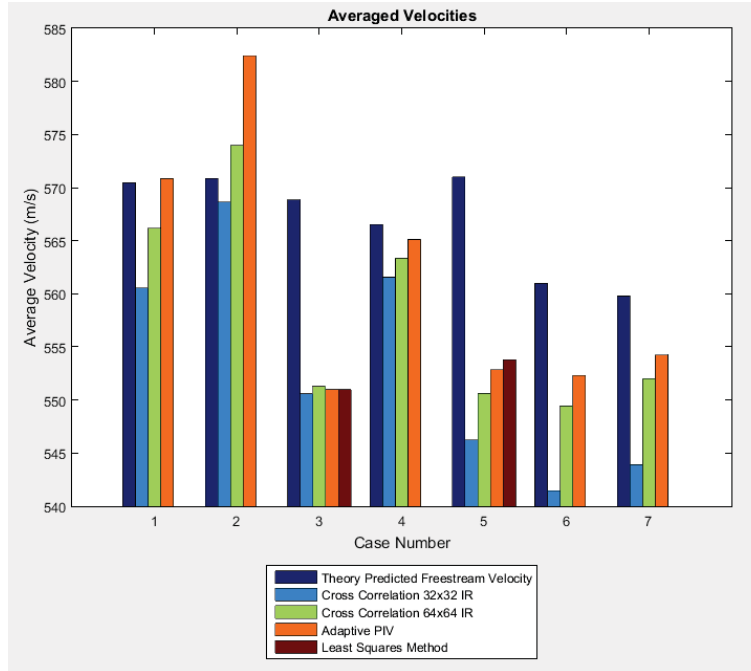
Figure 60. Average Freestream Velocity for 7 cases using 4 different Analysis methods
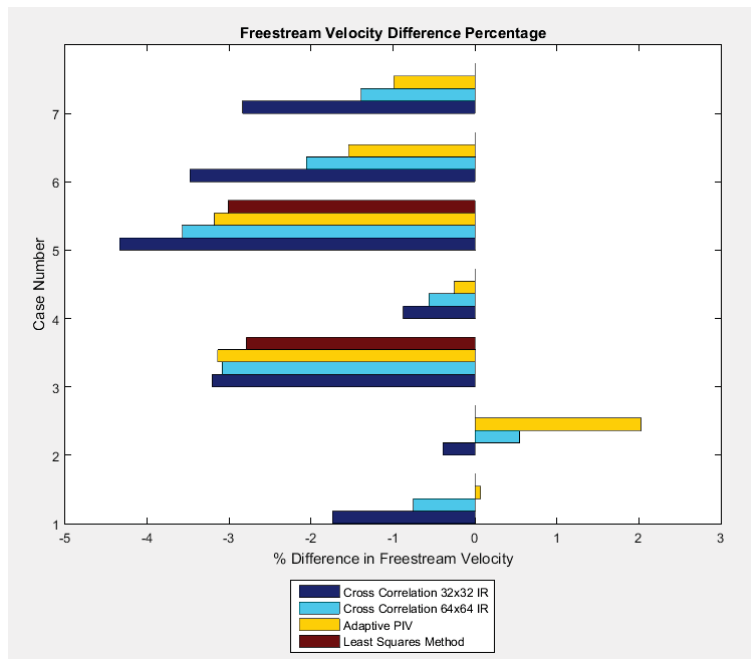
Figure 61. Percent Difference between caculated Average Velocities and Theory predicted Velocities

Close examination of these plots reveal a few trends concerning the 4 analysis methods included. The averaged velocity for all cases was within 5 percent of of the theory predicted values with a few cases within 1 percent.

Cross Correlation with a 32x32 IR consistently under estimated the average velocity in the freestream. This approximation tended to improve by using a larger 64x64 IR, which nearly always underestimated the velocity by a slightly smaller margin.

The Adaptive PIV method typically led to averaged freestream velocity values which were closer to expectations based on isentropic flow. While there was still a tendency to underestimate the velocity, there were two cases where velocity was overestimated.

The Least Squares method only functioned for 2 out of the 7 test cases for which it was attempted. The software simply crashed most test cases. For the two cases that it worked, it was closest to expected velocities by a fraction of a percent.

A noteworthy observation is that the cases closest to expectations in the freestream, namely Cases 1,2, and 4, were all cases with a lower laser power setting. Low laser power results in a tendency for the visual appearance of fewer particles and weaker signal. This tendency also generally meant fewer instances of overexposed particles.

The Mach 3 wind tunnel, which operates in a "blow down" configuration, may be subject to some transient effects due to variations in stagnation temperature. To measure variations in average freestream velocity, an average velocity was obtained utilizing every 40 image pairs (roughly 17 seconds of data, analyzed using 64x64 IR Cross Correlation) in chronological order, for Cases 1 through 7. The study revealed some variation in freestream velocity. Case 2 (Simple Shroud Tube, Carbon Dioxide) and Case 3 are presented in Figure 62.

Cases 2 and 3 show a general decrease in in freestream velocity over time. Cases 2 and 3 both include 2 Runs (subsequent tests within the Mach 3 tunnel, taken on the
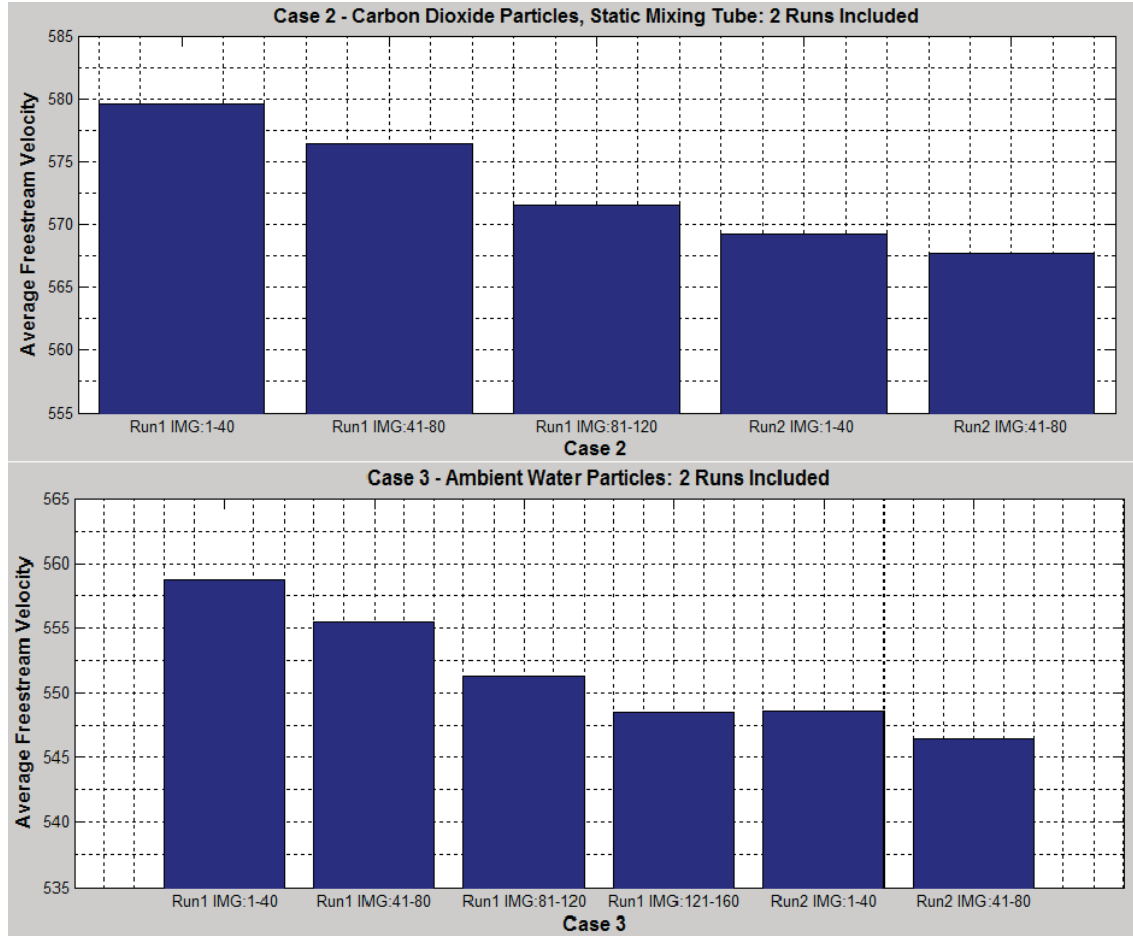
Figure 62. Case 2 (Carbon Dioxide Particles) and Case 3 (Ambient Water Particles), variation of average freestream velocity averaged over every 40 image pairs in chronological order

same day). Case 2 indicates that the average freestream velocity may have shifted as much as 12 m/s (roughly 2 percent) over the course of the two runs used to compile results. Assuming isentropic flow, this could correspond to ± 5 degrees Kelvin stagnation temperature variation over the course of 2 runs. In Case 3, average freestream velocity dropped by a similar margin. It is noteworthy that velocity variations in Cases 2 and 3 were the highest of the 7 cases. Cases 1, 4, 5, 6, and 7 are shown in Appendix E. These cases show variations within 5 m/s (within 1 percent) and did not necessarily show a consistent downward trend in velocity. Velocity fluctuations

90

of this smaller magnitude could correlate to temperature shifts of ± 2 degrees Kelvin over the course of the runs included in the cases.

The next statistic analyzed is the average percentage of vectors used to produce the average vector map generated by an analysis method. The law of large numbers suggests that the more vectors that are included in an average, the more representative that average will be of a theoretical mean [20]. While this idea does not eliminate biases from data collection or analysis method, these statistics did produce some interesting results. Figure 63 displays these results for cases 1 through 7.
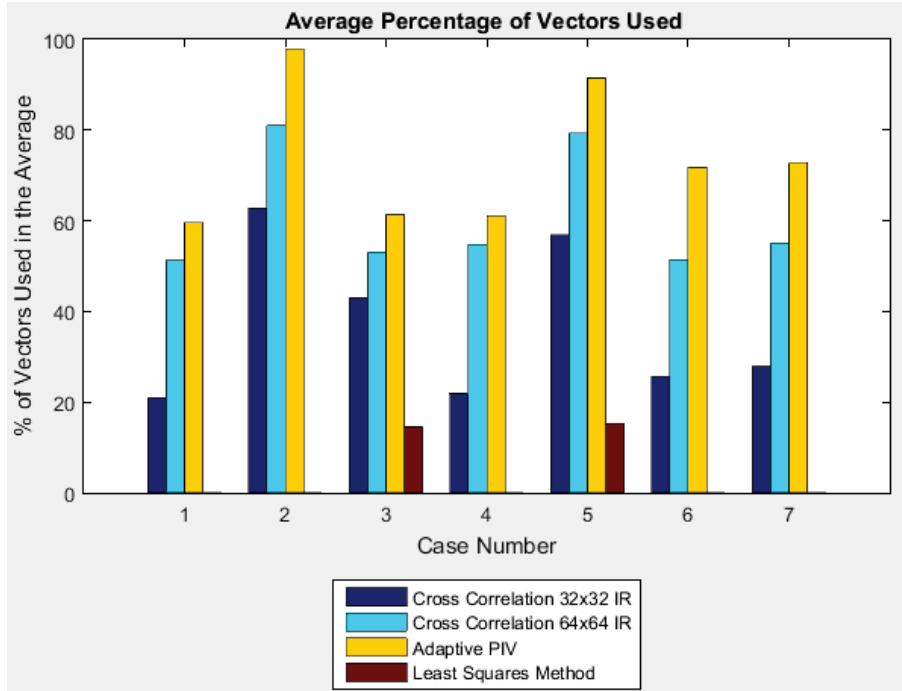
Figure 63. Average percentage of vectors included for Average Vector Maps

There is a very clear trend that emerged with regards to the methods used, and the averaged percentage of vectors used to produce the averaged vector map. In the two cases that the least squares method functioned, less that 20 percent of the total vectors were used in the average. By this metric, the least square method is not ideal. The Cross-Correlation method 32x32 IR performed with somewhat higher values, but

values between 20 and 30 percent occurred in 4 out of the 7 cases. However, doubling the size of the interrogation region, sometimes doubled the percentage of vectors included in the average. Adaptive PIV led to the highest percentages, with 2 cases above 80 percent of vectors used in the average.

The next statistics analyzed are the average standard deviations in the horizontal and vertical directions. Standard deviation is a measure of the variability in the vectors that produced the averaged vector map. Some of this variability is inherent from differences in particle response and flow fluctuations. However, when comparing the average standard deviations from the same data sets, using different analysis methods, it can be a measure of the variability in the interpretation of the data. While the magnitudes of the average standard deviation tended to be lower in the vertical direction , the trends in both directions are very similar. Thus, they are both presented in Figure 64 and will be analyzed simultaneously.

Analysis methods performed with very consistent trends in nearly every case and independently of directional component. The Cross Correlation 32x32 IR method, consistently produced the highest standard deviations in both the horizontal and vertical directions. The only exceptions to this trend were in the cases where the Least squares methods were also included for comparison. In these cases, the Cross Correlation 32x32 IR and the Least Squares methods performed very similarly and both were higher than the Cross Correlation 64x64 IR and Adaptive PIV methods.

The results in this section have provided valuable insight into the performance of the four methods compared for each of the 7 cases examined. The Adaptive PIV method yielded average freestream velocities that were the closest to expected velocity values,the highest percentages of vectors included in averaged vector map, and the lowest standard deviations in vertical and horizontal velocity components. This method adjusts interrogation region size according to changes in particle density
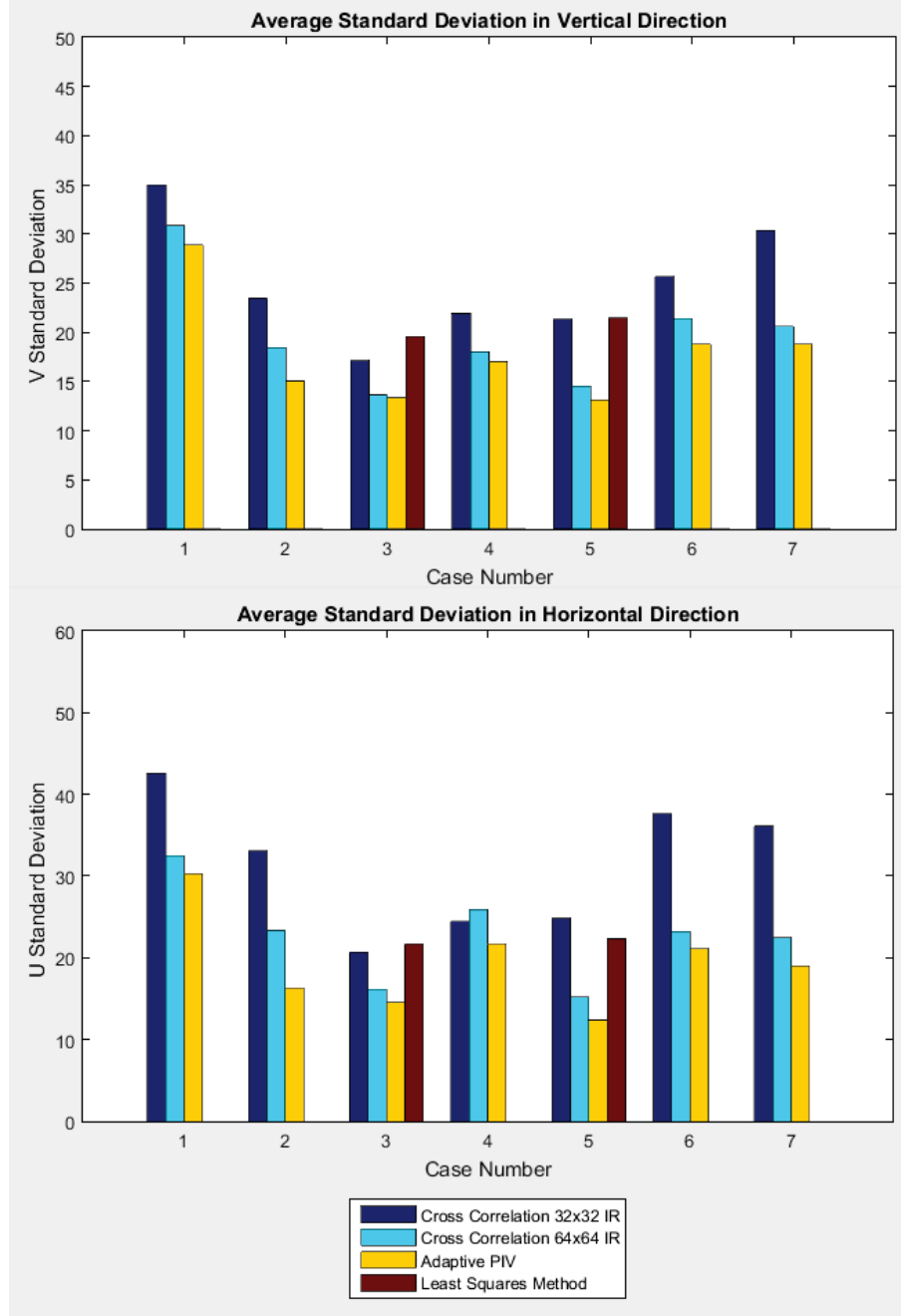
Figure 64. Bar charts of average vertical (Top) and horizontal (Bottom) standard deviations

and velocity gradients [7], which may be the reason for its high performance in these categories. The least squares method only functioned for 2 out of the 7 cases. In the cases for which it performed, average velocity was very slightly closer to expected

values than the other methods. However, a very low percentage of vectors were used to form these averages. The cross correlation 32x32 IR method consistently under predicted freestream velocity by the largest margin (up to 4 percent) , used a lower percentage of vectors in the averaged vector map, and led to the highest standard deviations. The cross correlation method led to freestream velocities slightly closer to expectations when a larger interrogation region was used. The 64x64 IR method also led to increased percentages of vectors used and standard deviations between those in the 32x32 IR and Adaptive Method iterations.

4.3.3 Particle Response for Analysis Methods

While averaged statistics are useful in providing a global picture of the methods performance in a region of interest, a particle response plot can show the differences in how a method resolves a shock wave with the same input image data. In this section the four primary analysis methods will be compared on the same normalized particle response plots. This comparison will feature the two cases for which all four methods were completed, namely Cases 3 and 5 (both using ambient water particles). As shown in the previous section, Cases 3 and 5 have some difference from expected velocities in the freestream. Thus, for ease of comparison, these results are plotted in two ways. The top plot shows theoretical $V_{n,1}$ and $V_{n,2}$ lines using measured T_0 values. The bottom plot shows theoretical $V_{n,1}$ and $V_{n,2}$, using velocity matched stagnation temperatures T_{0VM} (see Equation 44 in Section 3.4.3) which effectively ensures that the freestream velocity values start near 1 on the normalized particle response plots. Case 3 is presented in Figure 65 and Case 5 is presented on Figure 66.

The normalized particle response plots for Cases 3 and 5 reveal that each of the 4 methods generally measure very similar responses across the shock. The exception was the performance of the the Least Squares Method in case 3. The response curve,
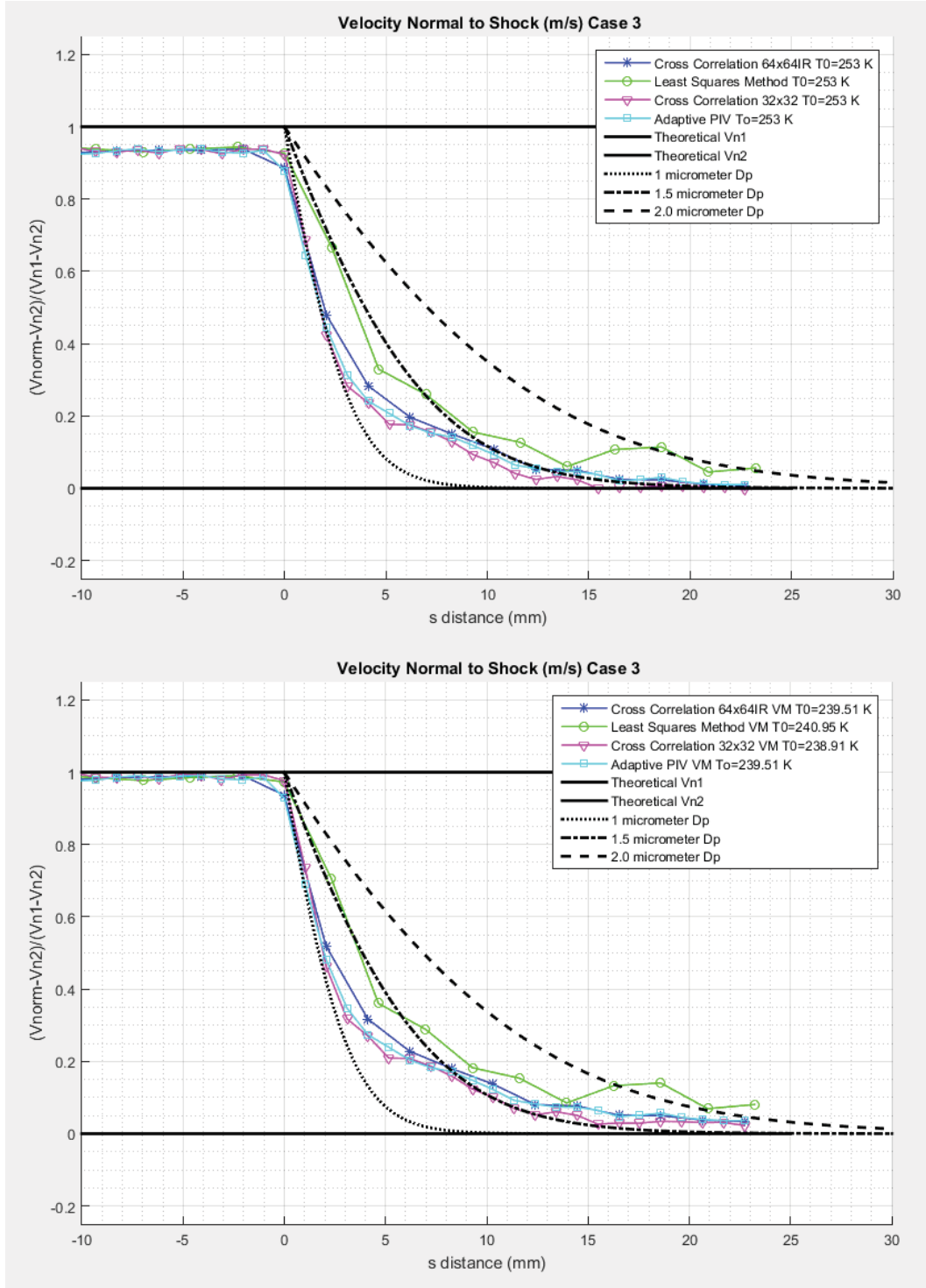
Figure 65. **Case 3 Particle Response plots using 4 Analysis Methods. Top plot uses measured T_0 and bottom plot uses T_{0VM}**
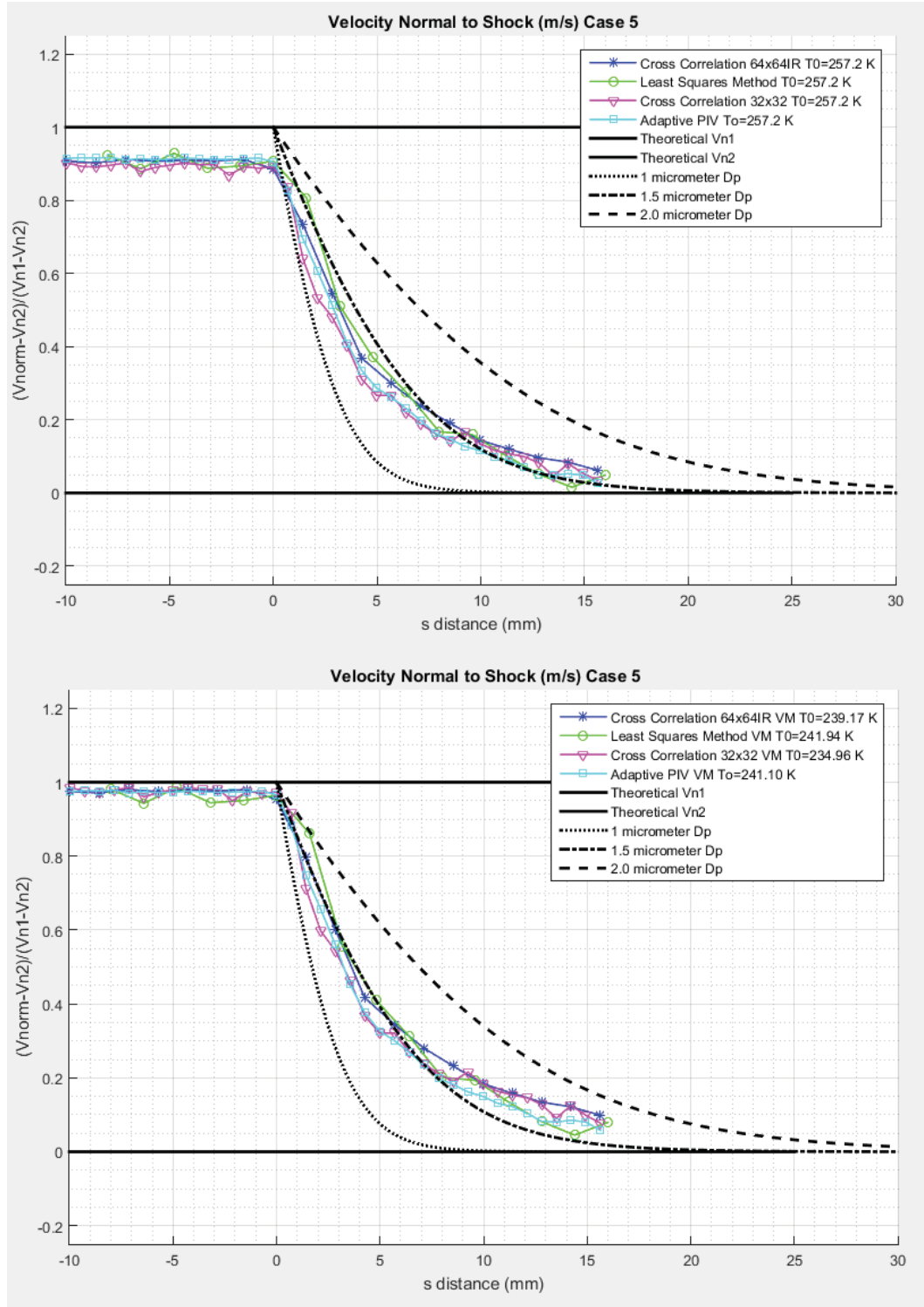
Figure 66. Case 5 Particle Response plots using 4 Analysis Methods. Top plot uses measured T_0 and bottom plot uses T_{0VM}

shown in green in Figure 65, appears somewhat elongated and more erratic than curves produced by the other methods which indicates that the model may be less accurate in this region than its more traditional counterparts. The Cross Correlation 64x64IR and Adaptive PIV methods both feature very smooth particle response curves. However, the Adaptive PIV method has the added benefit of containing twice as many data points. The Cross Correlation 32x32 IR method's performance was less smooth than the Adaptive PIV method, but produced a very similar trend with an initial reduction in velocity that was better resolved than its counterparts.

It is noteworthy that both of these cases were captured using no active seeding techniques (exclusively ambient water particles). The principle difference between these cases was the lens that captured the images. A close comparison of the T_{0VM} response plots (bottom plots) reveals that Case 5 appears to have an elongated response. It is possible that ambient moisture levels were different on runs taken during different days. However, it may also be that particles imaged with different magnifications, lead to different indicated particle response rates.

4.3.4   Effects of Peak Ratio Validation and Gaussian Window Filters

With the exception of the Least Squares method, the analysis methods examined in previous sections can be augmented by the use of peak ratio validation and Gaussian window filters. This section will examine the effects of these augmentations by use of the same averaged statistics and particle response plots used to evaluate the primary analysis methods in previous sections.

The first augmentation examined is peak ratio validation. This filter compares the two highest correlation peaks produced by a correlation method and measures the ratio between them. Ideally, a higher peak ratio indicates a better vector measurement. In Figure 67, statistics from Cases 2 and 3 compare a peak ratio of 1.25

and 1.5. Figure 68, shows the particle response of Case 2 which also compares the two peak ratio values.
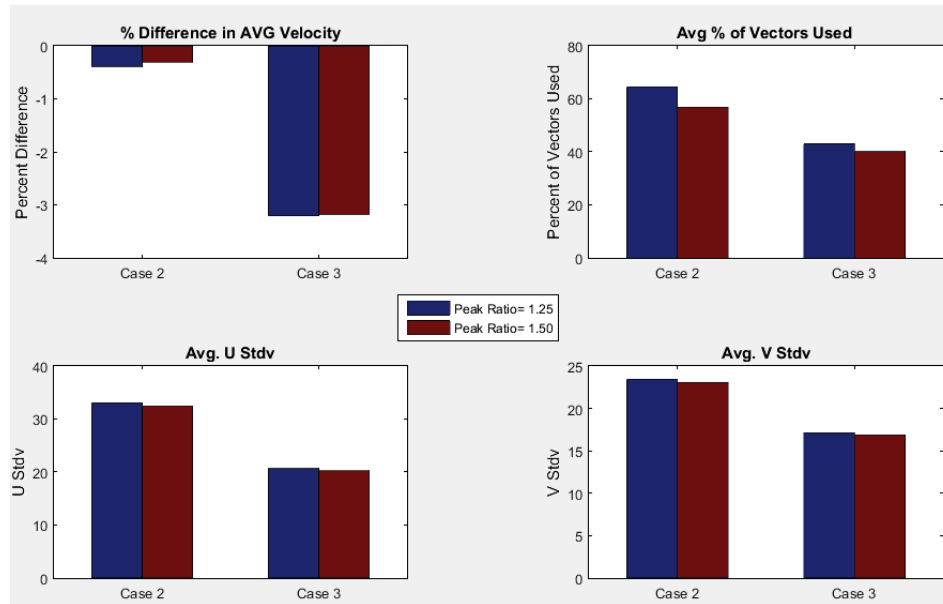
Figure 67. Statistics for Case 2 and Case 3 for peak ratios of 1.25 and 1.5
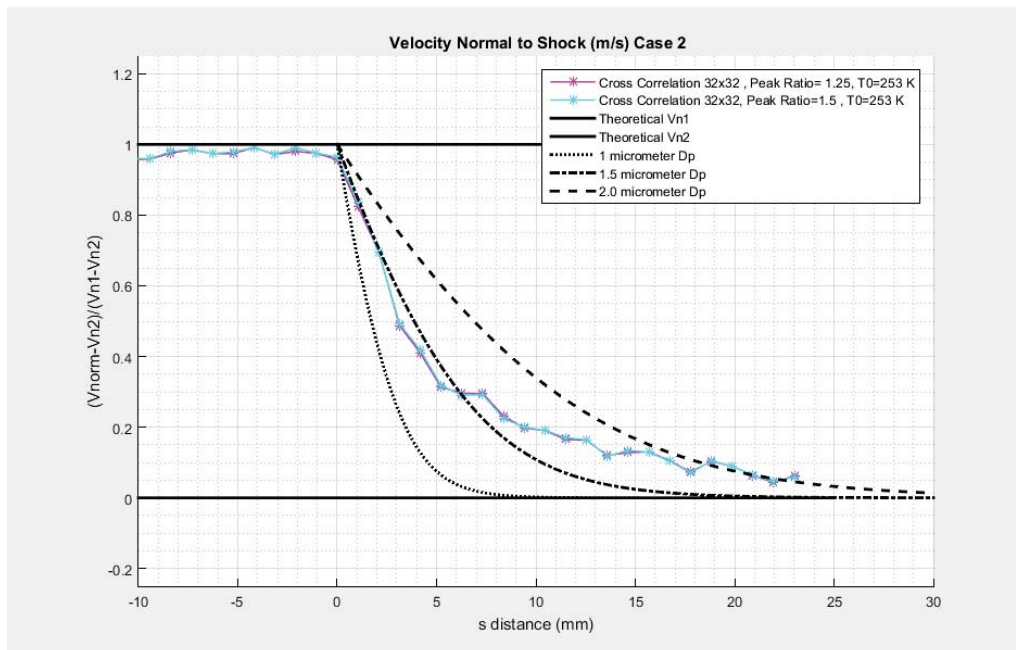
Figure 68. Particle Response plot for one region in Case 2 comparing response curves with peak ratios of 1.25 and 1.5

As can be seen in Figure 67, varying peak ratio between 1.25 and 1.5 had very minimal effects on the the accuracy in the freestream, the percentage of vectors used in the average, and the standard deviations in the horizontal or vertical directions. The greatest effect observed was a slight decrease in the percentage of vectors used in the average. Examining Figure 68, the particle response curves are nearly identical with very small discrepancies between the two peak ratio iterations.

The next augmentation examined is the use of a Gaussian Window function. This augmentation biases the vectors produced by an interrogation region to the window defined by a k value. This is done in the hopes of avoiding error incurred by particles that may exit an interrogation region during the time between frames.
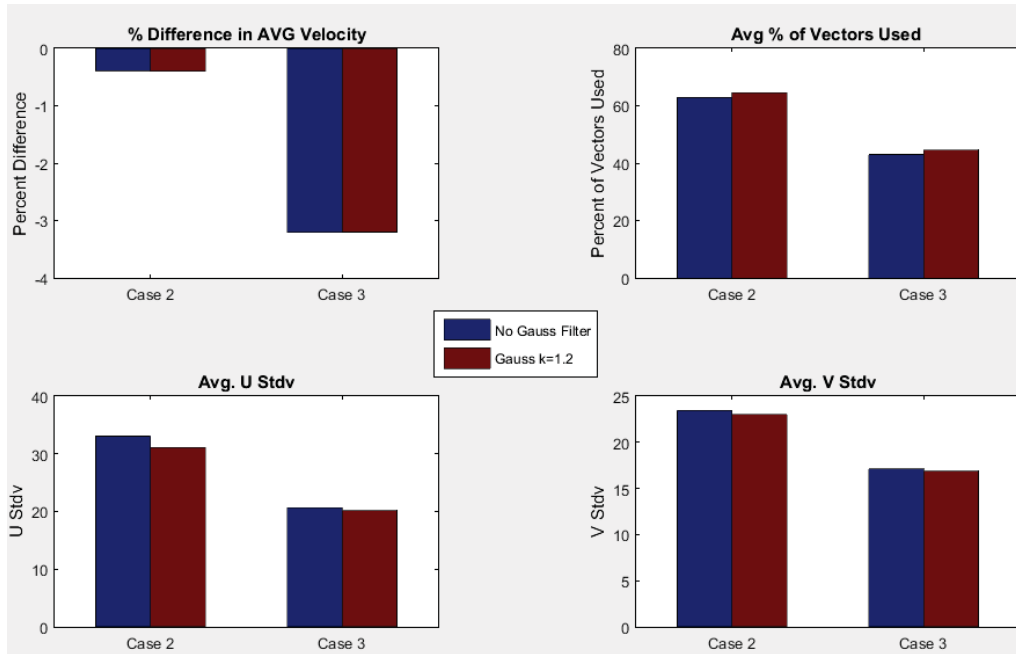
Figure 69. Statistics for Case 2 and Case 3 for with and without the use of a Gaussian Filter

Figure 69 compares the statistics from Cases 2 and 3 using no Gaussian filter and a Gaussian filter with a k=1.2. Figure 70, shows the particle response plot for case 2 comparing iterations with and without the use of a Gaussian filter.
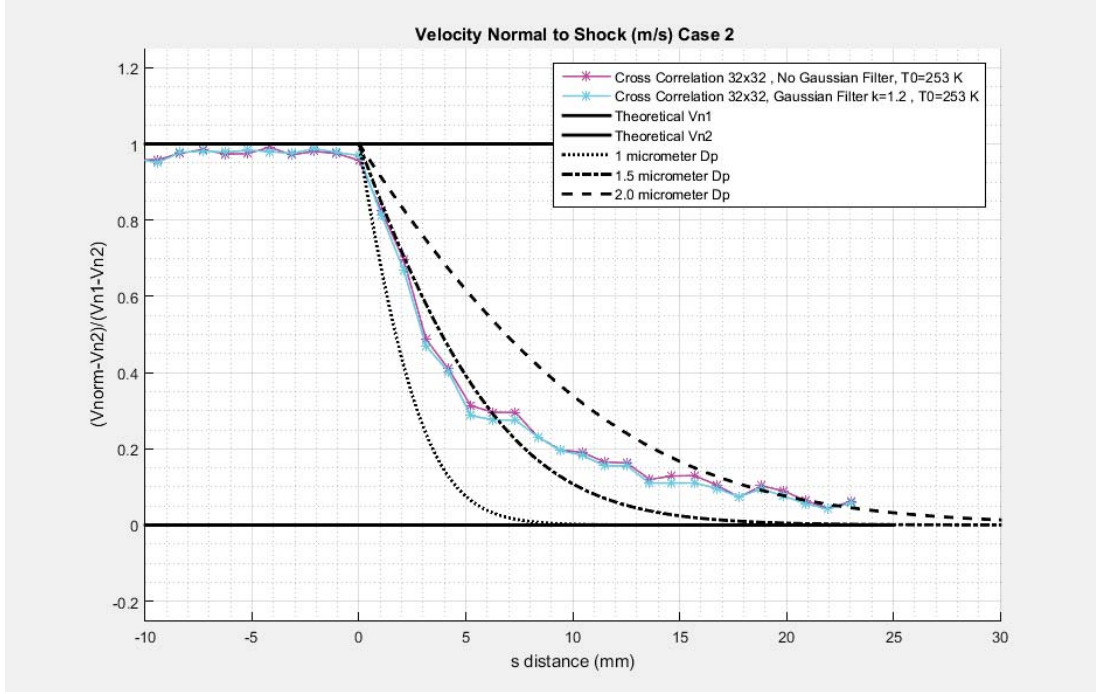
Figure 70. **Particle Response plot for Case 2 comparing response curves with and without the use of a Gaussian Filter**

Similar to the peak validation results, the use of a Gaussian filter with k=1.2 seems to have very minimal effects on averaged statistics. The particle response plot also does not reveal a significant difference in the response of an iteration with a Gaussian filter and an iteration without a Gaussian filter. However, the response curves do seem to indicate a very slight decrease in the normal velocities in the shock region for the filtered case.

4.4 Image Pre-Processing Trends

The previous section focused on analysis methods that take images as inputs, but do not alter the images themselves. This research also explored methods of pre-processing images using two techniques. The first technique was background noise and "cloud" removal which made use of tools included in Dantec DynamicStudio

2015a. The second technique was a Novel Bright Particle filter developed by the author which attempted to remove the influence of brighter particles in the image data. A more detailed explanation of these techniques was provided in Chapter 3. This section provides qualitative and quantitative descriptions of effects produced by these techniques.

4.4.1 Effects of Image Processing using Dantec Image Processing Library

A combination of filters from the Dantec Image Processing Library, namely a 3x3 low pass median filter and a 5x5 minimum filter, were used to produce a "background" image, which was then subtracted from the original image, to produce a new image with reduced background noise. This process is explained with more detail in Section 3.3.3. This technique was originally conceived by attempting to remove the "cloudy" behavior seen in images where carbon dioxide particles are used. The visual results of its application to an image with carbon dioxide "clouds" can be seen in Figure 71.
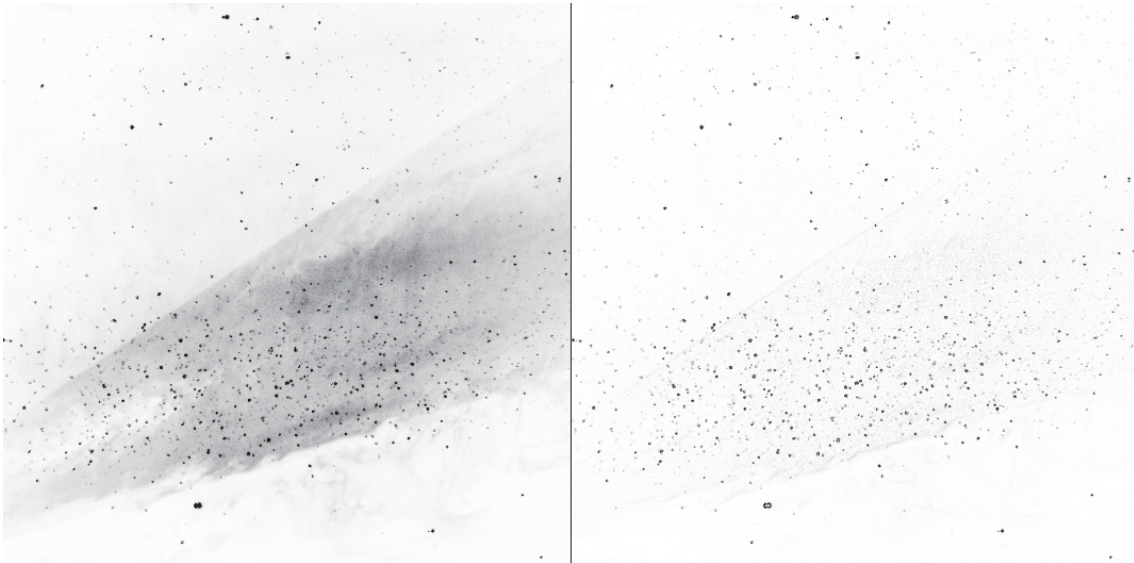
Figure 71. **Image from Case 1 showing the effects of Dantec Filtering on Carbon Dioxide "Cloud". This image is inverted from black to white for visualization purposes.**

Figure 71 reveals that the cloud is visibly reduced, while preserving the presence of brighter particles within the clouds. While the primary objective of this technique was to remove clouds, it could be more applied more generally an any image with background noise. Figure 72 shows the effect that the image filter has on a lighting discontinuity following a shock wave. The unfiltered image features a clearly defined shock wave and the second image shows a more uniform background without the presence of a lighting discontinuity.
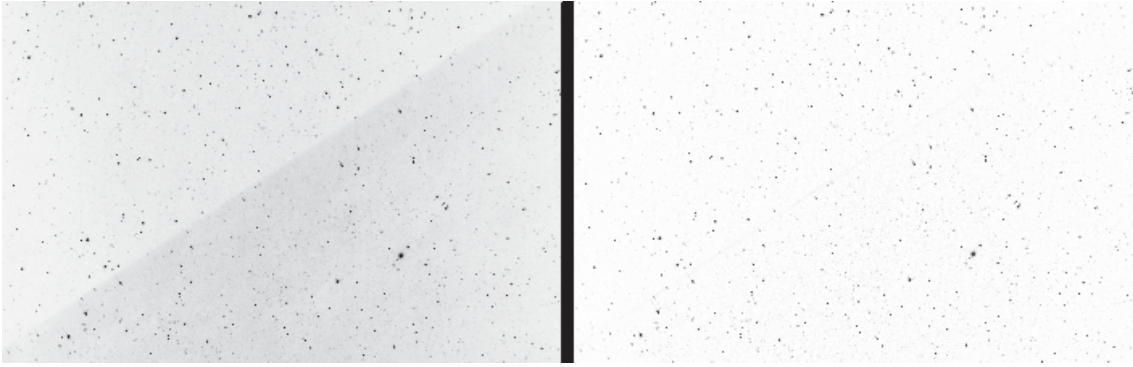
Figure 72. Image from Case 3 showing the effects of Dantec Filtering on shock lighting discontinuity. This image is inverted from black to white for visualization purposes .

The visual success of this technique begs the question of whether or not removing background noise in this manner actually improves the performance of the velocimetry data. To answer this question, Cases 1, 2, and 3 were examined using the same performance metrics used previously. Figure 73 compares performance statistics of Dantec filtered and non filtered iterations of Cases 1, 2, and 3.

Before the results are discussed, it is worth noting that Case 1 was seeded with carbon dioxide particles and had the greatest number of images where clouds were included. Case 2 also featured carbon dioxide particles, but the presence of clouds was less prevalent. Case 3 was seeded using only ambient water particles and experienced occasional lighting discontinuities along the shock. Thus, it is not surprising that the most dramatic effects were observed in Case 1. In Case 1, the difference in average
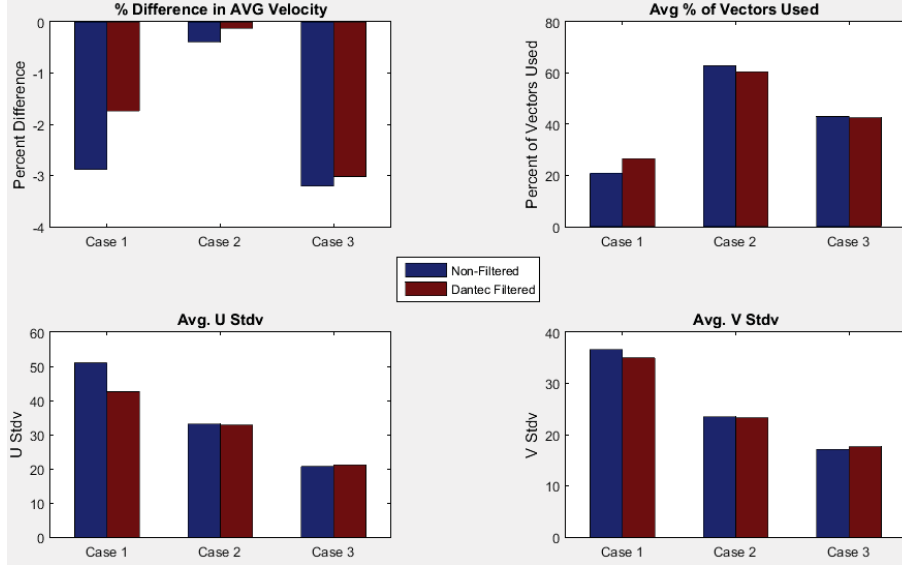
Figure 73. Comparison of performance statistics for Dantec Filtered and unfiltered iterations of cases 1,2, and 3

velocity from theory predictions dropped by over 1 percent. The average number of vectors included also increased and both the horizontal and vertical standard deviations decreased. Cases 2 and 3 were less notable, and were generally unaffected by the inclusion of the Dantec filtering technique.

To understand the effects that this filter has on particle response, Figure 74 compares the particle response plot of an unfiltered iteration and a filtered iteration. Case 1 was selected for examination due to the more significant effects observed in performance statistics. Note that this plot uses Velocity Matched Stagnation Temperatures T_{0VM} for ease of comparison.

The velocity data provided in Case 1 is the most uneven of all seven cases presented in this thesis, but it's imperfection allowed it to reveal the somewhat significant effects of this Dantec filtering technique. While similar peaks and inconsistencies are observed in both response curves, the filtered curve shows a somewhat faster response than the unfiltered case. Thus, in terms of both particle response and performance statistics, a noticeable improvement has been made to results of than ideal image

103
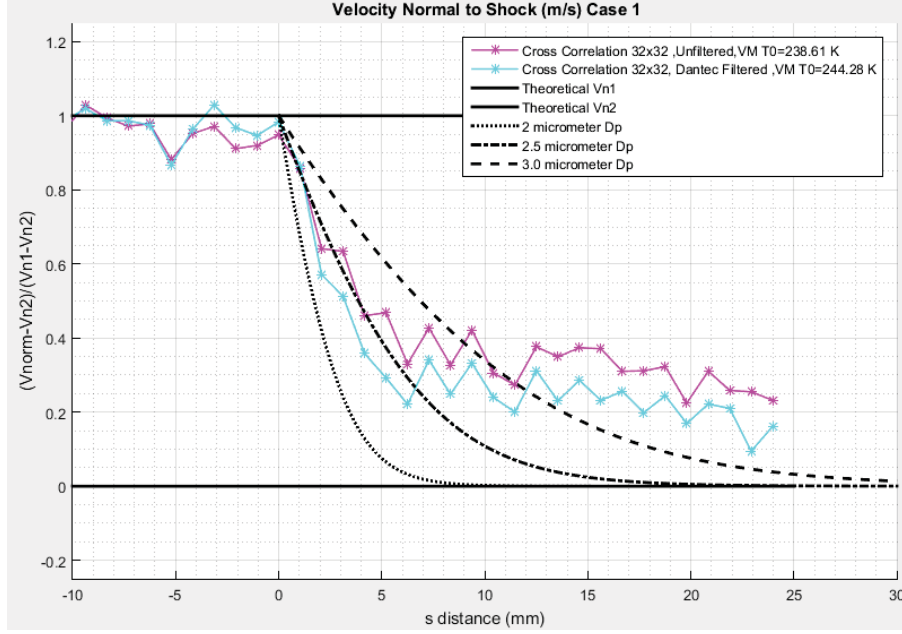
Figure 74. Particle responses of Case 1 using Dantec filtered and non-filtered iterations data.

4.4.2   Effects of a Novel Bright Particle Filter

A novel Bright Particle Filter was developed with the intention of eliminating signal contribution of brighter particles within PIV image data. The idea was that if the brightest and presumably largest particles could be removed from the images, then the remaining dimmer and presumably smaller particles would produce a faster particle response. An additional effect could be the removal of overexposed and double imaged particles that may have ill effects on cross correlation methods. For more specifics on the development and features of the bright particle filter please refer to section 3.3.4. In this section, the effects of the Bright Particle Filter are evaluated by metrics presented in previous sections. The visual effects of the particle filter (on Case 3) are shown in Figure 75 .

To the naked eye, it appears that overexposed particles and brighter particles were
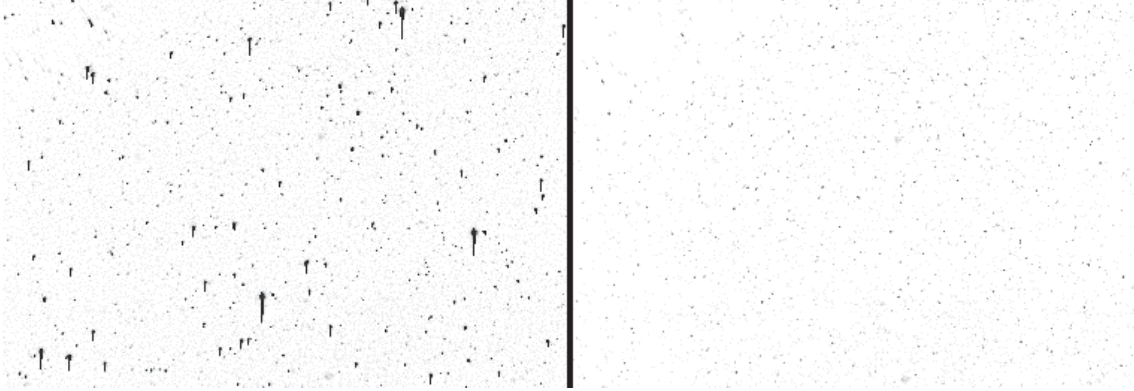
Figure 75. **Images comparing an unfiltered image from Case 3 (left) and an image filtered with the Bright Particle Filter (Right). This image is inverted black to white for visualization purposes**

largely removed from the image and dimmer particles remain. However, the true effects of this filter cannot be determined visually. The novel bright particle filter was tested using Cases 2 (carbon dioxide), 3 (ambient water), and 6 (carbon dioxide and ambient water). Performance statistics were generated comparing iterations that used the bright particle filter and those that did not. These statistics are presented in Figure 76.

Examining Figure 76, the bright particle filter generally had little impact in the difference in average freestream velocity, but the results in other statistics were generally not favorable for the Bright Particle filter. The average percentage of vectors used was reduced by a non-trivial amount in Cases 2 and 6, with case 2 reduced by almost half. Averaged standard deviation of velocities was consistently higher in both the horizontal and vertical directions for the bright particle filtered iterations.

It is not entirely surprising that the number of valid vectors might decrease and standard deviations may increase when the effective particle density and signal to noise ratio are significantly reduced. While the performance statistics are not favorable, the filter was designed with the idea of reducing the particle response time by eliminating larger particles from the image. Figure 77 compares the particle response
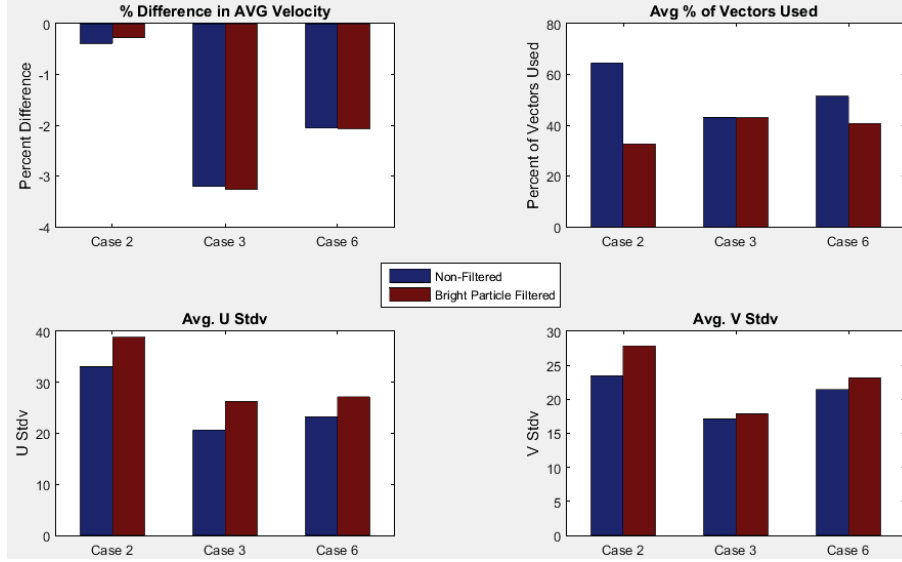
Figure 76. **Comparison of performance statistics for Bright Particle Filtered and unfiltered iterations of Cases 2,3, and 6**

of Bright Particle Filtered iterations with non-filtered iterations in Cases 2 and 6. There is a noteworthy disparity in the number of images included between these two cases. Case 6 contains 406 image pairs compared to case 2 which contains only 196. Thus the results of the particle response comparisons indicate that result may be virtually the same when the number of image pairs is sufficiently high, or the response may be slower and noisier when the number of included image pairs is not as high.

The results of both the vector statistics and the particle response plots indicate that despite a drastic change in the way the particle images appear, this process of filtering out particles with a brighter signal did not lead to a better result.

106
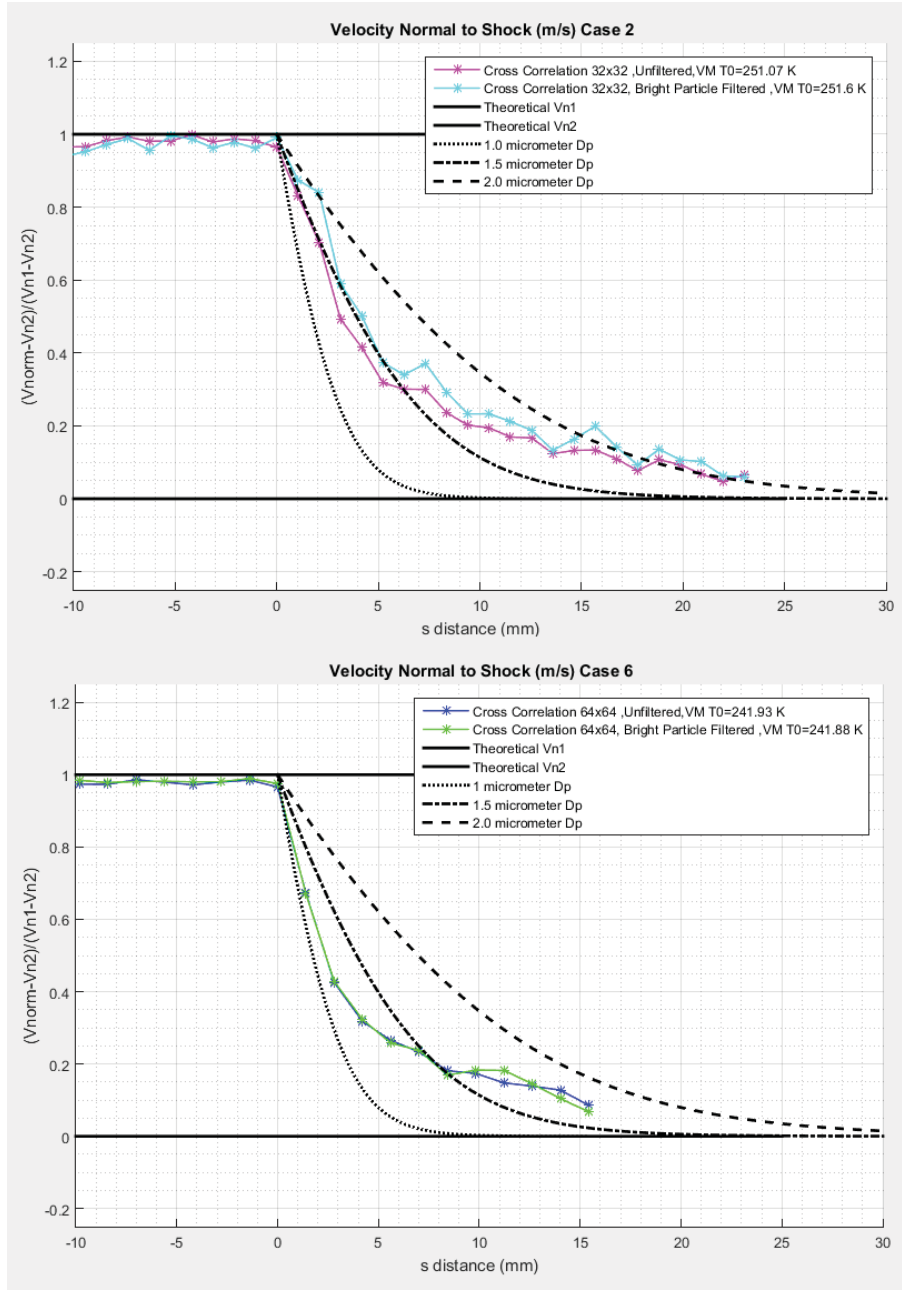
Figure 77. Comparison of response plots for Bright Particle Filtered and unfiltered iterations of Cases 2 and 6

V. Conclusions and Recommendations

5.1 Research Effort Overview

PIV is a robust and useful measurement technique which allows the researcher a glimpse into the full field behavior of a diverse spectrum of fluid flows. While the technique is extremely insightful, it is often hindered by its requirement for idealized tracer particles. Many traditional particles slowly accumulate on wind tunnel surfaces which can affect other tests or the operation of the tunnel itself. The desire to avoid tunnel contamination and its associated maintenance costs precludes the use of PIV in those facilities. This is especially prevalent in closed loop tunnels such as the Tri-sonic Gas Dynamics Facility on Wright Patterson Air Force Base, for which this project was sponsored. Ultimately, the general aversion to tunnel contamination represents a gap in PIV usability which can be corrected given a reliable Clean Seeding alternative.

Motivated by a desire to fill this capability void in both the TGF and in the PIV community, researchers at AFIT, including the author of this thesis, have studied the use of carbon dioxide particles as seed for PIV experiments. This particular work directly tested the performance of carbon dioxide particles by use of well documented particle response experiments. CO_{2s} particles are formed using CO_{2l} stored in large Dewars. This process involves the rapid expansion of CO_{2l} within a simple shroud tube or static mixing tube. Particles agglomerate within the tube and a mixture of CO_{2s} and CO_{2g} enter the settling chamber of a wind tunnel. In this body of work, the Air Force Research Laboratory Mach 3/Mach 6 Facility was used to run particle settling experiments in which a 15 degree wedge was inserted into the Mach 3 flow. The sudden drop in velocity caused by the oblique shock wave provides an insightful measurement of the particle response as described by many other researchers [21, 14, 5, 18, 23].

108

Testing unexpectedly revealed the presence of moisture within the tunnel which allowed the researcher an opportunity to collect velocimetry data without active injection of seed particles. While this particular development offered unique opportunities, it somewhat limited the researchers ability to directly compare carbon dioxide particle generation methods to the intended extent. However, the research was able to compare the response of carbon dioxide particles to that of ambient water particles.

With the option of objectively comparing particle performance based on seeding generation methods partially negated, the body of research refocused on quantifying the direct effects of analysis methods, method augmentations, and image preprocessing techniques. From the data collected, seven cases were selected and evaluated using 39 different analysis configurations aimed at isolating the specific effects of methods such as Cross-Correlation, Adaptive PIV, Least Squares Method, peak ratio validation, Gaussian window functions, and image filtering techniques. The performance of these configurations was objectively compared using averaged statistics of freestream accuracy, percentages of vectors included in the averaged vector map, and standard deviation in the horizontal and vertical direction. Additionally, comparisons were made judging the effects of a configuration on resulting particle response curves.

5.2   Conclusions

Close observation of particle images and velocimetry results revealed several items of importance with regards to the behaviors of carbon dioxide seeding and that of ambient water particles. Carbon dioxide imagery was distinguishable from other imagery by the presence of "clouds" of highly concentrated carbon dioxide which sublimated and then condensed. While this hindered the production of accurate velocity vectors using cross correlation methods, it did provide useful visualization of the shock angle. In terms of particle response, carbon dioxide particles were shown to

109

recover the flow velocity within 25 to 30 millimeters measured normal to the shock. Comparing the response curves to theoretical curves assuming the density of dry ice, this indicated a particle diameter of 1.5 to 2 micrometers and a particle response time, τ_p, of 38 microseconds. Ambient water particles recovered to expected velocities between 20 and 25 millimeters normal to the shock, indicative of particle sizes of about 1.5 micrometers.

Some laser intensity and camera performance related artifacts were encountered during testing that are worthy of note. Laser intensity for some cases was set to a higher setting, in order to produce signal on smaller particles. This lead to a tendency for the overexposure of larger particles. These over exposed particles, sometimes produced a camera generated artifact within the image pair, in which the same particle is imaged in two location on both frames of the image pair.

Close examination of flow angularity , β , and θ values observed in imagery, indicated that cases with ambient water particles present experienced a slight reduction in freestream Mach number. This observation matches theory presented in literature concerning condensation in supersonic nozzles. It should be noted that velocities in cases with ambient water particles, frequently underestimated expected freestream values by 1 to 4 percent depending on the analysis method, even when compared to theoretical isentropic velocities based on the reduced Mach numbers. Average freestream velocity was also shown to vary up to 2 percent during the course of individual tests included in Cases. This variation is likely due to a drifting stagnation temperature.

Comparisons of analysis methods revealed that overall, the Adaptive PIV method was consistently a strong performer in terms of closeness to expected values, average percentage of vectors used, and average standard deviations of velocity in the horizontal and vertical directions. The Adaptive PIV method was also shown to produce

110

smooth curves with high spatial resolution and with trends that were consistent with other methods to which it was compared. Cross Correlation with a 32x32 pixel interrogation region produced similar results with respect to the particle response curve, but typically produced data in which average velocity under predicted the expected freestream velocity (assuming isentropic flow), by the highest margin (up to 4 percent). The percentage of vectors included in the average vector map was also reduced in the Cross Correlation iterations, with values between 20 percent and 65 percent. This range seemed low when compared to Adaptive PIV, which had percentages between 60 and 98 percent. Also in the Cross Correlation 32x32 IR method, standard deviation averages tended to increase by 30 to 100 percent in both the horizontal and vertical directions when compared to the Adaptive PIV method. Increasing the interrogation region size to a 64x64 IR tended to improve the aforementioned statistics and smooth out the results of the particle response curves. However, the reduced spatial resolution made it still somewhat inferior to the adaptive PIV method. Lastly the Least Squares method was also compared using the same metrics. However, it was only successfully applied in two of the seven cases, and generally produced results that were unremarkable and sometimes significantly worse than the correlation methods.

The performance of analysis method augmentations such as peak ratio validation criteria and the use of a Gaussian filter were also examined by the same statistics and particle response curve evaluations. Comparing results filtered by a peak ratio criteria of 1.25 versus 1.5 revealed no significant difference in performance statistics or particle response curves. Likewise, the inclusion of a Gaussian filter with k=1.2 produced similarly non-influential results.

The application of Dantec DynamicStudio's image processing library to filter images containing carbon dioxide condensate "clouds" or shock-centralized lighting dis-

continuities was met with some qualitative and quantitative success when an image produced by low pass median and minimum filters was subtracted to produce an image with reduced background noise. While cases with less significant background disturbances were generally unaffected by the inclusion of this filtering technique, the results on velocimetry data of less ideal quality were more dramatic. In this case, adherence to expected values in the freestream improved by 1 percent, the percentage of vectors included in the average was increased by about 5 percent, and the average standard deviations of velocity components also decreased by up to 20 percent. The particle response curve also indicated a slightly faster response though very similar behaviors were observed.

An attempt to pre-process data in a novel bright particle filter (code developed in Matlab) was also attempted. Under the assumption that the brightest particles are also the biggest and slowest responding particles, a filter was developed using Matlab image processing tools to remove the presence of bright or overexposed particles which contained pixels above certain pixel intensity. Though the visual effect of bright particle removal was dramatic, when evaluated with the aforementioned performance metrics, results were either generally unremarkable or was an obvious detraction. Generally, accuracy in the freestream was unchanged, while the percentage of vectors included in the average decreased by up to 30 percent ,and average standard deviation components both increased by up to 20 percent. Particle response curves indicated that results were either unchanged or produced a slightly elongated response.

5.3   Impact of Research

This research marks the development of a new research capability for AFRL RQVX. This was the first time that PIV was ever conducted in the Mach 3/ Mach 6 facility. Modifications necessary to the tunnel mark a substantial time and resource

investment, which can allow PIV measurements to be performed in that tunnel in the future. Experimentation also identified a previously unknown issue of moisture content in the tunnel system which can now be corrected if proper resources are dedicated to the problem. On the other hand, it may be advisable to use the water naturally present to conduct future PIV tests.

This research reaffirmed the concept that particle image velocimetry with cleanly seeded carbon dioxide particles, could be conducted in a supersonic environment. Successful measurement of carbon dioxide particle response produced similar results to previous experiments completed in smaller and lower Mach number facilities at the Air Force Institute of Technology.

As many PIV researchers can attest, the data is only as good as the software and analysis methods used to produce the vector maps. Researchers are often presented with a software package with numerous analysis options, the shear number of which can be overwhelming and confusing. The act of completing practical comparisons of analysis methods, augmentations, and filtering techniques has produced valuable information for the next researcher who may use the same software again.

Lastly a new concept of removing bright particles from the image data was attempted. Though this attempt was largely unsuccessful, it may give insight into future work.

5.4 Future Work

This research marks a significant investment in time dedicated toward developing the capability to conduct PIV experiments in the Mach 3/ Mach 6 Facility. It would therefore be a missed opportunity if more tests were not conducted using PIV in that facility. A limiting factor in the research presented in this thesis was the presence of ambient moisture within the tunnel system. If that moisture could be eliminated,

the original goal of characterizing particles produced by various generation methods could again be a possibility. If the issue of ambient moisture could not be easily addressed, the concept of using particle seeding to study a local flow structure could be considered. A jet in cross flow experiment could be implemented using carbon dioxide particles at the test section. Particle response experiments could also be conducted in other supersonic wind tunnels using a similar configurations allowing the collection of data that was unbiased by the presence of water particles. A significant portion of carbon dioxide research at AFIT has also been dedicated to the Tri-sonic Gas Dynamics Facility. This research is ultimately motivated by the idea of cleanly seeding the Tri-sonic Gas Dynamics Facility and developing PIV capability there. Thus, a return to the TGF armed with lessons learned in this research , could prove a valuable endeavor.

Appendix A. Full Test Matrix

Run #	Time	Run Date	Lens Used (mm)	Camera F-Stop	Run Time (sec)	Laser Setting Attenuator, L1 L2	Delta t (microsec)	Upstream Port Configuration	Downstream Port Configuration	Po (Psi)	To (Kelvin)	Presence of Water Particles	Outside Temps (Degrees F)
1	9:05	1/20/2016	60	4	35	3,25,10,10	0.5	x	SST 1/4 OD 90 degree Bend	100	x	Likely not Present	16
2	10:18	1/20/2016	60	4	35	3,10,10	0.5	SST 3/8 OD	x	100	x	Likely not Present	16
3	10:36	1/20/2016	60	4	35	2,10,10	0.5	SST 3/8 OD	x	100	x	Likely not Present	16
4	10:44	1/20/2016	60	4	35	2,7,10	0.5	SST 3/8 OD	x	100	x	Likely not Present	16
5	8:56	2/5/2016	60	4	60	2.25,7,10	0.5	SST 3/8 OD	x	100	253	Likely not Present	29
6	9:21	2/5/2016	60	4	60	1.75,7,10	0.5	SST 3/8 OD	x	100	253	Likely not Present	29
7	9:47	2/5/2016	60	4	60	1.75,7,10	0.5	SMT 3/8 OD	x	100	253	Likely not Present	29
8	10:01	2/5/2016	60	4	60	1.75,7,10	0.5	SMT 3/8 OD	x	100	253	Likely not Present	29
9	10:18	2/5/2016	60	4	60	1.75,7,10	0.5	SMT 3/8 OD	x	100	253	Likely not Present	29
10	8:54	2/24/2016	60	4	70	1.75,7,10	0.5	SMT 3/8 OD	x	100	252	Likely Present	41
11	9:08	2/24/2016	60	4	70	1.75,7,10	0.5	SMT 3/8 OD	x	100	250	Likely Present	41
12	9:21	2/24/2016	60	4	66	1.75,7,10	0.5	SMT 3/8 OD	x	100	250	Likely Present	41
13	9:35	2/24/2016	60	4	66	1.75,7,10	0.5	SMT 3/8 OD	x	100	250	Likely Present	41
14	10:00	2/24/2016	60	4	67	1.75,7,10	0.5	SMT 3/8 OD	x	100	250	Likely Present	41
15	10:15	2/24/2016	60	4	63	3,7,10	0.5	SMT 3/8 OD	x	100	250	Likely Present	41
16	10:35	2/24/2016	60	4	61	3,7,10	0.5	SMT 3/8 OD	x	150	253	Likely Present	41
17	10:50	2/24/2016	60	4	64	3,7,10	0.5	SMT 3/8 OD	x	150	253	Likely Present	41
18	11:08	2/24/2016	60	4	63	3,7,10	0.5	SMT 3/8 OD	x	150	253	Likely Present	41
19	11:33	2/24/2016	60	4	60	3,7,10	0.5	SMT 3/8 OD	x	150	255	Likely Present	41
20	11:44	2/24/2016	60	4	64	3,7,10	0.5	SMT 3/8 OD	x	150	256	Likely Present	41
21	9:08	2/29/2016	60	4	59	3,7,10	0.5	SMT 3/8 OD	x	100	250	Likely Present	45
22	10:01	2/29/2016	60	4	60	3,7,10	0.5	SMT 3/8 OD	x	100	249	Likely Present	45
23	10:10	2/29/2016	60	4	65	2.5,6,10	0.5	SMT 3/8 OD	x	100	249	Likely Present	45
24	10:21	2/29/2016	60	4	60	2.5,6,10	0.5	SMT 3/8 OD	x	100	249	Likely Present	45
25	10:33	2/29/2016	60	4	70	2.5,6,10	0.5	SMT 3/8 OD	x	100	248	Likely Present	45
26	10:39	2/29/2016	60	4	65	2.5,6,10	0.5	SMT 3/8 OD	x	100	248	Likely Present	45
27	10:48	2/29/2016	60	4	80	2.5,6,10	0.5	SMT 3/8 OD	x	100	248	Likely Present	45
28	9:01	3/1/2016	60	4	65	2.5,6,10	0.5	SMT 3/8 OD	x	100	254	Likely Present	39
29	9:17	3/1/2016	60	4	60	2.5,6,10	0.5	SMT 3/8 OD	x	100	254	Likely Present	39

Mach 3 Particle Response Test Matrix Page 1

Table 6. Test Matrix Page 1

Mach 3 Particle Response Test Matrix Page 2

Run #	Run Time	Run Date	Lens Used (mm)	Camera F-Stop	Run Time (sec)	Laser Setting Attenuator, L1,L2	Delta t (microsec)	Upstream Port Configuration	Downstream Port Configuration	Po (Psi)	To (Kelvin)	Presence of Water Particles	Outside Temps (Degrees F)
30	10:20	3/1/2016	60	4	65	2.75,6.5,10	0.5	x	x	100	254	Likely Present	39
31	10:31	3/1/2016	60	4	60	2.75,6.5,10	0.5	x	x	100	254	Known to be Present	39
32	8:55	3/3/2016	60	4	60	2.75,6.5,10	0.5	x	x	100	255	Known to be Present	34
33	9:41	3/3/2016	60	4	60	2.75,6.5,10	0.5	x	x	100	255	Known to be Present	34
34	8:53	3/9/2016	60	4	60	2.75,6.5,10	0.5	x	x	100	256	Known to be Present	65
35	9:21	3/9/2016	60	4	62	2.75,6.5,10	0.5	SMT 3/8 OD	x	100	256	Known to be Present	65
36	9:39	3/9/2016	60	4	62	2.75,6.5,10	0.5	SMT 3/8 OD	x	100	256	Known to be Present	65
37	9:44	3/9/2016	60	4	61	2.75,6.5,10	0.5	SMT 3/8 OD	x	100	258	Known to be Present	65
38	9:53	3/9/2016	60	4	67	1.75,6.5,10	0.5	SMT 3/8 OD	x	100	258	Known to be Present	65
39	10:07	3/9/2016	60	4	61	1.75,6.5,10	0.5	x	x	100	258	Known to be Present	65
40	10:15	3/9/2016	60	4	120	1.75,6.5,10	0.5	x	x	100	258	Known to be Present	65
41	10:39	3/9/2016	60	4	60	1.75,6.5,10	0.5	SST 3/8 OD	x	100	258	Known to be Present	65
42	8:56	3/10/2016	60	4	60	1.75,6.5,10	0.5	x	x	100	258	Known to be Present	54
43	9:02	3/10/2016	60	4	62	1.75,6.5,10	0.5	x	SST 1/4 OD	100	255	Known to be Present	54
44	9:08	3/10/2016	60	4	62	1.75,6.5,10	0.5	x	SST 1/4 OD	100	254	Known to be Present	54
45	9:13	3/10/2016	60	4	61	1.75,6.5,10	0.5	x	SST 1/4 OD	100	253	Known to be Present	54
46	10:15	3/10/2016	60	4	120	1.75,6.5,10	0.5	x	Oil Seeder	100	253	Known to be Present	54
47	8:58	3/11/2016	105	4	60	2.75,6.5,10	0.5	x	x	100	257	Known to be Present	49
48	9:02	3/11/2016	105	4	150	2.75,6.5,10	0.5	x	Oil Seeder	100	256	Known to be Present	49
49	9:21	3/11/2016	105	4	60	2.75,6.5,10	0.5	x	Oil Seeder	100	255	Known to be Present	49
50	9:25	3/11/2016	105	4	60	2.75,6.5,10	0.5	x	Oil Seeder	100	253	Known to be Present	49
51	9:29	3/11/2016	105	4	60	2.75,6.5,10	0.5	x	Oil Seeder	100	252	Known to be Present	49
52	9:35	3/11/2016	105	4	60	2.75,6.5,10	0.5	x	Oil Seeder	100	252	Known to be Present	49
53	9:54	3/11/2016	105	4	90	2.75,6.5,10	0.5	SMT 3/8 OD	x	100	252	Known to be Present	49
54	9:59	3/11/2016	105	4	90	2.75,6.5,10	0.5	SMT 3/8 OD	x	100	252	Known to be Present	49
55	10:04	3/11/2016	105	4	60	2.75,6.5,10	0.5	SMT 3/8 OD	x	100	252	Known to be Present	49
56	10:13	3/11/2016	105	4	60	2.75,6.5,10	0.5	x	SST 3/8 OD	100	250	Known to be Present	49
57	10:19	3/11/2016	105	4	60	2.75,6.5,10	0.5	x	SST 3/8 OD	100	250	Known to be Present	49
58	10:24	3/11/2016	105	4	60	2.75,6.5,10	0.5	x	SST 3/8 OD	100	250	Known to be Present	49

Table 7.   Test Matrix Page 2

Appendix B. Case Configurations Table

| Case	Particle Type	Lens (mm)	Analysis Method	Interrogation Region Dimensions (Pixels)	Peak Ratio Validation	Gaussian Filter K Value	Dantec Image Pre-Processing Applied?	Large Particle Filtering Applied?	Beta Theta Mach Prediction	Average Free Stream Velocity	Theorectical Velocity	% Difference	Matched Velocity To	Average % of Vectors Used	Average Horizontal Standard Deviation	Average Vertical Standard Deviation
1.1	CO2	60	Cross Correlation	32x32	1.25	x	No	No	2.983	554	570.457	-2.8847	238.61	21	51.0183	36.6025
1.2	CO2	60	Cross Correlation	32x32	1.25	x	Yes	No	2.983	560.5443	570.457	-1.7377	244.28	26.66	42.5781	35.001
1.3	CO2	60	Adaptive PIV	32x32 -	1.25	x	Yes	No	2.983	570.8534	570.457	0.0695	253.2	59.5419	30.3104	28.8697
1.4	CO2	60	Least Squares Method	32x32	N/A	x	Yes	No	x	x	x	x	x	x	x	x
1.5	CO2	60	Cross Correlation	64x64	1.25	x	Yes	No	2.983	566.1667	570.457	-0.7521	249.209	51.2725	32.524	30.8633
2.1	CO2	60	Cross Correlation	32x32	1.25	x	No	No	2.989	568.6275	570.869	-0.3926	251.07	62.8527	33.0688	23.4624
2.2	CO2	60	Cross Correlation	32x32	1.5	x	No	No	2.989	569.1087	570.869	-0.3083	251.44	56.89	32.49	23.0792
2.3	CO2	60	Cross Correlation	32x32	1.25	1.2	No	No	2.989	568.604	570.869	-0.3967	250.997	64.607	31.31114	23.001
2.4	CO2	60	Cross Correlation	64x64	1.25	x	No	No	2.989	573.9709	570.869	0.5434	255.7571	81.0166	23.374	18.4785
2.5	CO2	60	Adaptive PIV	32x32 -	1.25	x	No	No	2.989	582.4293	570.869	2.0251	263.35	97.9923	16.3391	15.0631
2.6	CO2	60	Least Squares Method	~ 64x64	N/A	N/A	No	No	x	x	x	x	x	x	x	x
2.7	CO2	60	Cross Correlation	32x32	1.25	x	Yes	No	2.989	570.1657	570.869	-0.1232	252.3771	60.5289	32.2789	23.2789
2.8	CO2	60	Cross Correlation	32x32	1.25	x	Yes	Yes	2.989	569.3048	570.869	-0.2741	251.6152	32.8882	38.8463	27.8815
2.9	CO2	60	Cross Correlation	64x64	1.25	x	Yes	Yes	2.989	573.22	570.869	0.4119	255.0883	54.2256	29.5928	22.5693
3.1	Water	60	Cross Correlation	32x32	1.25	x	No	No	2.928	550.6021	568.8402	-3.2062	238.91	43.0058	20.6856	17.1175
3.2	Water	60	Cross Correlation	32x32	1.5	x	No	No	2.928	550.7547	568.8402	-3.1794	239.0431	40.1393	20.2637	16.8801
3.3	Water	60	Cross Correlation	32x32	1.25	1.2	No	No	2.928	550.6327	568.84	-3.2008	238.9371	44.5059	20.1598	16.8595
3.4	Water	60	Cross Correlation	64x64	1.25	x	No	No	2.928	551.2927	568.8402	-3.0848	239.5102	53.1455	16.1772	13.6582
3.5	Water	60	Adaptive PIV	32x32 - 64x64	1.25	x	No	No	2.928	550.99	568.8402	-3.1379	239.5102	61.3094	14.5369	13.3554

Table of Case Analysis Configurations Page 1

Table 8. Table of Case Configurations Page 1

Table of Case Analysis Configurations Page 2

| Case	Particle Type	Lens	Analysis Method	Interrogation Region Dimensions (Pixels)	Peak Ratio Validation	Gaussian Filter K Value	Dantec Image Pre-Processing Applied?	Large Particle Filtering Applied?	Beta Theta Mach Prediction	Average Free Stream Velocity	Theorectical Velocity	% Difference	Matched Velocity To	Average % of Vectors Used	Average Horizontal Standard Deviation	Average Vertical Standard Deviation
3.6	Water	60	Least Squares Method	~64x64	N/A	N/A	No	No	2.928	552.9582	568.8402	-2.792	240.9596	14.7099	19.4602	19.607
3.7	Water	60	Cross Correlation	32x32	1.25	x	Yes	No	2.928	551.6578	568.8402	-3.0206	239.8279	42.5054	21.1507	17.6273
3.8	Water	60	Cross Correlation	32x32	1.25	x	Yes	Yes	2.928	550.2414	568.8402	-3.2696	238.5977	43.0022	26.2454	17.864
3.9	Water	60	Cross Correlation	64x64	1.25	x	Yes	Yes	2.928	550.3983	568.8402	-3.242	238.7337	66.5313	18.1	12.1094
4.1	Water	60	Cross Correlation	32x32	1.25	x	No	No	2.881	561.567	566.5324	-0.8765	251.5322	21.9232	24.4462	21.9232
4.2	Water	60	Cross Correlation	64x64	1.25	x	No	No	2.881	563.3501	566.5324	-0.5617	253.132	54.8027	25.9268	18.04
4.3	Water	60	Adaptive PIV	32x32 -	1.25	x	No	No	2.881	565.1156	566.5324	-0.2501	254.72	61.1604	21.7312	17.0385
4.4	Water	60	Least Squares Method	~ 64x64	1.25	x	No	No	x	x	x	x	x	x	x	x
5.1	Water	105	Cross Correlation	32x32	1.25	x	No	No	2.924	546.23	571.0009	-4.3378	235.37	56.8721	24.8449	21.3308
5.2	Water	105	Cross Correlation	64x64	1.25	x	No	No	2.924	550.6238	571.0009	-3.5687	239.1704	79.2723	15.1826	14.54
5.3	Water	105	Adaptive PIV	32x32 to 64x64	1.25	x	No	No	2.924	552.8461	571.0009	-3.1795	241.1048	91.456	12.393	13.1547
5.4	Water	105	Least Squares Method	~ 64x64	1.25	x	No	No	2.924	553.8056	571.0009	-3.0114	241.9425	15.3107	22.3395	21.463
6.1	CO2/Water Mix	105	Cross Correlation	32x32	1.25	x	No	No	2.863	541.4657	560.9835	-3.4792	234.9562	25.6531	37.6191	25.6531
6.2	CO2/Water Mix	105	Cross Correlation	64x64	1.25	x	No	No	2.863	549.4418	560.9835	-2.0574	241.9293	51.458	23.2441	21.4268
6.3	CO2/Water Mix	105	Adaptive PIV	32x32 -64x64	1.25	x	No	No	2.863	552.3193	560.9835	-1.5445	244.4699	71.7947	21.0849	18.7847
6.4	CO2/Water Mix	105	Least Squares Method	~64x64	1.25	x	No	No	2.863	x	x	x	x	x	x	x
6.5	CO2/Water Mix	105	Cross Correlation	64x64	1.25	x	Yes	Yes	2.863	549.3854	560.9835	-2.0675	241.8795	40.7412	27.1445	23.166
7.1	CO2/Water Mix	105	Cross Correlation	32x32	1.25	x	No	No	2.88	543.908	559.7809	-2.8356	236.0232	27.8981	36.1334	30.3573
7.2	CO2/Water Mix	105	Cross Correlation	64x64	1.25	x	No	No	2.88	552.0108	559.7809	-1.3881	243.1079	55.1387	22.4653	20.5938
7.3	CO2/Water Mix	105	Adaptive PIV	32x32- 64x64	1.25	x	No	No	2.88	554.2224	559.7809	-0.993	245.0597	72.9045	19.0172	18.0479
7.4	CO2/Water Mix	105	Least Squares Method	~ 64x64	1.25	x	No	No	x	x	x	x	x	x	x	x

Table 9.   Table of Case Configurations Page 2

118

Appendix C.   Additional Contour and Particle Response Plots
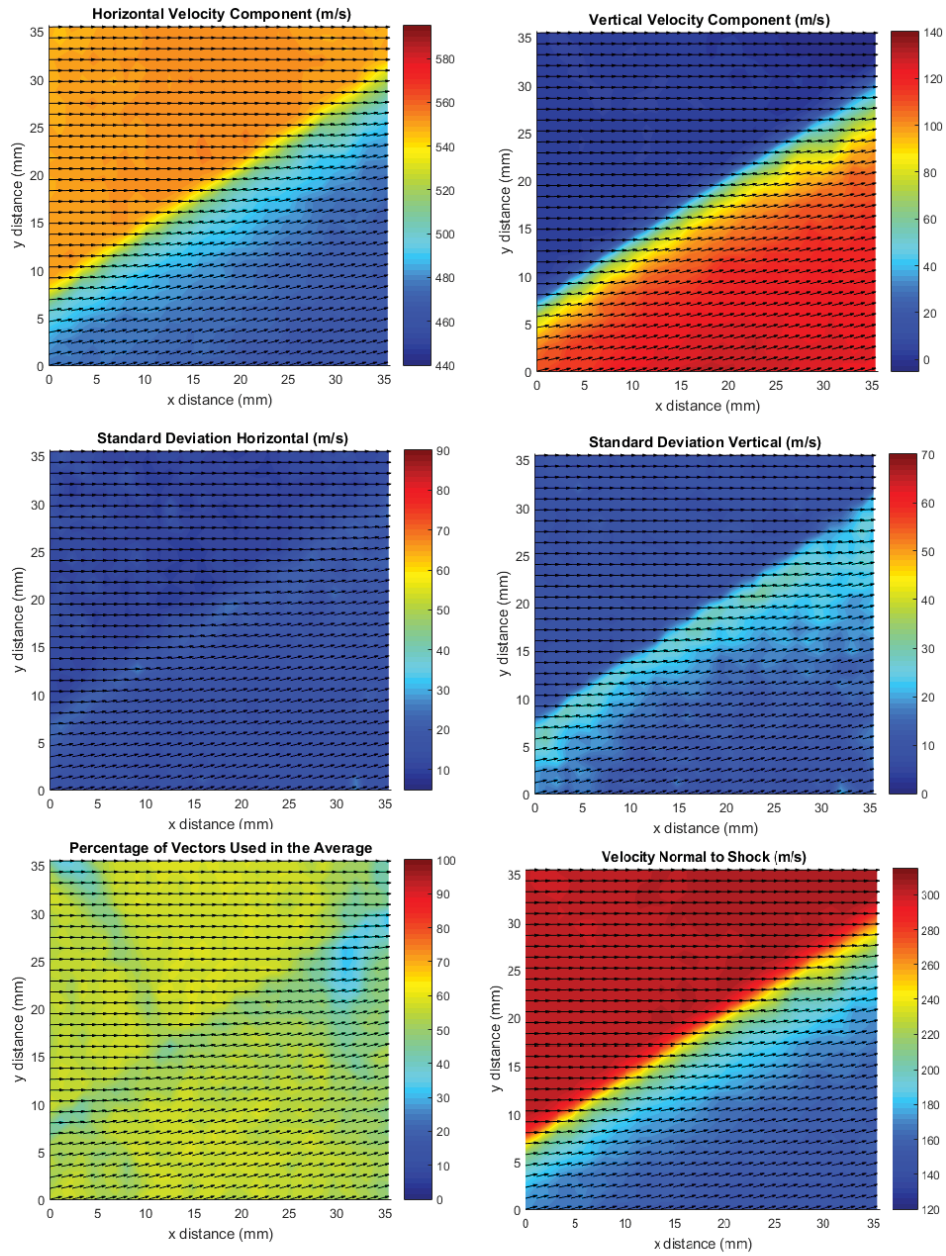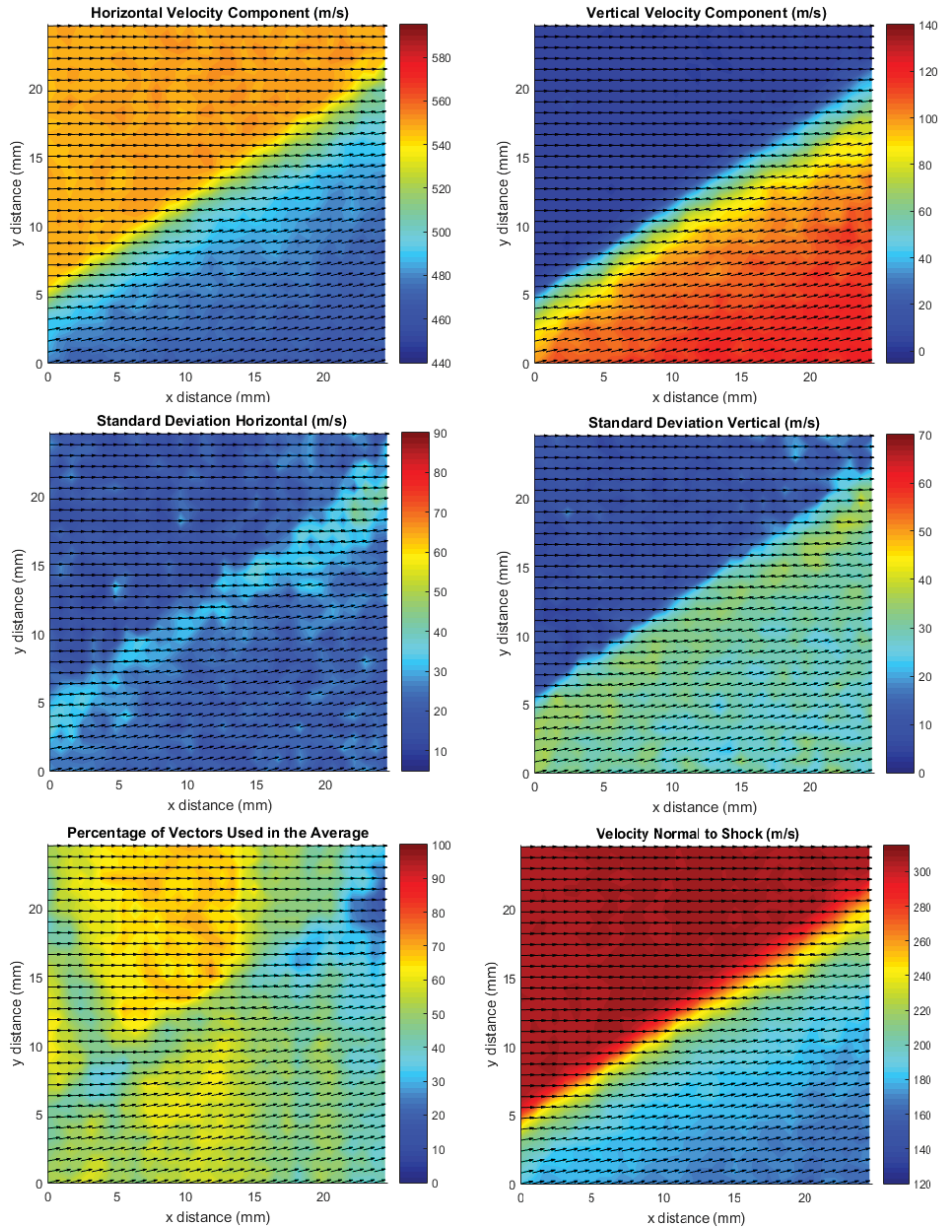

Case 3 Cross Correlation 64x64 IR

Figure 78.   Contains 6 contour plots from Case 3
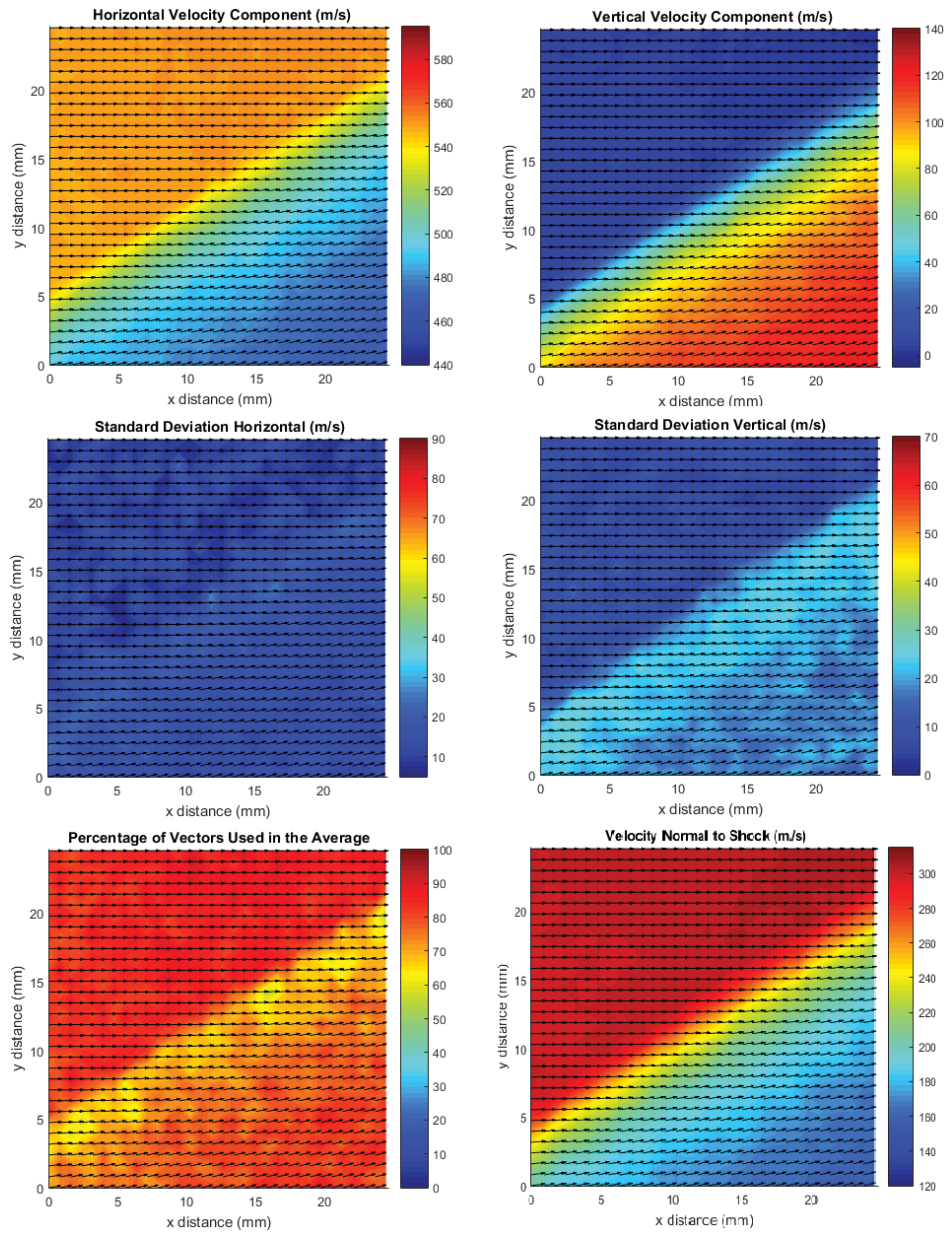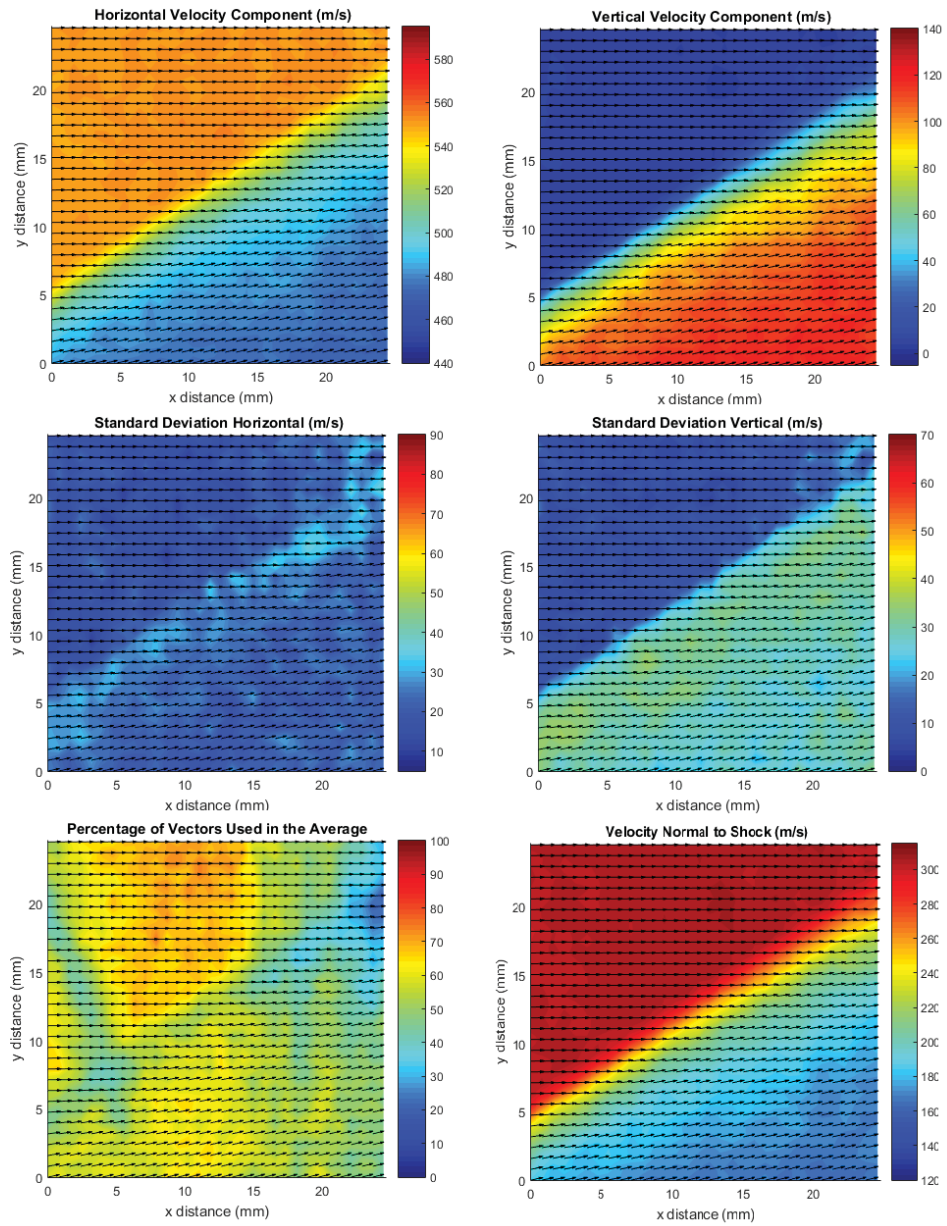
Case 5 Cross Correlation 64x64 IR

Figure 79. Contains 6 contour plots from Case 5

Case 6 Cross Correlation 64x64 IR

Figure 80.   Contains 6 contour plots from Case 6

CASE 7 Cross Correlation 64x64 IR
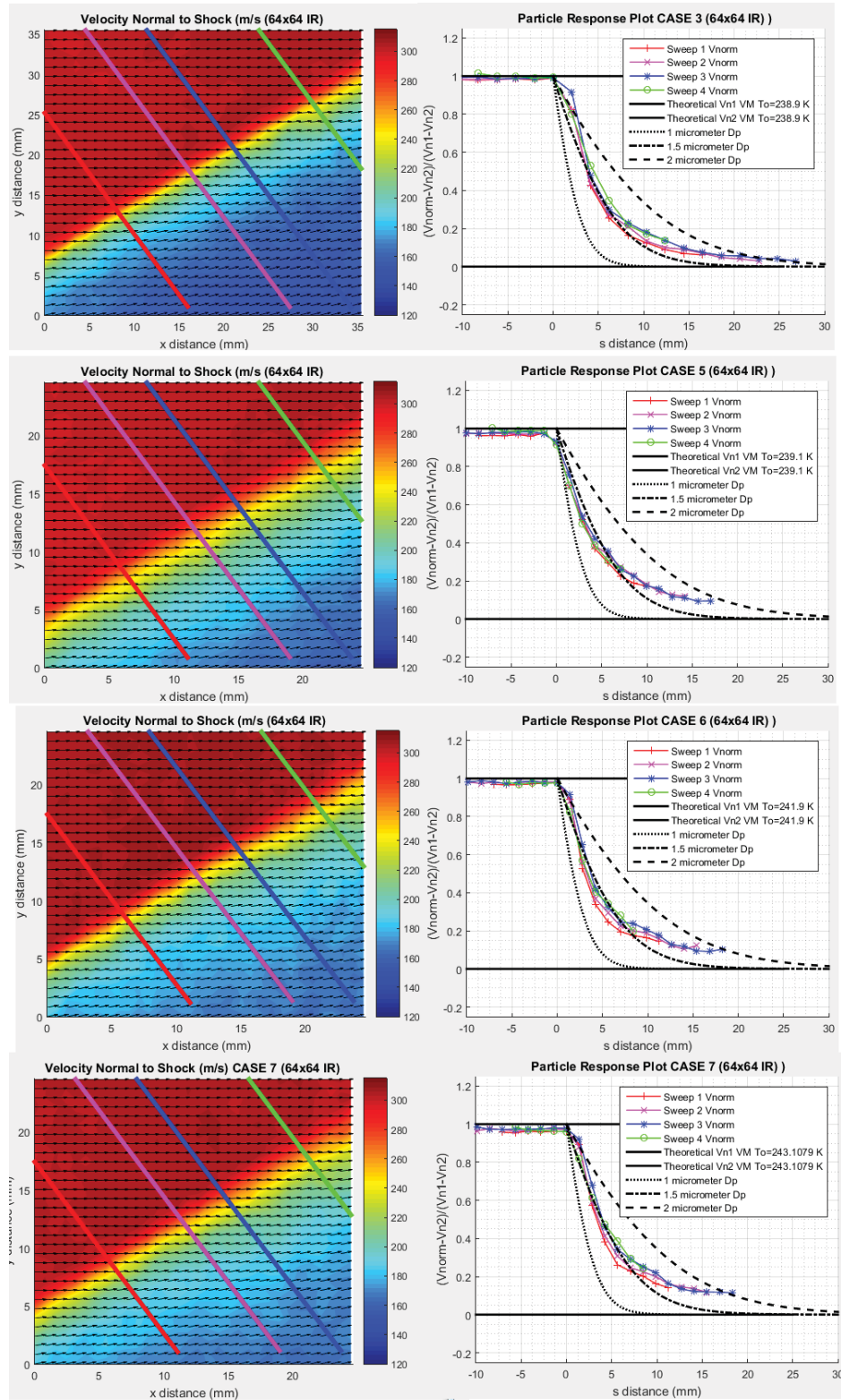
Figure 81.   Contains 6 contour plots from Case 7

Figure 82. Normalized particle response plots from Cases 3,5,6,7

Appendix D.   Particle Images

Explanation of Particle Images

Appendix D is meant to display examples of particle images in Cases 1 through 7. More specifically, these images are included to show the distinctions between including carbon dioxide particles (Cases 1, 2, 6, and 7) and cases featuring exclusively ambient water particles (Cases 3, 4, and 5). Appendix D , for all 7 cases, provides an image prior to tunnel operation which reflects the presence of carbon dioxide particles in cases where active seeding was included, and shows no particles in the ambient water cases. Appendix D also includes 10 representative frames from the Region of interest for each case (a total of 70 images). These frames are provided to show the representative variations in seeding, but also to show the global similarities between cases including Carbon dioxide particles. For convenience the overview table from Chapter 4 is repeated as Table 10. Note that all images are inverted from black to white and have brightness and contrast adjustments. The photo editing technique is performed identically on all images for the sake of unbiased comparison.

Table of Case Test Conditions										
Case	Particle Type	Test Date	Lens Size (mm)	Number of Runs Included	Number of Image Pairs	Laser Power	Upstream Port Configuration	Downstream Port Configuration	To (Kelvin)	Po (psi)
1	CO2	2/5/2016	60	1	109,129	Low	Simple Shroud Tube	Not Used	253	100
2	CO2	2/5/2016	60	2	196	Low	Static Mixing Tube	Not Used	253	100
3	Water	3/3/2016	60	2	266	High	Not Used	Not Used	255	100
4	Water	3/9/2016	60	1	280	Low	Not Used	Not Used	256	100
5	Water	3/11/2016	105	1	181	High	Not Used	Not Used	257	100
6	CO2/Water Mix	3/11/2016	105	3	392	High	Static Mixing Tube	Not Used	252	100
7	CO2/Water Mix	3/11/2016	105	3	406	High	Simple Shroud Tube	Not Used	250	100

Table 10.   Table Overview of Cases Examined

Case 1: Description and Images

Case 1 features Carbon Dioxide particle introduced using the simple shroud tube. This Case used 129 image pairs,the low laser intensity setting, and the 60 mm camera lens. Particles can be seen prior to tunnel activation, indicating the presence of carbon dioxide particle at the test section. Fine carbon dioxide condensate clouds are frequently visible within these images.

Figure 83. Contains 1 image of regions of interest from Case 1. This image contains full image before the tunnel is turned on. Carbon Dioxide particles are visible. Images is inverted from black to white
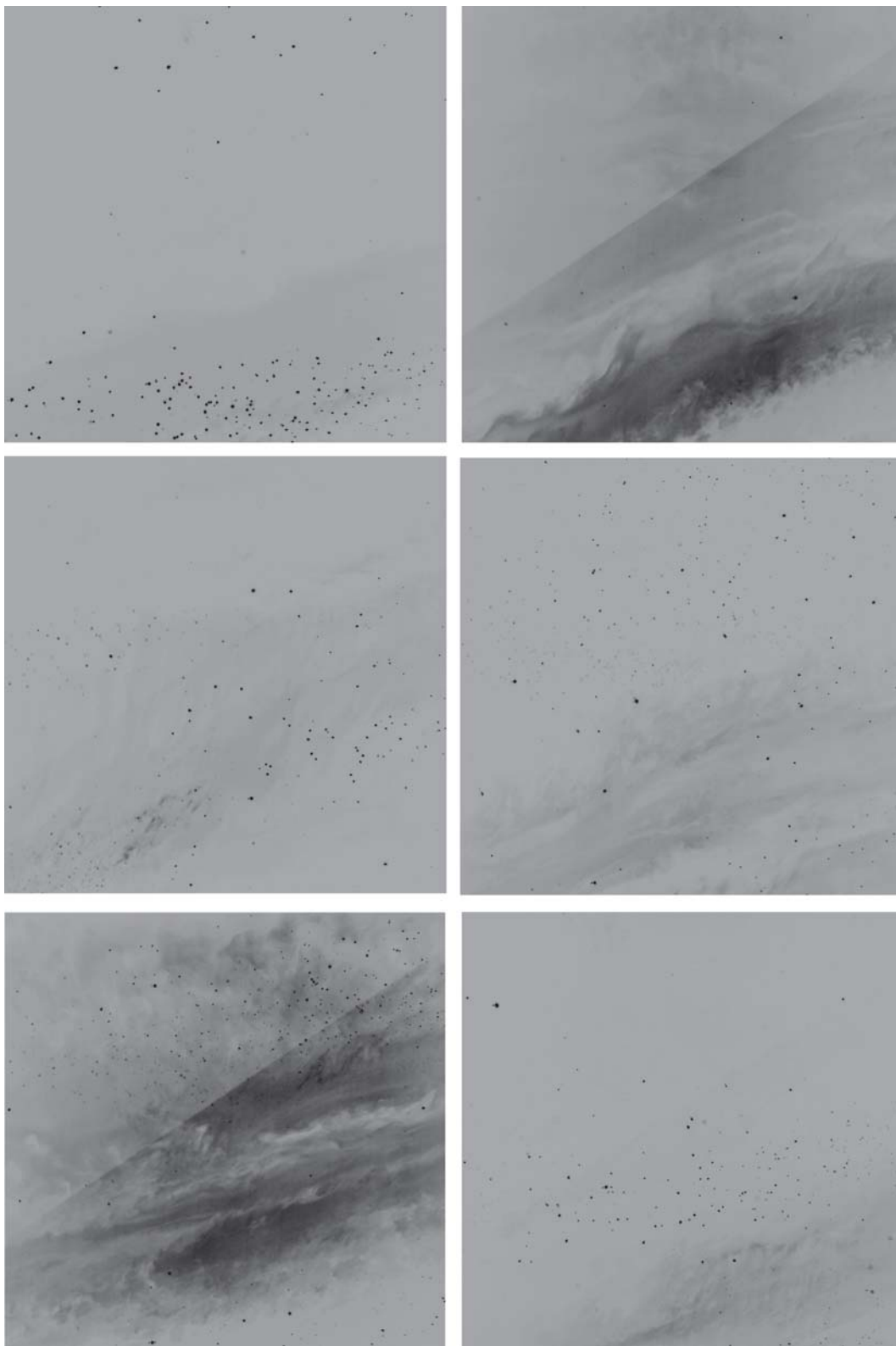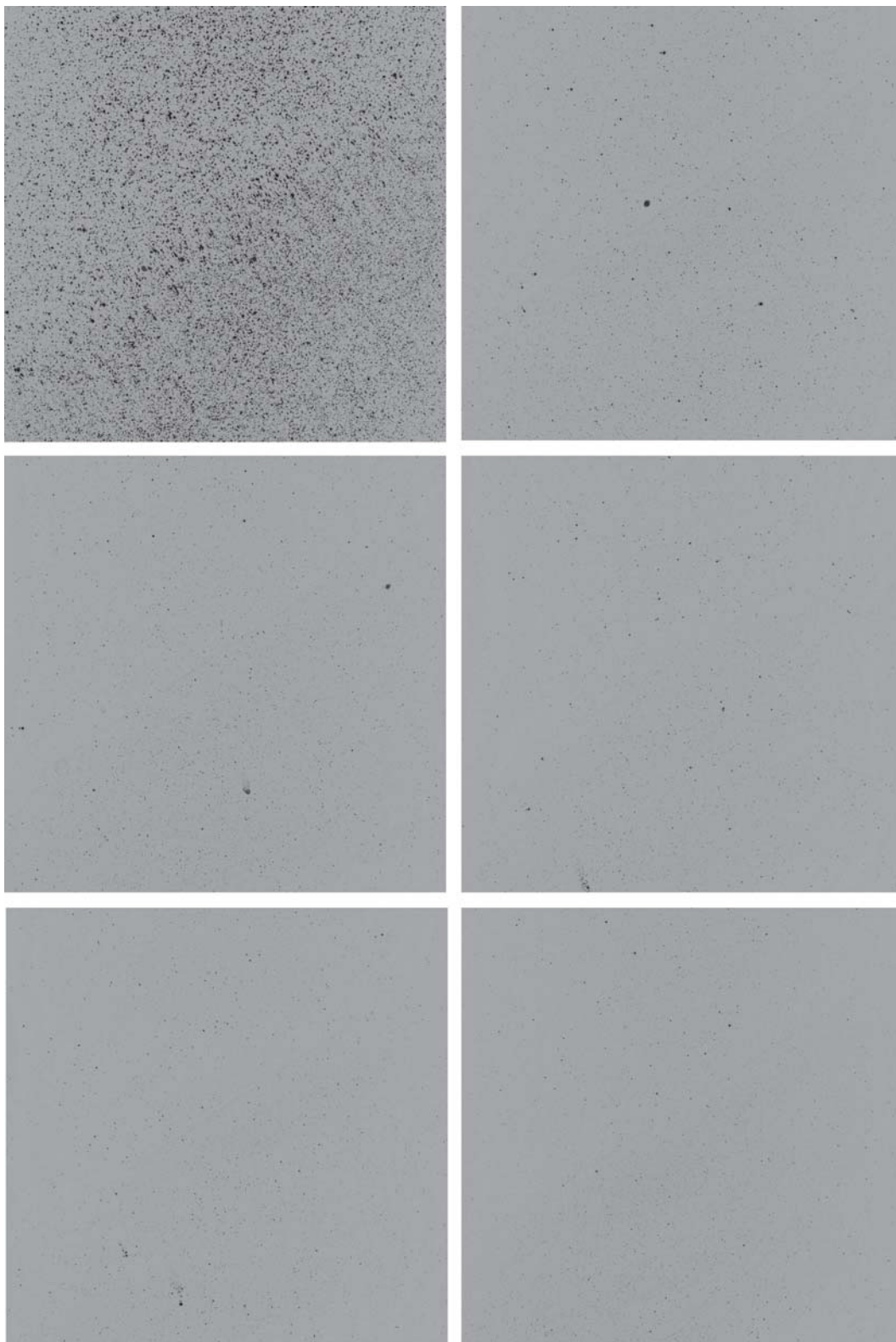
Figure 84.   Contains 6 images of regions of interest from Case 1. Images are inverted black to white

126
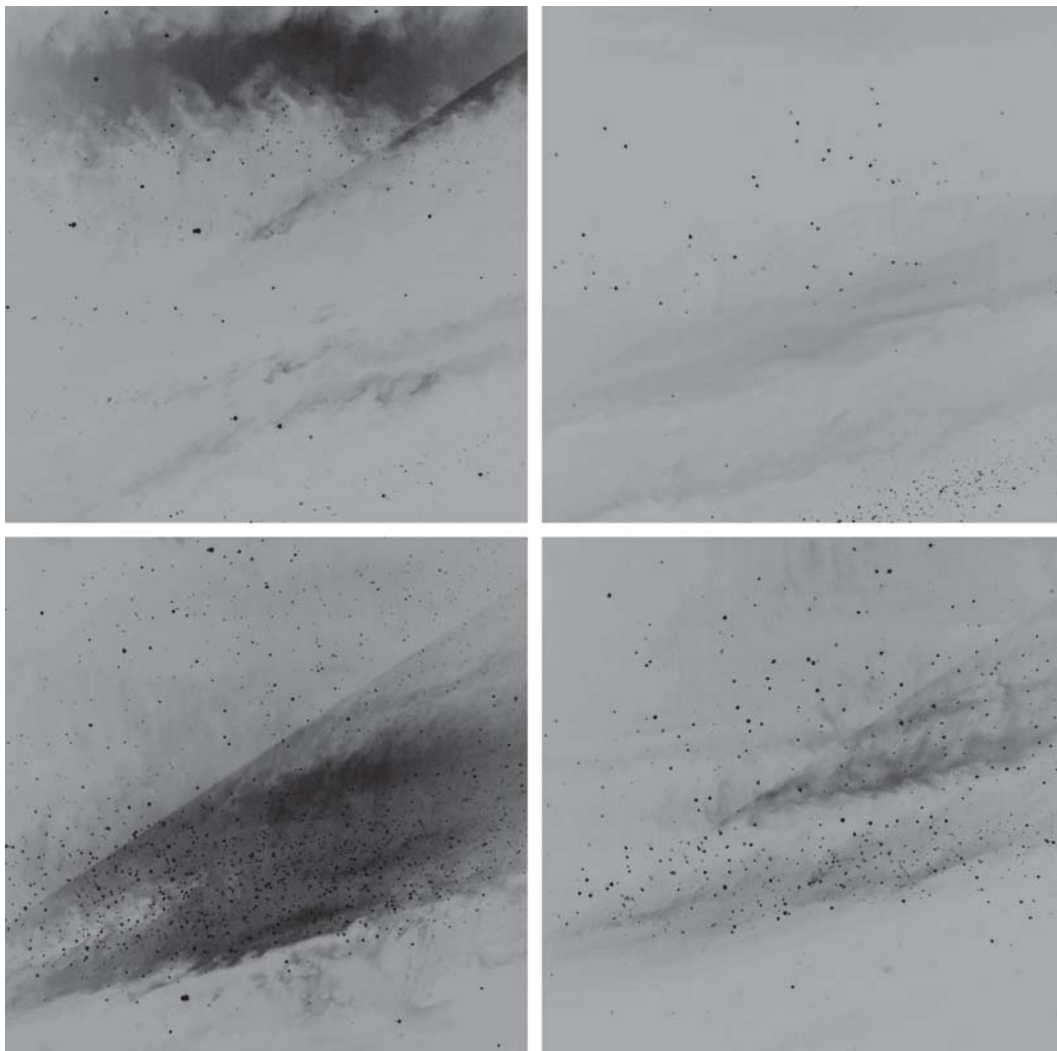
Figure 85. Contains 4 images of regions of interest from Case 1. Images are inverted black to white

Case 2: Description and Images

Case 2 features Carbon Dioxide particle introduced using the Static Mixing Tube. This Case used 196 image pairs,the low laser intensity setting, and the 60 mm camera lens. Particles can be seen prior to tunnel activation, indicating the presence of carbon dioxide particle at the test section. Fine carbon dioxide condensate clouds are sometime visible within these images.

Figure 86. Contains 1 image from Case 2. This image contains full image before the tunnel is turned on. Carbon Dioxide particles are visible. Images is inverted from black to white
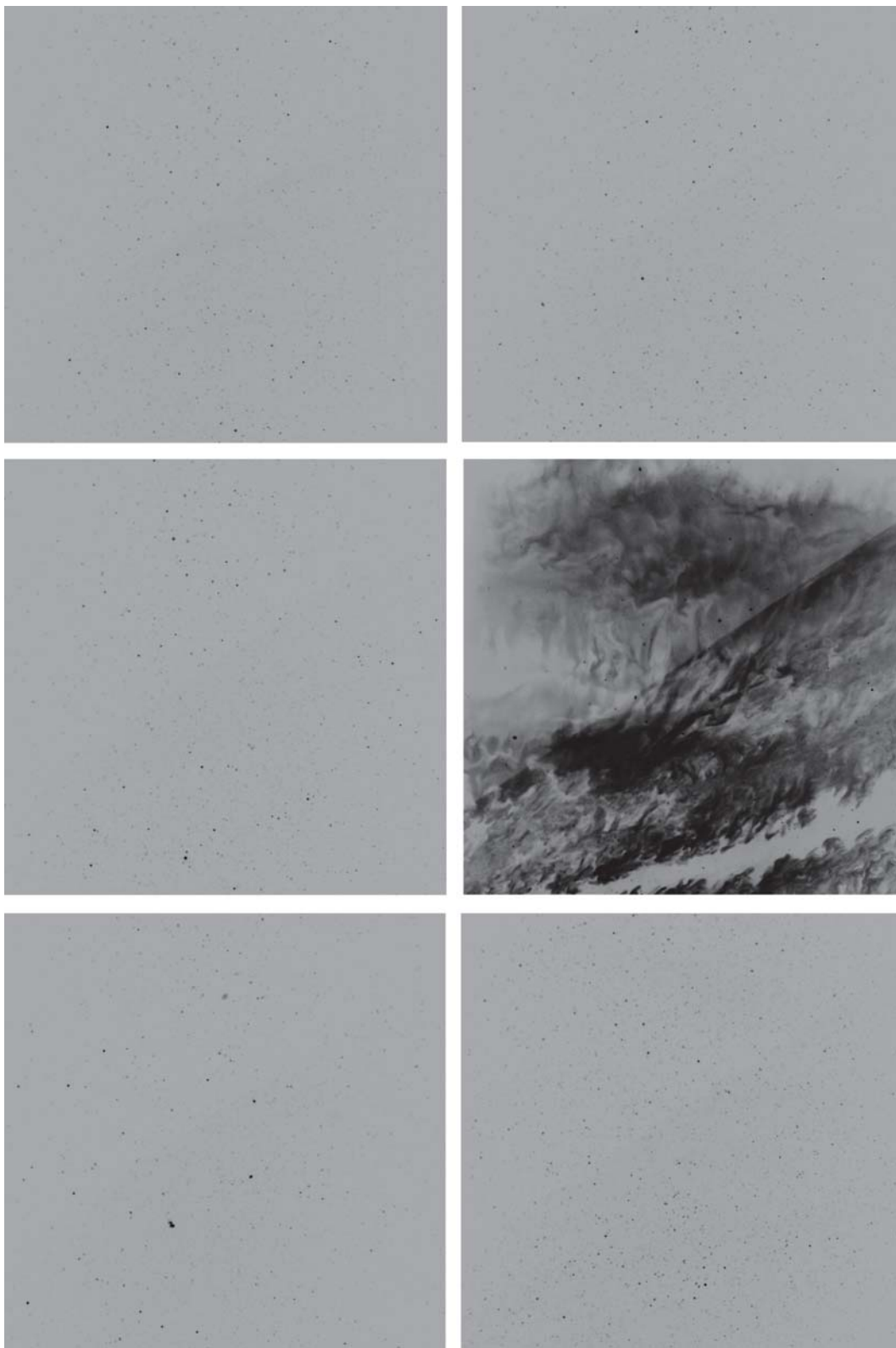
Figure 87. Contains 6 images of regions of interest from Case 2. Images are inverted black to white

129

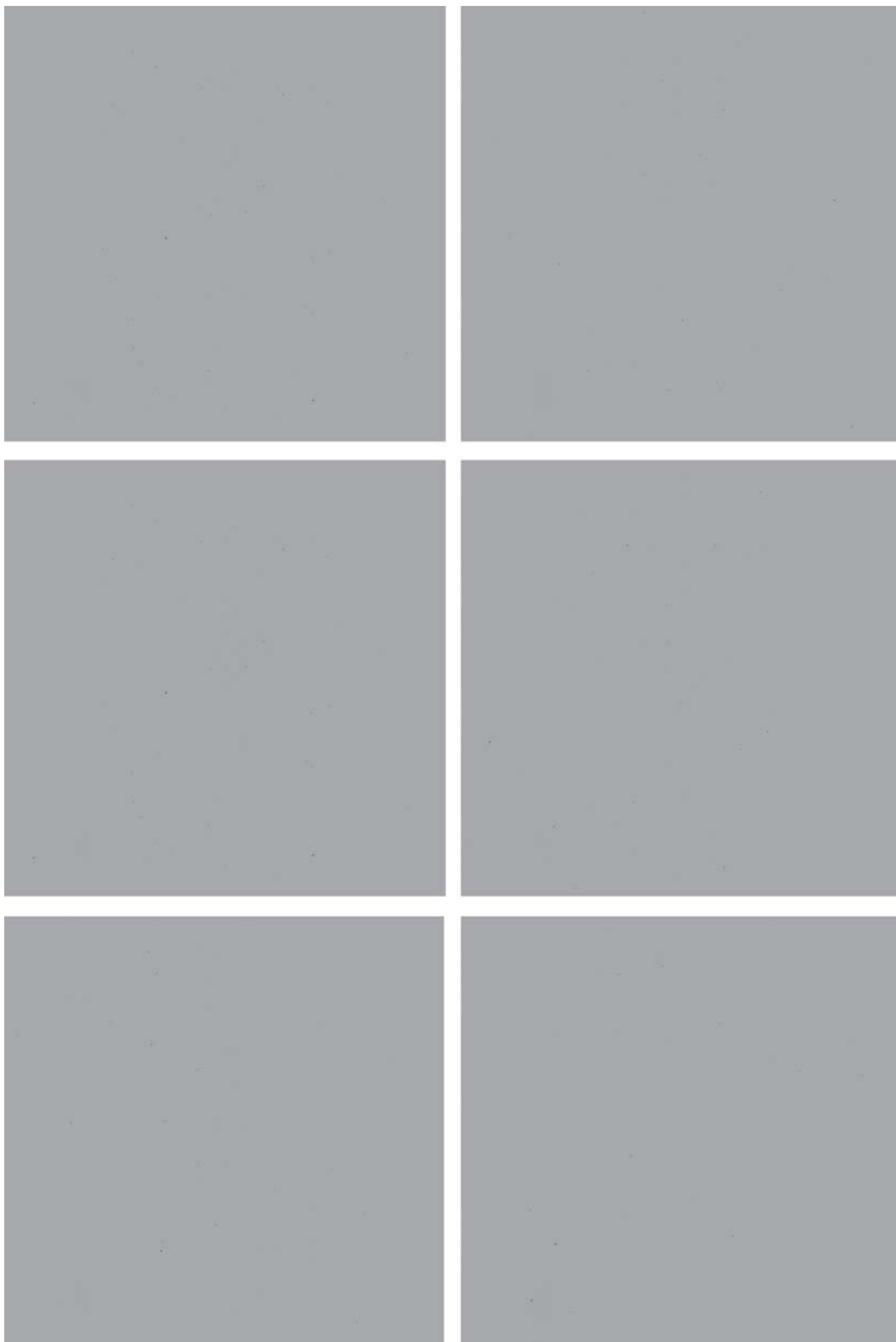Figure 88.   Contains 4 images of regions of interest from Case 2. Images are inverted black to white
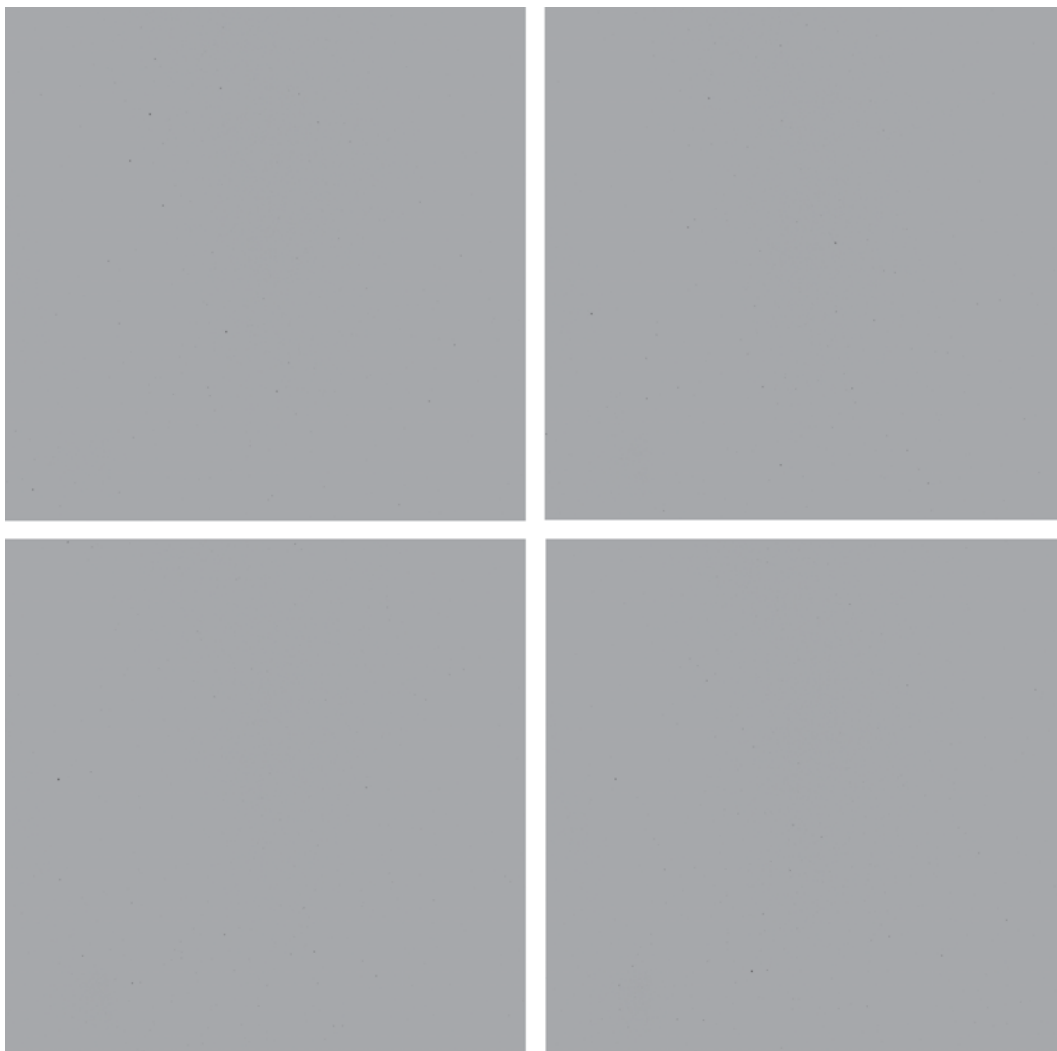
Case 3: Description and Images

Case 3 features only Ambient Water Particles. This case used 266 image pairs,the high laser intensity setting, and the 60 mm camera lens. No particles can be seen prior to tunnel activation.Lighting discontinuities can sometimes be seen in the shock region. Particle density and coverage was unsteady for this case and varied from medium to high density

Figure 89.   Contains 1 image from Case 3. This image contains full image before the tunnel is turned on. No particles are visible. Images is inverted from black to white

Figure 90. Contains 6 images of regions of interest from Case 3. Images are inverted black to white

132

Figure 91. Contains 4 images of regions of interest from Case 3. Images are inverted black to white

Case 4: Description and Images

Case 4 features only Ambient Water Particles. This case used 280 image pairs, the low laser intensity setting, and the 60 mm camera lens. No particles can be seen prior to tunnel activation. Particle density was very low for this case and signals were very weak for this particular data set. Thus, using the same image processing techniques utilized in the rest of the cases presented in Appendix D, the particles are very difficult to visualize. Despite limitations of this particular visual representation, particles are present and produced good PIV results.

Figure 92. Contains 1 image from Case 4. This image contains full image before the tunnel is turned on. No particles are visible. Images is inverted from black to white
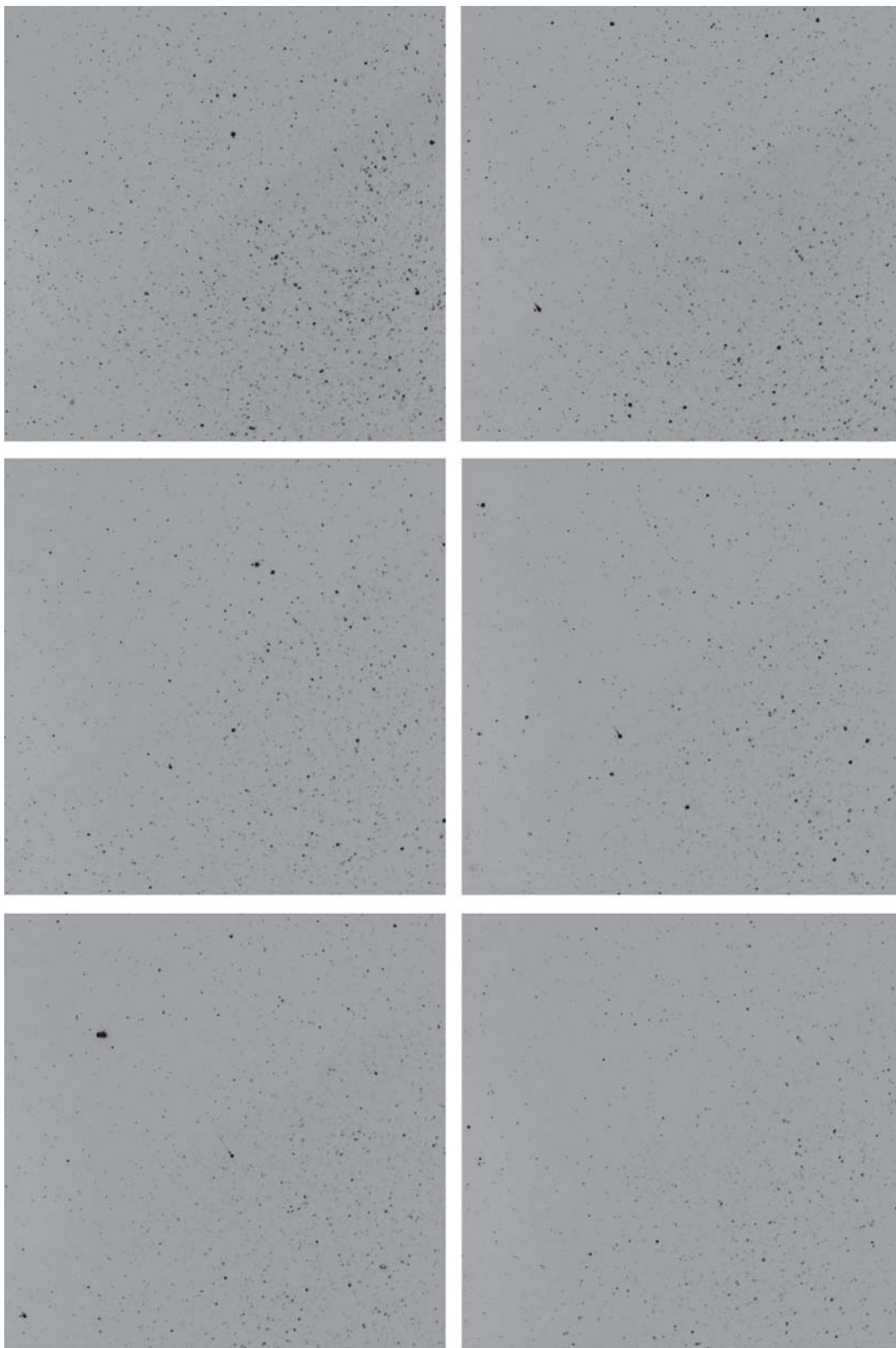
Figure 93. Contains 6 images of regions of interest from Case 4. Images are inverted black to white
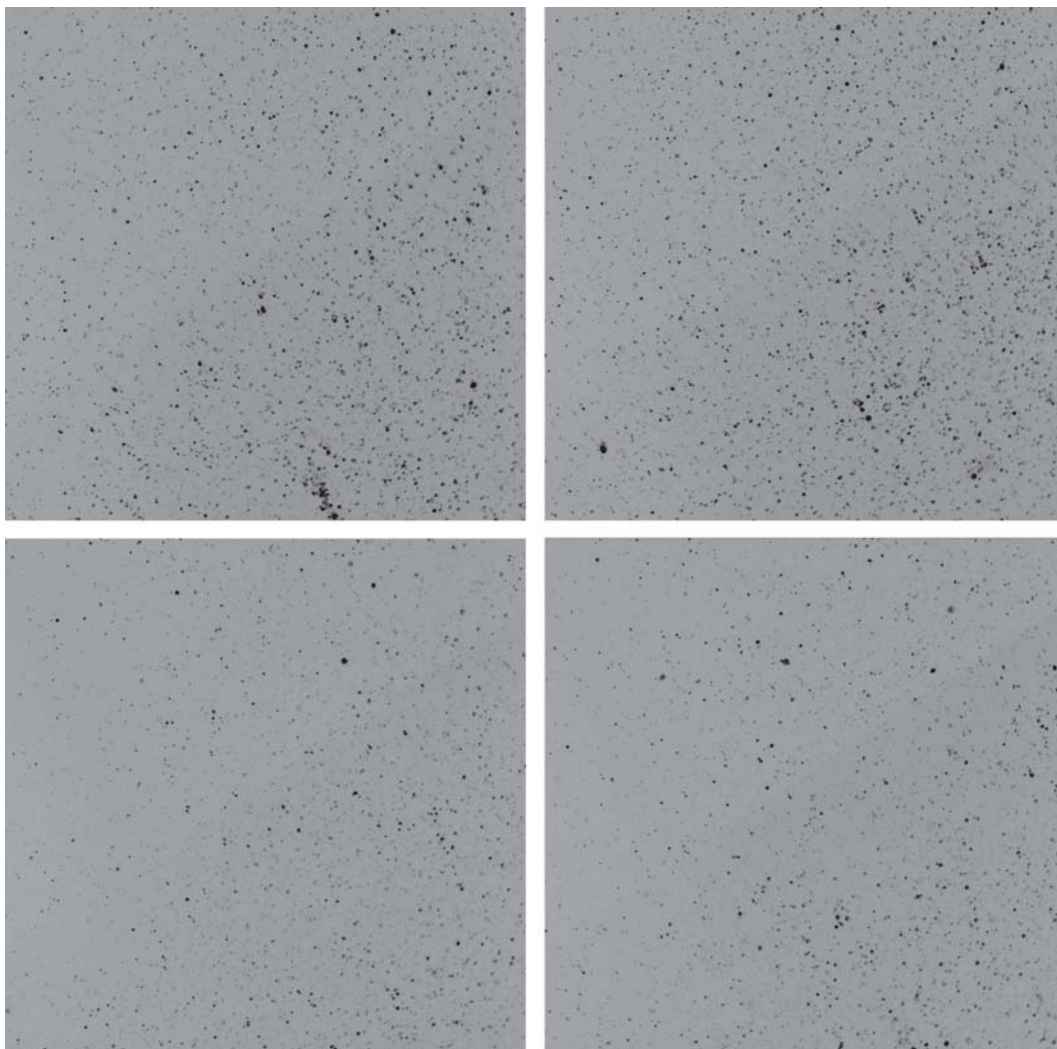
135

Figure 94.   Contains 4 images of regions of interest from Case 4. Images are inverted black to white

Case 5: Description and Images

Case 5 features only Ambient Water Particle. This case used 181 image pairs,the higher laser intensity setting, and the 105 mm camera lens. No particles can be seen prior to tunnel activation. Particle density was relatively high for this case. Note that particles appear larger due to increased magnification.

Figure 95. Contains 1 image from Case 5. This image contains full image before the tunnel is turned on. No particles are visible. Images is inverted from black to white

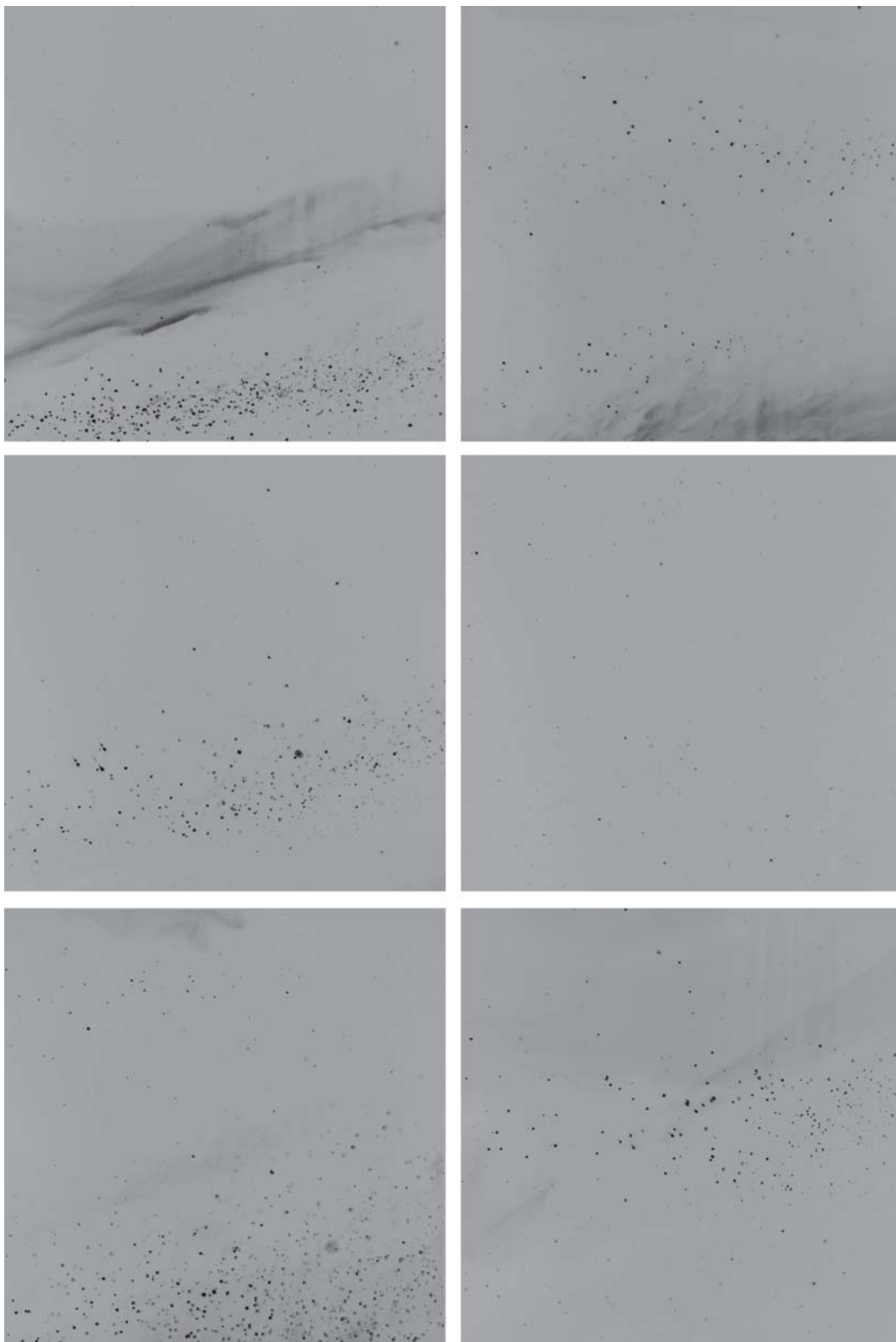**Figure 96.** Contains 6 images of regions of interest from Case 5. Images are inverted black to white
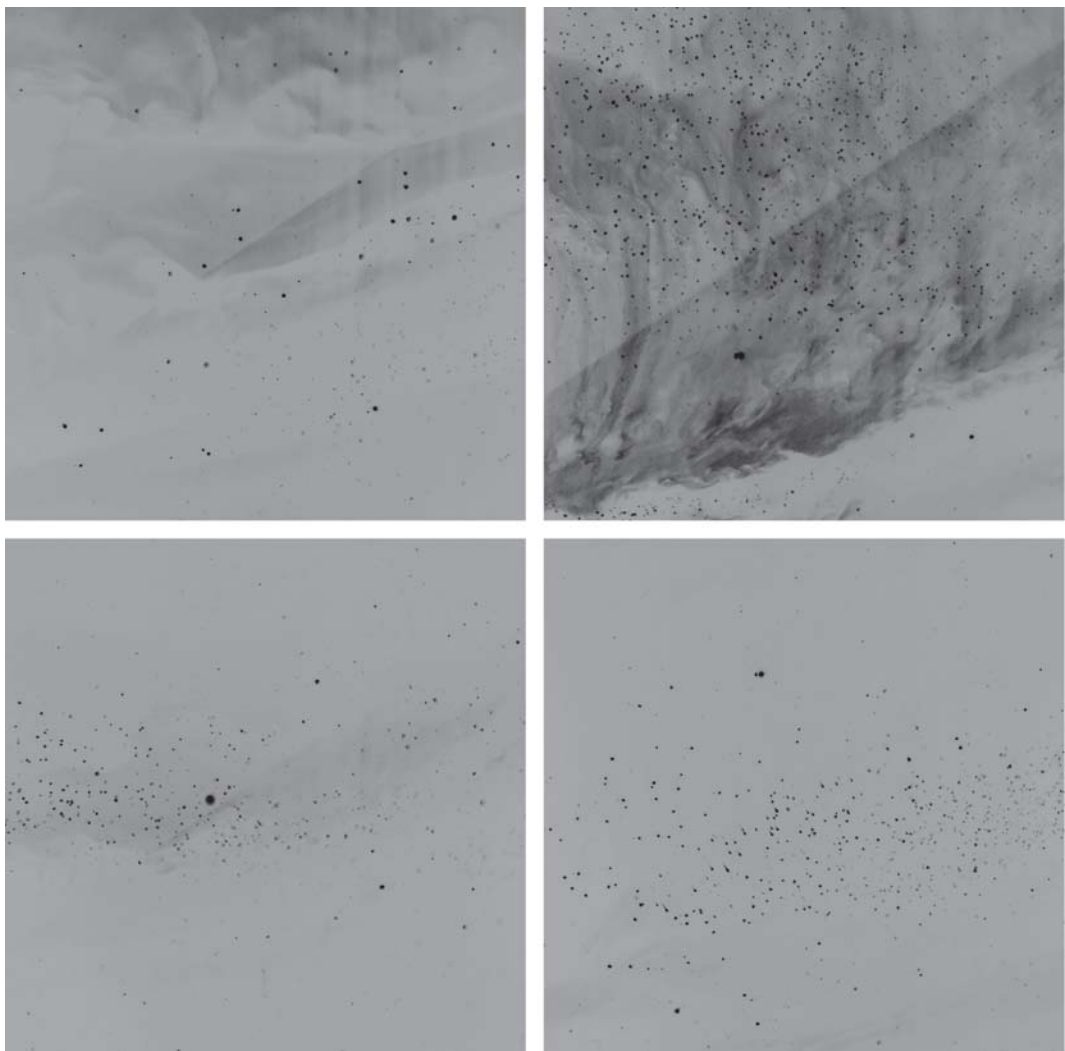
Figure 97. Contains 4 images of regions of interest from Case 5. Images are inverted black to white

Case 6: Description and Images

Case 6 features a mix of carbon dioxide particles (produced with the static mixing tube) and ambient water particles. This case used 392 image pairs,the higher laser intensity setting, and the 105 mm camera lens. There is visible carbon dioxide condensate clouds visible in these images.

Figure 98. Contains 1 image from Case 6. This image contains full image before the tunnel is turned on. Carbon dioxide particles are visible. Images is inverted from black to white
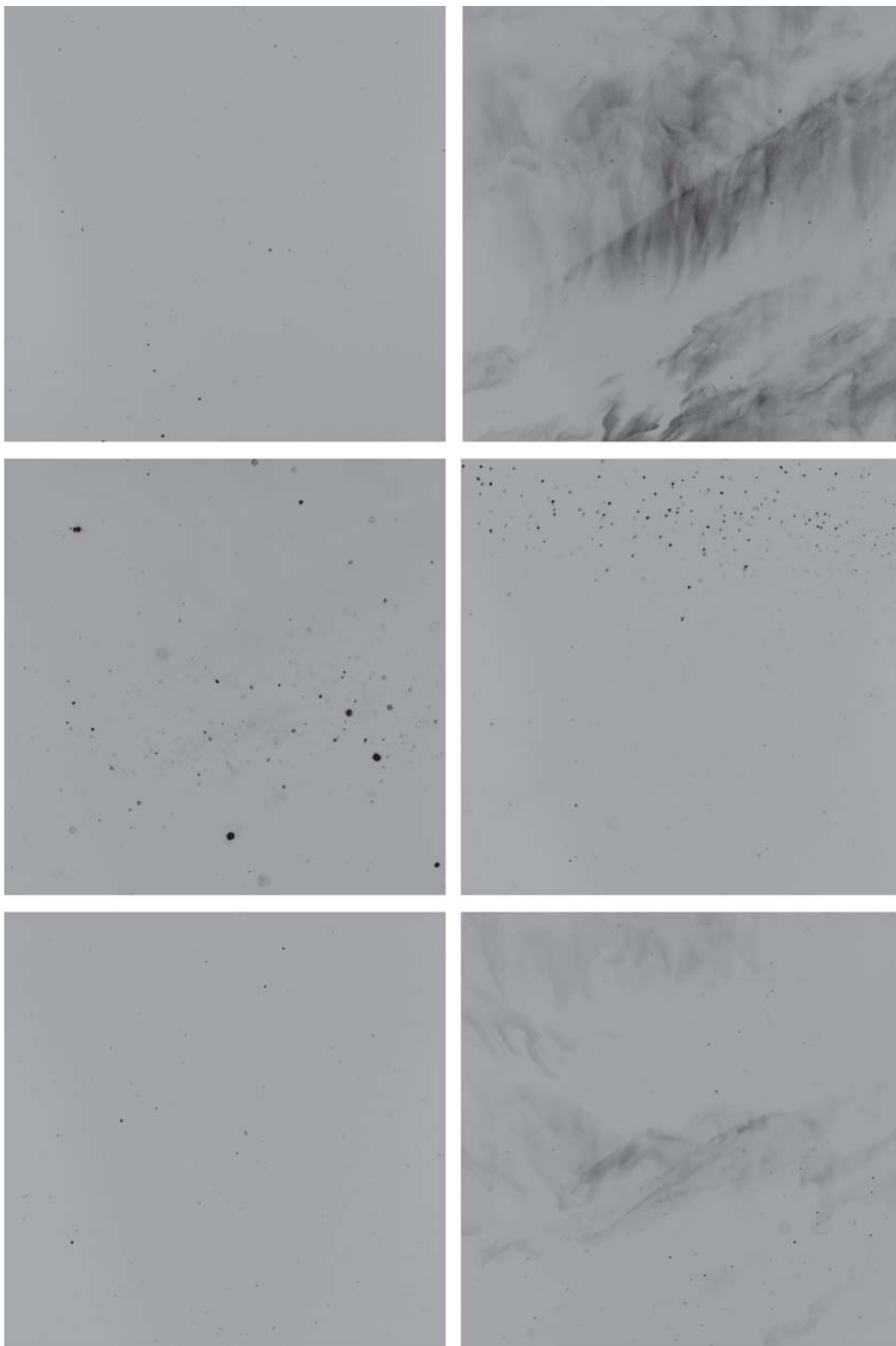
Figure 99. Contains 6 images of regions of interest from Case 6. Images are inverted black to white

141

Figure 100. Contains 4 images of regions of interest from Case 6. Images are inverted black to white

142

Case 7: Description and Images

Case 7 features a mix of carbon dioxide particles (produced with the simple shroud tube) and ambient water particles. This case used 406 image pairs,the higher laser intensity setting, and the 105 mm camera lens. There is visible carbon dioxide condensate clouds visible in these images.

Figure 101. Contains 1 image from Case 7. This image contains full image before the tunnel is turned on. Carbon dioxide particles are visible. Images is inverted from black to white

Figure 102. Contains 6 images of regions of interest from Case 7. Images are inverted black to white

144
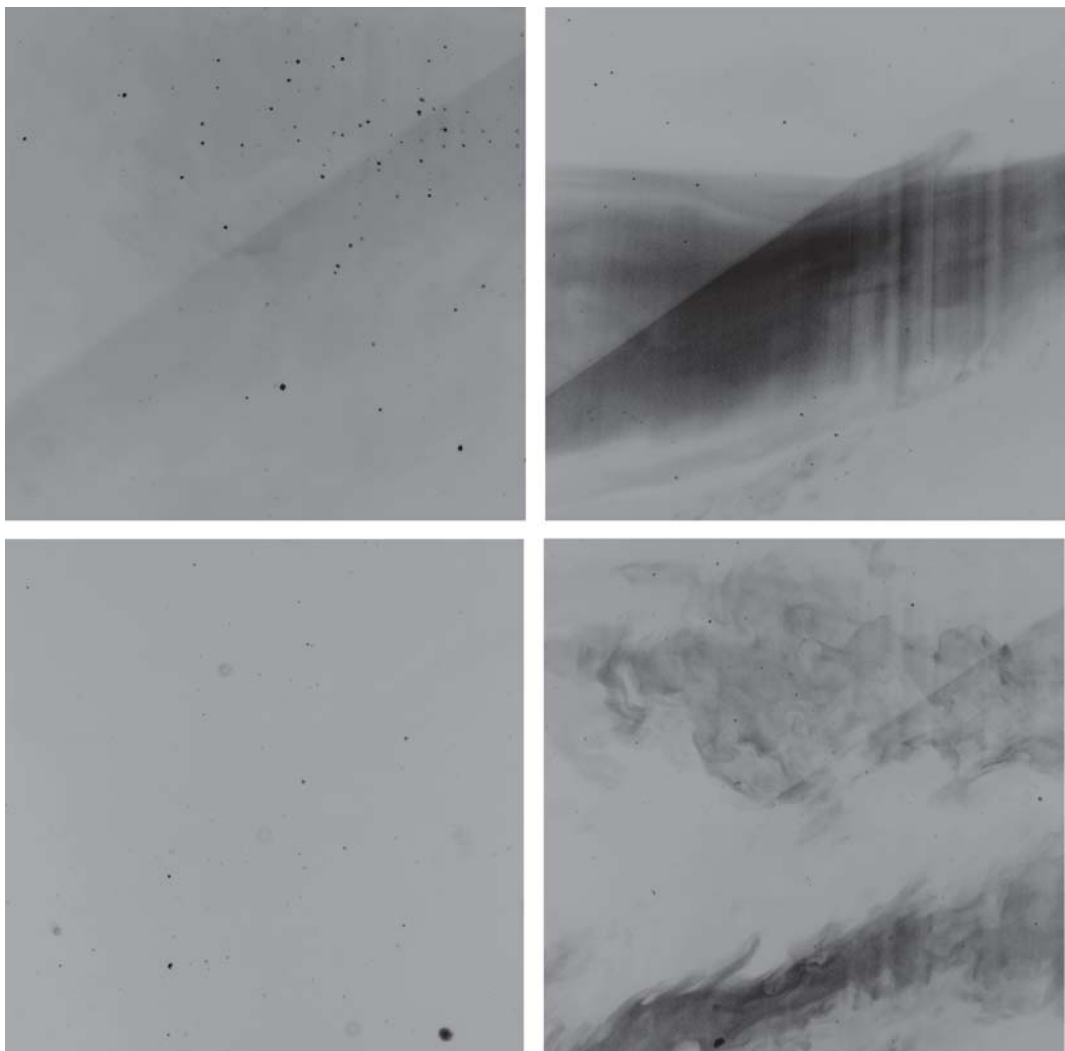
Figure 103. Contains 4 images of regions of interest from Case 7. Images are inverted black to white

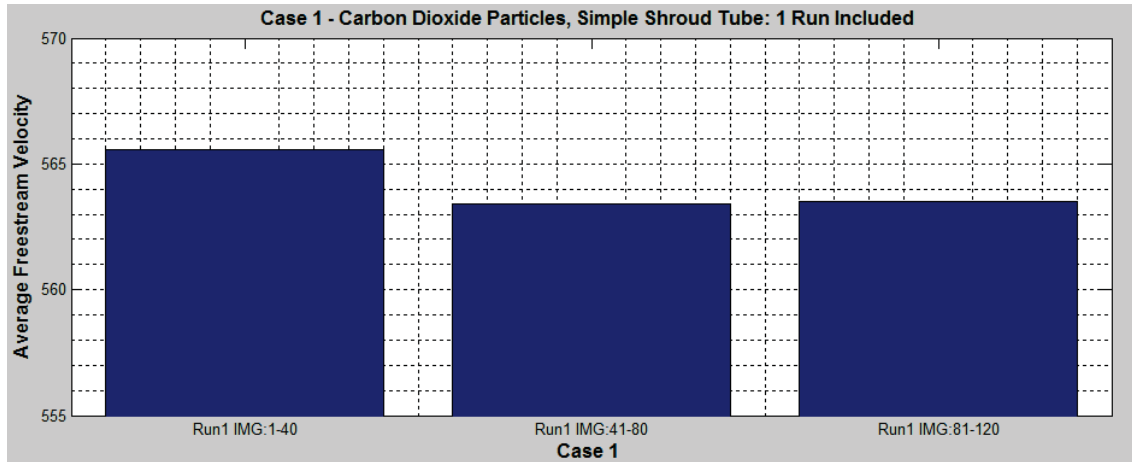# Appendix E.   Velocity Variation Plots

Figure 104.   Case 1, (Carbon Dioxide, Simple Shroud Tube) variation of average freestream velocity averaged over every 40 image pairs in chronological order.
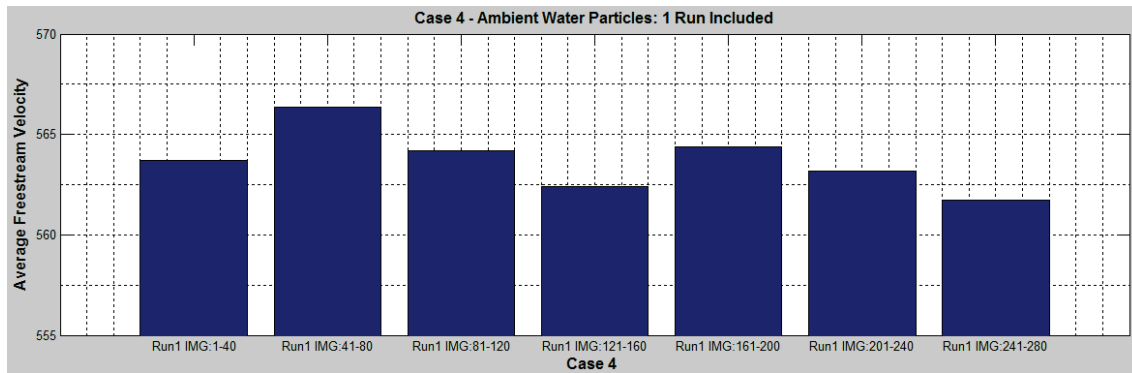

Figure 105. Case 4, (Ambient Water Particles) variation of average freestream velocity averaged over every 40 image pairs in chronological order
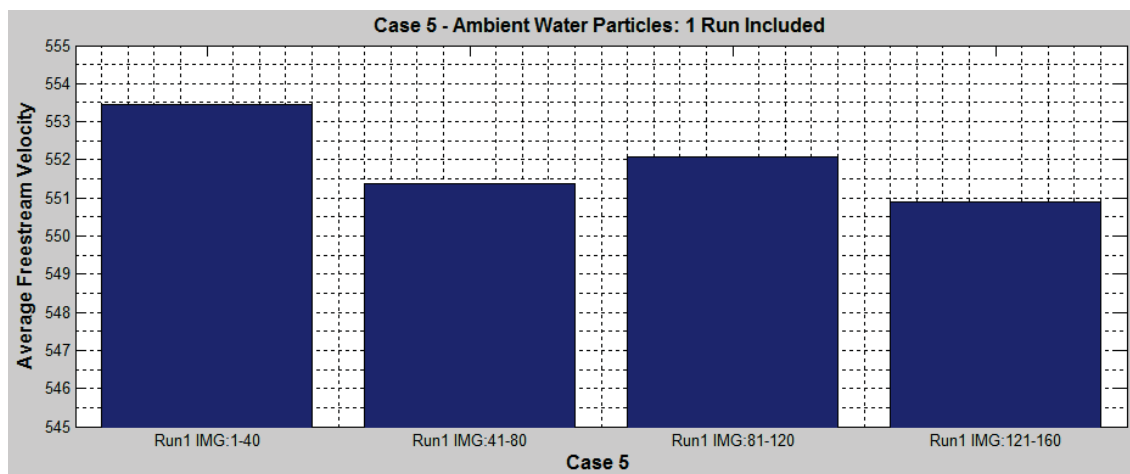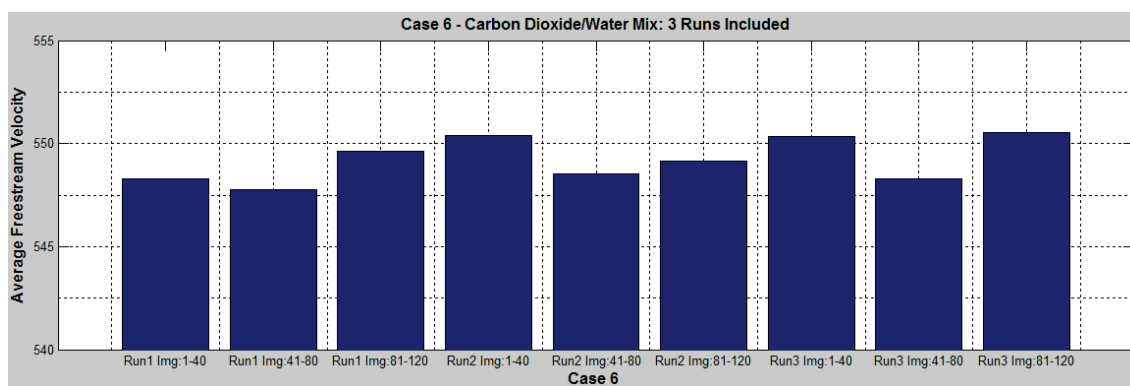
Figure 106. Case 5, (Ambient Water Particles) variation of average freestream velocity averaged over every 40 image pairs in chronological order

Figure 107. Case 6, (Ambient Water Particles) variation of average freestream velocity averaged over every 40 image pairs in chronological order
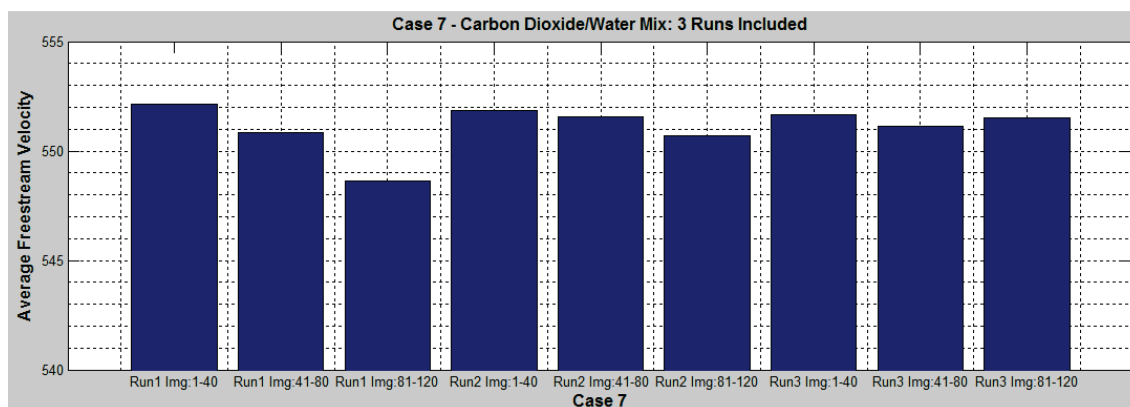
147

Figure 108. Case 7, (Ambient Water Particles) variation of average freestream velocity averaged over every 40 image pairs in chronological order

Bibliography

1. Adrian, R. J. "Twenty years of particle image velocimetry". *Experiments in Fluids*, Vol. 39, pp. 159–169, 2005.

2. Adrian, R.J. and S. Gordon. "The Impact of Particle Image Velocimetry on Aerospace Technology", June 2015. URL `http://www.aiaa-aviation.org/Notebook.aspx?id=28737`.

3. Anderson, J. D. *Fundamentals of Aerodynamics*. McGraw Hill, New York, 5th edition, 2011.

4. Balakumar, B. J. and R. J. Adrian. "The Impact of Particle Image Velocimetry on Aerospace Technology", 2004.

5. Beresh, S., J. Wagner, B. Pruett, Russel W. Spillers, M. McWithey, J. Gary, and K. Chankaya. "Deployment of Particle Image Velocimetry into the Lockheed Martin High Speed Wind Tunnel". *AIAA SciTech*, January 2014.

6. Brossard, C. J., C. Monnier, P. F. Barricau, X. Vandernoot, Y. LeSant, and F. Champagnat. "Principles and Applications of Particle Image Velocimetry". *AerospaceLab*, Issue 1, pp. 1–11, 2009.

7. Dynamics, Dantec. *DynamicStudio:User's Guide*. Dantec Dynamics, DK-2740 Skovlunde, Denmark, 9040u1859 edition, 2015.

8. Greene, B. *Characterization and Control of Carbon Dioxide Seed Particles in Particle Image Velocimetry*. Thesis, Air Force Institute of Technology, Dayton, OH, Mar 2008.

9. Hayes, J. "Mach 3 User Guide", April 2007.

10. Jahanmiri, M. *Particle Image Velocimetry: Fundamentals and its Applications.* Technical Report 2011:03, Chalmers University of Technology, March 2011.

11. Liber, M. *Measurment and Image Processing Techniques for Particle Image Velocimetry Using Solid-Phase Carbon Dioxide.* Thesis, Air Force Institute of Technology, Dayton, OH, Mar 2014.

12. Love, B. *Particle Size Control for PIV Seeding Using Dry Ice.* Thesis, Air Force Institute of Technology, Dayton, OH, Mar 2010.

13. Meinhart, C. D., S. T. Wereley, and J. G. Santiago. "PIV Measurements of a Microchannel Flow". *Experiments in Fluids*, Vol. 27, pp. 414–419, 1999.

14. Melling, A. "Tracer particles and seeding for particle image velocimety". *Measurement Science and Technology*, Vol. 8, pp. 1407–1416, 1997.

15. Merzkirch, W. *Techniques of Flow Visualization.* Technical Report 302, Advisory Group for Aerospace Research and Development, Dec 1984.

16. Optics, IDEX. "How to Select Cylindrical Lenses", Aug 2015. URL `www.marketplace.idexop.com`.

17. Raffel, M., C. E. Willert, S. T. Wereley, and J. Kompenhans. *Particle Image Velocimetry: A Practical Guide.* Springer, New York, 2nd edition, 2007.

18. Ragni, D., F. Schrijer, B. W. van Oudheusden, and F. Scarano. "Particle tracer response across shocks measured by PIV". *Experiments in Fluids*, Vol. 50, pp. 53–64, 2011.

19. Reuss, D. L. *Velocity,Vorticity, and Strain-Rate Ahead of a Flame Measured in an Engine Using Particle Image Velocimetry.* Technical Report 900053, SAE International, Feb 1990.

20. Ross, S. *A First Course in Probability.* Pearson, New Jersey, 8th edition, 2010.

21. Tropea, C., A. Yarin, and J Foss. *Springer Handbook of Experimental Fluid Mechanics.* Springer, New York, 1st edition, 2007.

22. Wegener, P. and L. Mack. "Condensation in Supersonic and Hypersonic Wind Tunnels". *Advances in Applied Mechanics*, Vol. 5, pp. 307–442, 1958.

23. Williams, O., T. Nguyen, A. Schreyer, and A. Smits. "Particle response analysis for particle image velocimetry in supersonic flows". *Physics of Fluids*, Vol 27, pp. 1–15, 2015.

24. Wolfe, D. *Boundary Layer Measurements in the Trisonic Gas-Dynamics Facility using Particle Image Velocimetry with CO2 Seeding.* Thesis, Air Force Institute of Technology, Dayton, OH, Mar 2012.

REPORT DOCUMENTATION PAGE

1. REPORT DATE (DD–MM–YYYY)
26 May 2016

2. REPORT TYPE
Master's Thesis

3. DATES COVERED (From — To)
Sept 2015 — 16 June 2016

4. TITLE AND SUBTITLE

PARTICLE IMAGE VELOCIMETRY AND ANALYSIS METHODS USING CLEANLY SEEDED PARTICLES IN SUPERSONIC FLOW

5a. CONTRACT NUMBER

5b. GRANT NUMBER

5c. PROGRAM ELEMENT NUMBER

6. AUTHOR(S)

Gulotta, Paul, A. , 2nd Lieutenant

5d. PROJECT NUMBER

JON 16Y252A

5e. TASK NUMBER

5f. WORK UNIT NUMBER

7. PERFORMING ORGANIZATION NAME(S) AND ADDRESS(ES)

Air Force Institute of Technology
Graduate School of Engineering and Management (AFIT/EN)
2950 Hobson Way
WPAFB OH 45433-7765

8. PERFORMING ORGANIZATION REPORT NUMBER

AFIT-ENY-MS-16-J-053

9. SPONSORING / MONITORING AGENCY NAME(S) AND ADDRESS(ES)

AFRL/RQVX
Att: Mr. Robert Guyton
2145 5th Street
WPAFB OH 45433
Email: Robert.guyton@wpafb.af.mil

10. SPONSOR/MONITOR'S ACRONYM(S)

AFRL/RQ

11. SPONSOR/MONITOR'S REPORT NUMBER(S)

12. DISTRIBUTION / AVAILABILITY STATEMENT

DISTRIBUTION STATEMENT A:
APPROVED FOR PUBLIC RELEASE; DISTRIBUTION UNLIMITED.

13. SUPPLEMENTARY NOTES

14. ABSTRACT

Particle Image Velocimetry (PIV) was successfully conducted in the Air Force Research Lab Mach 3/ Mach 6 Facility (M3M6F) for the first time. Particle response experiments evaluating the performance of dry ice particles were conducted using a 15 degree half-wedge in nominal Mach 3 flow. The particle response of carbon dioxide particles is compared to that of water particles produced from ambient moisture content in the tunnel system. Carbon dioxide particles produced particle response curves indicating particle diameters of approximately 2 microns acclimating to the asymptotic change in velocity across the shock between 25 and 30 mm on a path normal to the shock wave. Analysis methods such as cross correlation in 32x32 pixel and 64x64 pixel Interrogation Regions (IR), were compared to other techniques, namely the Adaptive PIV method and the Least Squares Method. The effects of analysis method on both freestream velocity and particle response were investigated.

15. SUBJECT TERMS

16. SECURITY CLASSIFICATION OF:			17. LIMITATION OF ABSTRACT	18. NUMBER OF PAGES	19a. NAME OF RESPONSIBLE PERSON
a. REPORT	b. ABSTRACT	c. THIS PAGE			Dr. M. Reeder, AFIT/ENY
U	U	U	UU	175	**19b. TELEPHONE NUMBER** (include area code) (937) 255-3636, x4530; Mark.reeder@afit.edu